Reaching towards higher masses of supersymmetric particles decaying to tau leptons

Institute of Physics and Technology

University of Bergen

Master's Thesis in Experimental Particle Physics

Author:
Agnethe Seim Olsen

June 30, 2014

Acknowledgements

The first person on a very long list is professor Anna Lipniacka, your input and guidance has been invaluable. Thank you for giving me the opportunity to be part of the ATLAS collaboration. I am very fortunate to have been allowed to spend two summers of learning and doing analysis with emerging and established scientists from all over the world, at CERN. Travelling to different countries for workshops, a PhD-school and shift-work has been very interesting.

This analysis, and my quality of life the past year, greatly benefits from the blind support, travel companionship, coffee breaks with coffee talk and coffee statistics, half marathons and answers to uninformed questions from Ørjan, Jan and Steffen (not all necessarily represented in all categories). Thanks to Bertrand, Wolfgang and Alex for expert opinions on and off Skype. Special thanks to Therese for always trying to include me in analysis, for continuously asking where I stand with my thesis, and for always being very honest. Your applied pressure has been much appreciated.

In a less particle physics related context, I would like offer thanks to Tordis and Renate for wine and crochet nights with some physics on the side. Thanks to Kine, Daniel, Thomas (the one with a cap and the one from the "north") and Tonje for lunches and shared frustrations. Thank you, Marita, for series-marathons with litres of tea. Thanks to Brit Ellen for letting me live with you, and for telling me "you probably needed that" if I ever overslept. A million thanks to my family for offering non-physics related conversation and free dinner. Chapter 1 is for you.

Finally, I want to thank you, Joe, for proofreading, for trying to keep me sane and well-fed and for being the most wonderful person.

Contents

Abstract

Searches for new physics beyond the established Standard Model (SM) is an important task in physics today. Supersymmetry (SUSY) is a candidate for an extension of the SM that can account for some of the unexplained phenomena. SUSY is searched for in many models and different final states. In many SUSY models the tau lepton can provide an important signature. SUSY realised at the electroweak (EW) scale would expect the third generation of sfermions to be the lightest sleptons. With R-parity conserved, this means the production rate into final states with taus is expected to be larger than into final states with electrons or muons. Compared to an analysis focussing on jets and missing transverse energy, E_T^{miss}, requesting a tau should provide a good measure of rejecting backgrounds, like multijet background, while keeping other kinematic cuts relaxed.

However, for the supersymmetric model minimal Super Gravity (mSUGRA), in the m_0 $m_{1/2}$ mass plane, the analysis "Search for supersymmetry in 8 TeV p–p collisions with τ-leptons, jets and missing transverse energy in the final state" [1] is less sensitive for low m_0 and high $m_{1/2}$ than the similar analysis "Search for squarks and gluinos with the ATLAS detector in final states with jets and missing transverse momentum and 20.3 fb^{-1} of $\sqrt{s} = 8$ TeV proton-proton collision data" [2]. The two analyses are looking at the same simulated mSUGRA signal samples, and the parameter values are the same; m_0 and $m_{1/2}$ are treated as grid parameters: $A_0 = -2m_0$, $\tan\beta = 30$ and $\mu{>}0$.

This thesis presents an optimisation of the search for SUSY in final states with one τ lepton, jets and missing transverse energy. The search is performed in proton-proton collisions at $\sqrt{s} = 8$TeV corresponding to an integrated luminosity of 20.3 fb^{-1}. The SUSY model considered is mSUGRA with the parameter values listed above. The event selection is optimised for maximal sensitivity to mSUGRA in the low m_0, high $m_{1/2}$ region of the mass plane

The result of the optimised analysis is interpreted in the mSUGRA model and a limit in the $(m_0, m_{1/2})$ plane is obtained. Values of $m_{1/2}$ up to 640 GeV are excluded for low m_0 and 300 GeV for high m_0 (2000 GeV $< m_0 <$ 5400 GeV).

List of Figures

List of Tables

Chapter 1

Introduction

If particle physics was music, the Standard Model (SM) would be a philharmonic orchestra. In a philharmonic orchestra there is a large instrumental ensemble divided into four sections. There are woodwinds, brass, strings and percussion. Among these instrument groups, and within each group, there is a generally accepted hierarchy. As the principal first violin is called the concertmaster, let's make this our electron. The electron is one of the three particles that make up matter, and the first violin is very often one of the instruments that play what builds up the main melody of the musical piece. The violin is also the smallest member of the violin family of string instruments. The other leptons would then be the viola-muon and the cello-tau. As for the very light, electrically neutral neutrinos, these could be triangles. A triangle is theoretically an instrument of indefinite pitch, for its fundamental pitch is obscured by its nonharmonic overtones. The neutrinos are particles of masses so tiny we have not yet got more than upper bounds, and they also tend to oscillate, meaning a neutrino of one type could become a neutrino of a different type. The triangle is part of the percussion group, and not a string instrument which would be more appropriate. Then again, neutrinos are a bit strange. Triangle-neutrinos it is.

Two other building blocks are needed to make up all of the matter we surround ourselves with, to make up us, to carry the melody. Up and down quarks make up the protons and neutrons that are, together with electrons, the constituents of atoms. These three elementary particles are, as far as we know, the only building blocks of all matter. The principal trumpet is generally considered the leader of the entire brass section, and the flute is often taken as the leader of the woodwinds. It only makes sense, then, to let the up and down quarks be the leader of two sections of quarks; up type (up, charm and top) and down type (down, strange and bottom) quarks. This translates into a trumpet-up-quark and a flute-down-quark. Next in line for the woodwinds are the oboe and the clarinet, and so oboe-strange and clarinet-bottom would make up the remaining down type

quark section. The two remaining up-type quarks could be the trombone-charm and the heavy tuba-top[1].

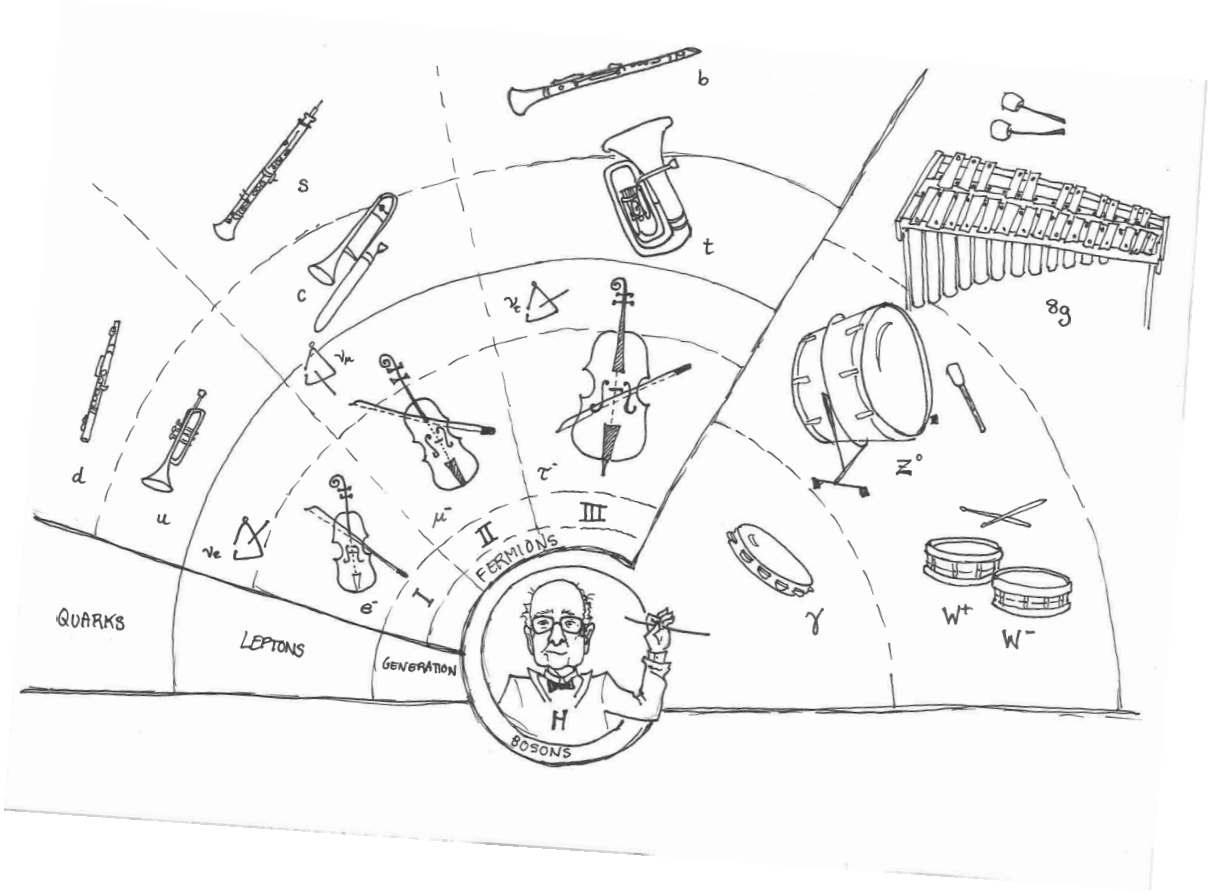

Figure 1.1: The Standard Model orchestra

Having all of these particles is great, but for anything of interest to happen they must be able to interact. For the music to have depth and sound good, we need percussion. Something to keep it all together. The $W^{\pm}$ and Z^0 mediate the weak force, and are relatively massive particles. Let us make these two snare drums and a bass drum. The photon, which mediates the electromagnetic force, can be represented by a tambourine. There are eight gluons mediating the strong force, and we can let these be combined to a glockenspiel. Glockenspiel-gluons, snare-drum-Ws, a bass-drum-Z and a tambourine-photon.

All the instruments we need are there, as shown in Figure 1.1, so why does the music sound so strange? An orchestra with no conductor could be a disaster. The last boson of the SM to be discovered was the Higgs boson. This is the

[1]The top quark is the heaviest elementary particle, with a mass of $173.07 \pm 0.52 \pm 0.72$ GeV [3]

quantum of a field particles interact with, and by doing so they acquire masses. The idea of all particles being massless makes as little sense as music from a conductorless orchestra. We know that some of the SM particles combine to build massive objects. Still, not all of the particles will pay attention to the conductor-Higgs. Neutrinos are very light, we only have an upper bound on their masses, and photons are completely massless. Triangle-neutrinos barely interact with the conductor, and tambourine-photons ignore him all together.

The SM also describes anti-particles. To have something equivalent in this experiment of thought, we have to modernize our philharmonic slightly. Let's take the violin-electron as an example. The anti-electron is more commonly known as a positron. The positron has almost exactly the same quantum numbers as the electron, that is to say they are very similar. The only difference is that the positron is positively charged whereas the electron is negatively charged. An electric violin can be made to look like an acoustic violin, but it is equipped with an electronic output of its sound. Anti-particles can then be represented by an electric version of the particle-instrument (yes, there is such a thing as an electric trumpet).

I will try not to take this analogy too far. Quite obviously musical instruments of our matter type will not annihilate with those of the antimatter type. Still, with this extension our combined acoustic and electric orchestra can play almost any kind of music you can think of. Saying that the orchestra *is* music would be wrong, just like saying that the Standard Model of particle physics *is* particle physics is an untrue statement. There are instruments that have not been included in the orchestra, and if you wanted to listen to anything with a vocal, you would have to look elsewhere. In the same way there are phenomenons in particle physics that the SM can't explain. One of the reasons I still think this is a good analogy for the SM[2] is that in an orchestra there is a certain structure, and the SM springs from the existence and breaking of symmetries. An orchestra can play a perfectly rhythmic, perfectly boring piece. Only when the music exploits the expectations of the audience and does something slightly, or completely, different things get interesting. Chapter 2 provides a more proper introduction to the SM, with Section 2.3 focusing on the symmetries the SM is built upon.

Dark matter is one of the things the SM (so far) can not explain. Some have looked into neutrinos being a candidate, but it seems there are not enough of them, and they are so extremely light. What is this dark matter, then? There are many answers to this question. Weakly Interacting Massive Particles (WIMPs) are still a strong candidate, though not a very well-defined one. Dark matter particles don't interact with photons, so we can not observe them directly. They

[2]Other than the fact that both music and particle physics are beautiful, but can, at times, be frustratingly hard to understand.

also interact, at best, weakly with our other bosons. Still, the existence of dark matter is not a field of controversy.

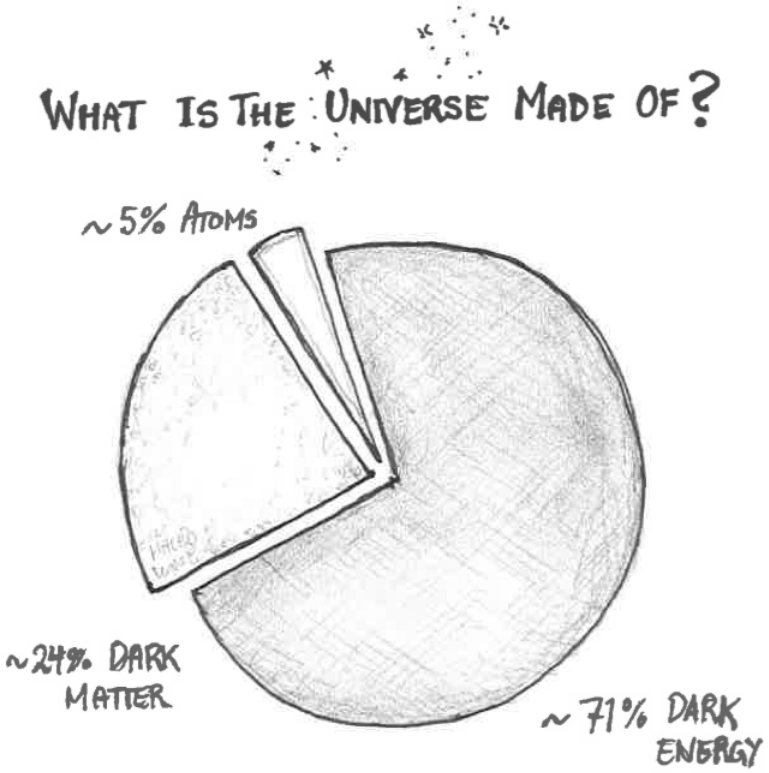

Figure 1.2: Composition of the universe. The numbers are taken from ref. [4]

The one way dark matter definitely does interact is gravitationally. Astrophysical observations such as the rotational curves in galaxies, the gravitational lensing of galactic clusters, the Wilkinson Microwave Anisotropy Probe (WMAP) Cosmic Microwave Background (CMB) anisotropy measurements [4], and Planck's complementing measurements of the CMB temperature and lensing-potential power spectra [5], and the simulations for large scale structures of the universe indicate that only 4-5 % of the energy density of our universe is made up of baryonic matter[3]. 23-24 % of the energy density can be attributed to cold[4], non-baryonic dark matter, and the remaining energy density is dark energy, as illustrated in Figure 1.2. Section 2.5 will go into this, and other challenges the SM is facing,

[3]Baryonic matter is matter the way we know it, made up from Standard Model particles
[4]*Cold* particles move slowly compared to the speed of light

and in Chapter 3 Supersymmetry (SUSY) comes to the rescue. This is a theory beyond the SM that can provide solutions to some of these problems.

Scientists have to be curious, ask the right questions, filter out the most correct answers, even make the right mistakes, to drive science forward. Scientists have to make measurements and analyse them. For figuring out the composition of the universe right after the Big Bang, or to observe particles proposed in a SUSY model, we need high energies. To achieve this particle physicists use particle colliders like the Large Hadron Collider (LHC) at CERN. There, protons are accelerated to near the speed of light before they are made to collide inside detectors like ATLAS (A Toroidal LHC Apparatus). Chapter 4 presents the history of the nuclear and particle physics laboratory, CERN, a brief overview of the LHC and a more detailed overview of ATLAS. This includes an introduction to how physics objects are reconstructed and identified in this detector. The tau lepton will be handled in greater detail in Chapter 5.

In addition to smashing particles together in big machines, particle physicists rely on good simulations. Monte Carlo simulations of the high energy physics processes that happen when two protons collide can be compared to the data taken with the detector. For the comparison to be more realistic, even the detector response is simulated, so that physicists know what signals to expect. To be able to make these simulations we need to have a good understanding of the processes that will be simulated. In this way results from analysis of data from experiments and simulations have to rely on each other to both be as good as possible. An introduction to event and detector simulation in ATLAS, as well as some tools used for analysis, is given in Chapter 6.

Among many possible approaches to detect SUSY, the direct production and observation of supersymmetric particles is one of the most promising. Different SUSY models can manifest themselves by very different signatures, and so the searches for SUSY more or less concern particular models. The searches focus on those signatures that have different predictions from SUSY and the SM. The sensitivity of the corresponding analysis heavily depends on the distinctness of the signature in the SM and in SUSY. If they differ a lot the conclusion on whether a SUSY model can be discovered or not will be a stronger statement. In the same way, the sensitivity depends on the accuracy of the two predictions. A more precise prediction, better simulations, allow for stronger conclusions from the measurement. However, for a detailed prediction of the SUSY appearance, a specific SUSY model has to be chosen. In the analysis presented in Chapter 7 the chosen SUSY model is mSUGRA. Section 3.2.1 will provide an introduction to this model.

Chapter 2

The Standard Model

Particle physics is the study of the fundamental constituents of matter and their interactions, and the SM is the theory that is currently used to describe it. The model has been repeatedly validated by experimental data, without challenging its fundamental structure making it a most satisfying theory. As of 2012, all particles predicted in the SM have been found by experiments. The last one, hiding from experimentalists until 2012, was the Higgs boson. On July 4th that year the ATLAS and CMS collaborations could announce that they had finally found a Higgs-like boson. An introduction to the Higgs-field and its effects follows in Section 2.4.

Gravity has not yet been included in the Standard Model, since the quantum theory of gravitation is not in agreement with General Relativity. A mediating particle of the gravitational field, the graviton, has been proposed. In March 2014 the BICEP2 experiment located at the South Pole [6] reported the discovery of primordial gravitational waves, ripples in space-time that carry a record of how the universe began. If these gravitational waves can be shown to originate from inflation, quantization of the gravitational field coupled to exponential expansion is predicted [7].

What is included in this Standard Model? How did it come to be so unanimously agreed upon? Jumping straight to a presentation of the SM could leave the reader feeling overwhelmed, and so this chapter will start off with a short summary of the history of particle physics. After this the main traits of the SM will be introduced. In Section 2.4 the "last piece of the puzzle", the Higgs boson will be given the spotlight, but this must be preceded by concepts of gauge theories and symmetries in particle physics. Finally, Section 2.5 will go through biggest problems of the SM.

2.1 The history of particles

The history of physics concerning particles starts with the discovery of the electron in 1897. It was discovered by J .J. Thomson in a cathode ray experiment conducted to test consequences of what he called the electrified-particle theory [8]. Thomson deduced that the electron was an elementary constituent of the atom but, atoms were electrically neutral and quite heavy, this lead to the problem of compensating for the negative charge and extra mass. In 1911, Rutherford demonstrated that the atom had most of its mass concentrated in a tiny positively charged core, the nucleus, in his scattering experiment where he fired a beam of α particles[1] at a sheet of gold foil [9]. In 1914, Bohr proposed a model of the hydrogen atom where the nucleus was circled by one electron. Bohr was able to calculate the spectrum of helium using an early form of quantum theory, the so-called "Bohr atom model" which assumed quantization of the orbital momentum. The hydrogen nucleus had been named the proton by Rutherford, and after exceptionally good agreement between Bohr's calculated spectrum and experiments, it seemed natural to assume that heavier atoms were built up from multiple protons circulated by an equal amount of electrons. The trouble of some unaccounted mass was settled was solved in 1932, with Chadwick's discovery of the neutron [10].

The process of discovering the photon started with Planck in 1900 as he attempted to explain the black-body spectrum of the electromagnetic radiation emitted by a hot object. The ultraviolet catastrophe[2] could be avoided if he assumed that electromagnetic radiation was quantised [11]

$$E = h\nu \tag{2.1}$$

where ν is the frequency and h is what we now call the Planck constant. Einstein took this idea even further when, in 1905, he argued that the quanta of the electromagnetic field was a particle: the photon [12]. An experiment conducted in 1923 by Compton confirmed Einstein's interpretation [13]. He found that light scattered off a particle (of mass m) at rest is shifted in wavelength, according to

$$\lambda' = \lambda + \lambda_c(1 - \cos\theta) \tag{2.2}$$

with λ being the initial wavelength, λ' the scattered wavelength, θ the scattering angle, and

$$\lambda_c = h/mc \tag{2.3}$$

[1] α particle is just another name for an ionised helium atom.

[2] The ultraviolet catastrophe came as a result of applying statistical mechanics to an electromagnetic field. The total power irradiated was predicted to grow infinitely large with growing frequencies!

the Compton wavelength of the target particle. This is the same result obtained by treating light as a particle of zero mass with energy given from Eq. 2.1, and applying the laws of relativistic energy and momentum conservation (as one would for a billiard ball collision).

Understanding light as both an electromagnetic wave and a particle can be difficult. Still, there is something more intuitive to light being quantised than to representing other particles as waves. The wave-particle duality was introduced by de Broglie in 1924, in his PhD thesis, Ref. [14]. The Copenhagen Interpretation of quantum mechanics, opposed by both de Broglie and Einstein, was primarily the product of Niels Bohr and Werner Heisenberg. One of the essential features of this interpretation is Heisenberg's uncertainty principle

$$\Delta x \Delta p \geq \frac{\hbar}{2} \tag{2.4}$$

which states that the product of the position and momentum uncertainties for any particle will be larger than a multiple of Planck's constant[3], or that position and momentum can not be accurately measured at the same time. Another essential feature is Bohr's complementarity principle. The wave and particle nature of objects can be regarded as complementary aspects of a single reality, that can be described by a wave function, Ψ. Upon measurement this wave function will collapse, nicely illustrated by the double slit experiment which was conducted with electrons for the first time in 1961, by Claus Jönsson [15].

So far the history of just two elementary particles has been told, the electron and the photon. The neutrino was first proposed by Pauli in 1930, securing the conservation of energy and momentum in β decay. The first neutrino was discovered experimentally by Reines and Cowan in 1956 [16]. In 1927, Dirac established the equation that now bears his name [17]. The Dirac equation was supposed to describe a free electron, but for every positive energy solution there was a corresponding solution with negative energy. This second result was later shown to correspond to an anti-matter electron, the positron. The electron's positively charged twin was found by Anderson in 1932 in a cosmic ray experiment [18]. Quarks, the constituents of protons, and neutrons, were postulated independently by Gell-Mann and Zweig in 1964. In 1968, deep inelastic scattering experiments at the Stanford Linear Accelerator Center (SLAC) showed that the proton contained tiny point-like objects and was not itself an elementary particle. The remaining elementary particles in the SM were discovered over time, with the top quark in 1995 as the last fermion or matter particle, and the Higgs boson discovery announced in 2012. As the observant reader may have picked up on, there are and has been a number of theories, postulations and experimental discoveries in

[3] $\hbar = h/2\pi$ is also called the reduced Planck constant or the Dirac constant.

particle physics. Listing much more of these would stray from the purpose of this section, which has been to put the SM in historical context. Particle physics now has a powerful theoretical framework, and any refinement or extension needs to be carefully fit in.

2.2 A brief overview of the Standard Model

In the Standard Model all particles are grouped in two categories: *fermions* and *bosons*. The SM fermions are particles with spin-1/2[4]. The bosons have integer spin. Matter is made up of fermions, which are divided into leptons and quarks. The fermions can be represented in a set of left-handed doublets and right-handed singlets, due to the weak isospin symmetry of the $SU(2)_L$ group, further explained in Section 2.3.3. There are six different leptons, classified according to electric charge (Q), electron number (L_e), muon number (L_μ) and tau number (L_τ). They naturally fall into three generations.

Fermions				**Bosons**	
Quarks	$\begin{pmatrix} u \\ d \end{pmatrix}$	$\begin{pmatrix} c \\ s \end{pmatrix}$	$\begin{pmatrix} t \\ b \end{pmatrix}$	*Fundamental Interaction*	*Mediators*
Leptons	$\begin{pmatrix} \nu_e \\ e^- \end{pmatrix}$	$\begin{pmatrix} \nu_\mu \\ \mu^- \end{pmatrix}$	$\begin{pmatrix} \nu_\tau \\ \tau^- \end{pmatrix}$	- Strong - Electromagnetic - Weak	8 gluons γ W^+,W^-,Z^0
Generation	I	II	III	Higgs boson	H^0

Table 2.1: Particles of the Standard Model

An electron will form a doublet with its corresponding electron neutrino, both of these having $L_e = +1$, $L_\mu = 0$ and $L_\tau = 0$, the electron having $Q = -1$ and the ν_e being electrically neutral. The same is true for the heavier μ-lepton and τ-lepton, respectively.

The quarks fall into the same number of generations as the leptons. They are characterised by their fractional charges and quarks flavour numbers U,D,C,S,T

[4]Spin is meant here as the intrinsic quantum number.

and B, one for each flavour. The fermions are shown in their multiplets and generations in Table 2.1. The quarks in the top row of a doublet, up-type quarks, have value +1 for its flavour quantum number, the ones in the bottom row, the down-type quarks, −1. The three up-type quarks (up, charm and top) all have $Q = +2/3$. The down-type quarks (down, strange and bottom) have $Q = -1/3$.

The fermions all have anti-particles. The anti-matter particles have Q of opposite sign of the corresponding matter particle. Each of the quarks and antiquarks also come in three colours[5], or anti-colours. These are usually called red, blue and green, anti-red, anti-blue and anti-green.

Finally, every interaction has its mediator. These are the bosons of the SM. The massless photon mediates the electromagnetic force. The mediators of the weak force are the two Ws, W^+ and W^-, and the electrically neutral Z boson. Only electrically charged particles are influenced by the electromagnetic force, while all fermions interact weakly. The strong force is mediated by 8 gluons that carry both colour and anti-colour. This means gluons interact with quarks and anti-quarks, but also amongst themselves. Coloured objects cannot exist as isolated particles. Quarks have only been observed in bound states called hadrons, of which there are two categories: mesons and baryons. A meson is a bound state of a quark and an anti-quark. A baryon consists of three quarks. The last particle in the SM is the Higgs boson which shall be illuminated in Section 2.4

2.3 Gauge Theories

Symmetries play an important role in particle physics. The invariance of the Lagrangian density $\mathcal{L}$[6] under a continuous one-parameter set of transformations implies, by Noether's theorem [19], a conserved quantity. For every continuous symmetry transformation in field theory, there is a corresponding conserved current. This hold as long as the field equations are satisfied [20]. This means, if the Lagrangian density is required to be invariant under a local gauge transformation, introduction of a set of gauge potentials with couplings to fermion and scalar matter follows. This set of gauge potentials, with their couplings, is completely determined by symmetry principles [21].

The SM is a theory of fields. Within the mathematical formalism of the SM, $\mathcal{L}$ is required to be invariant under local gauge transformations. Depending on the transformation, additional gauge fields have to be introduced to guarantee the invariance. These extra fields couple to the fermionic fields and can be interpreted as messengers, which mediate the interactions between fermions.

[5] Colour is a quantum number, like charge.

[6] The Lagrangian, L, of a dynamical system is a function that summarises the dynamics of the system. The Lagrangian density can be defined from $\mathrm{L} = \int \mathcal{L}\, dx^3$

A symmetry is an operation you can perform on a system that leaves the system invariant. The set of all symmetry operations, on a particular system, has four properties:

Closure: Performance of an operation on members of the set always produces a member of the same set. If R_i and R_j are in the set, then R_iR_j (first perform R_j, then perform R_i) is also in the set; there exists some R_k such that $R_iR_j = R_k$

Identity: There is an element I such that $IR_i = R_iI = R_i$ for all R_i.

Invers: For any element R_i there is an inverse, R_i^{-1}, such that $R_iR_i^{-1} = R_i^{-1}R_i = I$.

Associativity: $R_i(R_jR_k) = (R_iR_j)R_k$

Group theory can be regarded as the systematic study of symmetries, and the properties listed above are the defining properties of a mathematical group. Group elements do not necessarily commute

Commutation: $R_iR_j = R_jR_i$

If all elements do commute the group is said to be abelian. If not the group is non-abelian.

Most groups of interest in physics can be represented as groups of matrices. In particle physics, the most common groups are unitary groups: $U(n)$ and $SU(n)$. $U(n)$ is the collection of all unitary $n \times n$ matrices. A unitary matrix is a matrix whose inverse is equal to its transpose conjugate

$$U^\dagger = U^{-1} \tag{2.5}$$

where $U^\dagger = (U^*)^T$.
$SU(n)$ is the collection of all unitary $n \times n$ matrices with the additional constraint

$$\det U = 1 \tag{2.6}$$

These are called special unitary groups [22].

The remainder of this section will provide an introduction to the symmetry groups used to describe the transformation of particles in the SM. Quantum electrodynamics (QED) is the gauge field theory of electromagnetic interaction occurring among electrically charged fermions. The QED Lagrangian density is invariant under a symmetry transformation of the $U(1)$ group, further explained in Section 2.3.1. The weak interaction is described by the $SU(2)_L$ group. At

the electroweak scale, which is the energy scale around 246 GeV[7], QED and the electroweak interaction are unified. Electroweak theory is described by the $SU(2)_L \times U(1)_Y$ group, further explained in Section 2.3.3. Quantum chromodynamics (QCD) is the field theory of the strong interaction, and the QCD Lagrangian density is invariant under $SU(3)_C$ symmetry transformations, described in Section 2.3.2.

2.3.1 Quantum Electrodynamics and $U(1)$

QED is the relativistic quantum field theory of electrodynamics. Mathematically, it is an abelian gauge theory with the symmetry group U(1). The classical electromagnetic fields can be described by Maxwell's equations. From the two of Maxwell's equations for free fields (no charge)

$$\nabla \cdot \mathbf{B}(x) = 0 \qquad \nabla \times \mathbf{E}(x) = -\frac{\partial}{\partial t}\mathbf{B}(x) \tag{2.7}$$

it can be shown that there exists a scalar potential $\phi(x)$ and a vector potential $\mathbf{A}(\mathbf{x})$, such that

$$\mathbf{B}(x) = \nabla \times \mathbf{A}(\mathbf{x}) \quad \mathbf{E}(x) = -\nabla\phi(x) - \frac{\partial}{\partial t}\mathbf{A}(x) \tag{2.8}$$

Classically quantities with physical significance are the fields $\mathbf{E}(x)$ and $\mathbf{B}(x)$, and the potentials $\mathrm{A}_\mu(x) = (\phi(x), \mathbf{A}(\mathbf{x}))$ are auxiliary quantities that are not unique due to the gauge invariance of the theory. This means that we can change $\mathrm{A}_\mu(x)$, as long as the change leaves $\mathbf{E}(x)$ and $\mathbf{B}(x)$ unchanged. These are called gauge transformations. For example, as $\mathbf{B}(x)$ is the rotation of $\mathrm{A}_\mu(x)$, and the rotation of a gradient is zero, we can make the substitution

$$A_\mu(x) \to A'_\mu(x) = A_\mu(x) + \partial_\mu\chi(x) \tag{2.9}$$

where $\chi(x)$ is an arbitrary function. This is a $U(1)$ local gauge transformation.

In quantum theory, the potentials A_μ play the leading role and so we have to formulate the theory in terms of A_μ and not $\mathbf{E}$ and $\mathbf{B}$. The field A_μ is interpreted as the photon field, and the Lagrangian density of a free electromagnetic field is

$$\mathcal{L}_\gamma = \frac{1}{4}F^{\mu\nu}(x)F_{\mu\nu}(x) \tag{2.10}$$

where $F^{\mu\nu} = \partial^\mu A^\nu - \partial^\nu A^\mu$ is the electromagnetic field tensor.

The Dirac Lagrangian density describing a free fermion of mass m, represented by the field $\psi(x)$, is

[7]The number 246 GeV was taken from a calculation of the vacuum expectation value of the Higgs field, see Section 2.4

$$\mathcal{L}_{\text{fermion}} = \bar{\psi}(x)[i\gamma^\mu \partial_\mu - m]\psi(x) \tag{2.11}$$

where γ^μ are the Dirac matrices and $\bar{\psi(x)} \equiv \psi^\dagger(x)\gamma^0$. The gauge transformation of the fermion field is

$$\psi(x) \to \psi'(x) = e^{iq\chi(x)}\psi(x) \tag{2.12}$$

This can be thought of as multiplication of ψ by a unitary matrix, $U = e^{iq\chi(x)}$. $U(1)$ is the group of all such matrices, and so this is $U(1)$ gauge invariance. The gauge transformations in Eq. 2.9 and Eq. 2.12 present us with a problem. The derivative in Eq. 2.11 is no longer invariant. The Dirac Lagrangian density is invariant under global phase transformations, like the one in Eq. 2.12. If the phase factor is different at different space-time points; that is, if χ is a function of x^μ, the phase transformation is local and the Lagrangian is no longer invariant. The requirement of the local gauge invariance introduces interaction between photon and electron. When looked upon in its own gauge, invariance of the electromagnetic potential is equivalent to forbidding transverse polarization for the photon. The solution is what is called the minimal substitution, where the derivative is substituted by a covariant derivative

$$\partial_\mu \to D_\mu = \partial_\mu - iqA_\mu(x) \tag{2.13}$$

The QED Lagrangian density of a fermionic field interacting with the electromagnetic field is given by the real part of

$$\mathcal{L}_{\text{QED}} = \overline{\psi}(x)(i\gamma^\mu D_\mu - m)\psi(x) + \frac{1}{4}F^{\mu\nu}(x)F_{\mu\nu}(x) \tag{2.14}$$

This is the Lagrangian density of the electromagnetic field and the fermion Lagrangian density with minimal substitution. Eq. 2.14 can be rewritten as

$$\begin{aligned}\mathcal{L}_{\text{QED}} &= \mathcal{L}_{\text{fermion}} + \mathcal{L}_{\text{int}} + \mathcal{L}_\gamma \\ &= \overline{\psi}(x)(i\gamma^\mu \partial_\mu - m)\psi(x) + iq\bar{\psi}(x)\gamma^\mu A_\mu \psi(x) + \frac{1}{4}F^{\mu\nu}(x)F_{\mu\nu}(x)\end{aligned} \tag{2.15}$$

where $\mathcal{L}_{\text{int}} = iq\bar{\psi}(x)\gamma^\mu A_\mu \psi(x) = j^\mu A_\mu$ and j^μ is the conserved electromagnetic current. And so invariance under the $U(1)$ transformation leads to conservation of electric charge, q.

2.3.2 Quantum Chromodynamics and $SU(3)_C$

Electromagnetic interactions are associated with the fermion electric charges, while fermion flavours are related to electroweak phenomena. The strong forces

are flavour conserving and flavour independent, and the carriers of the electroweak interaction do not couple to the quark colour. It is natural then to take colour as the charge associated with the strong force, leading to interactions between quarks and gluons, and try to build a quantum field theory around it.

Quantum chromodynamics is a non-abelian gauge theory. We now denote the quark fields $\psi_f^\alpha(x)$, where f is the flavour, and α one of the three colours. To simplify, we adopt the notation in colour space: $\psi_f^T(x) = \left(\psi_f^1(x), \psi_f^2(x), \psi_f^3(x)\right)$. The free Lagrangian density

$$\mathcal{L}_0^{\mathrm{QCD}} = \sum_f \bar{\psi}_f(x)\left(i\gamma^\mu\partial_\mu - m_f\right)\psi_f(x) \tag{2.16}$$

is invariant under global $SU(3)_C$ transformations in colour space.

$$\psi_f^\alpha(x) \to (\psi_f^\alpha(x))' = U_\beta^\alpha \psi_f^\beta \qquad UU^\dagger = U^\dagger U = 1 \qquad \det(U) = 1 \tag{2.17}$$

In the $SU(3)_C$ algebra there are eight generators, $\frac{1}{2}\lambda_a$ $(a = 1, ..., 8)$. These are traceless matrices that satisfy the relation

$$\left[\frac{\lambda^a}{2}, \frac{\lambda^b}{2}\right] = if^{abc}\frac{\lambda^c}{2} \tag{2.18}$$

where f^{abc} are real antisymmetric $SU(3)_C$ structure constants.

The $SU(3)_C$ transformation acting on the spinor, ψ_f^α, in Eq. 2.17 can be written in the form

$$U = \exp\left(i\frac{\lambda^a}{2}g_s\chi_a\right) \tag{2.19}$$

Here g_s is the coupling constant of QCD and χ_a are arbitrary parameters. A sum over repeated indices is understood.

Following the same procedure as with QED we now require the free Lagrangian in Eq 2.16 to be invariant under local $SU(3)_C$ transformations as well: $\chi_a = \chi_a(x)$. The derivatives will again be substituted by covariant derivatives. The eight independent gauge parameters give rise to eight vector fields, $G_a^\mu(x)$ in the theory. These are interpreted as the eight gluons. The gauge transformation of gluon fields is more complicated than for the photon in QED. As the $SU(3)_C$ matrices do not commute, there are additional terms involving self-interaction between the gluons.

It can be shown [23] that the total QCD Lagrangian density can be written as

$$\mathcal{L}_{\text{QCD}} = \sum_f \bar{\psi}_f(x) \left(i\gamma^\mu D_\mu - m_f\right) \psi_f(x) + \frac{1}{4} G_a^{\mu\nu}(x) G^a_{\mu\nu}(x) \tag{2.20}$$

where the gluon field strength tensor is

$$G_a^{\mu\nu}(x) = \partial^\mu G_a^\nu(x) - \partial^\nu G_a^\mu(x) - g_s f^{abc} G_b^\mu G_c^\nu \tag{2.21}$$

and the covariant derivative is defined to be

$$D^\mu(x) \equiv \partial^\mu + i g_s \frac{\lambda_a}{2} G_a^\mu(x) \tag{2.22}$$

The QCD Lagrangian in 2.20 looks as simple as the QED Lagrangian in 2.14 even though the theory is more complicated. This is because of its colour symmetry properties. As the additional self-interactions amongst gauge fields is not present for photons in QED, it would be reasonable to expect that these interactions cause some of the very interesting features in QCD - asymptotic freedom and confinement. Asymptotic freedom means that strong interaction becomes weaker at short distances. Inside a hadron, the quarks are seemingly free. Correspondingly, confinement describes the fact that the strong force increases at large distances. Particles with colour charge cannot be isolated, only colour neutral objects can. The potential energy required to separate two quarks increases linearly with the distance between them, due to vacuum polarisation. This means the colour ionisation potential becomes infinite. If energy is injected into a hadron, the constituent quarks will not be separated. Instead, new quark-anti-quark pairs are formed in a process known as hadronisation.

2.3.3 Electroweak theory and $SU(2)_L \times U(1)_Y$

Electroweak theory is, as the name suggests, the unified theory of electromagnetic and weak interaction. Low-energy experiments have provided a large amount of information about the underlying dynamics of flavour-changing. Detailed analysis of the energy and angular distributions in β decays, such as

$$n \to p + e^- + \nu_e \tag{2.23}$$

made clear that only the left-handed (right-handed) fermion (anti-fermion) chiralities participate in those weak transitions; moreover, the strength of the interaction appears to be universal.

The chirality of a fermion, ψ, is defined by the operator γ^5 with eigenvalues ± 1. The field can be projected into its left- or right-handed component by the operation of the projection operator P^L or P^R

$$\left.\begin{array}{l}\psi^L(x) = P^L\psi(x) \\ \psi^R(x) = P^R\psi(x)\end{array}\right\} = \frac{(1 \pm \gamma^5)}{2}\psi(x) \tag{2.24}$$

Anti-particles have opposite chirality of their particle partners. All neutrinos are left-handed, while anti-neutrinos are right-handed. For simplicity, $\psi_1(x)$, $\psi_2(x)$ and $\psi_3(x)$ we introduce the notation

$$\psi_1(x) = \begin{pmatrix}\psi^L_{\nu_l}(x) \\ \psi^L_l(x)\end{pmatrix} \qquad \psi_2(x) = \psi^R_l(x) \tag{2.25}$$

$$\psi_1(x) = \begin{pmatrix}\psi^L_u(x) \\ \psi^L_d(x)\end{pmatrix} \qquad \psi_2(x) = \psi^R_u(x) \qquad \psi_3(x) = \psi^R_d(x) \tag{2.26}$$

which will be used for the remainder of this discussion. l and ν_l represent the leptons and lepton neutrinos, e, μ, τ and ν_e, ν_μ, ν_τ respectively. u and d represent the up- and down-type quarks, u, c, t and d, s, b respectively.

The symmetry group $U(1)_Y$ is essential in order to incorporate electric charge Q and unify weak and electromagnetic interactions in a common gauge structure. The $U(1)_Y$ conserves hypercharge, Y,

$$Q = T_3 + \frac{1}{2}Y \tag{2.27}$$

where T_3 is the third component of isospin.

Analogous to QED and QCD, the free Lagrangian density

$$\mathcal{L}_0^{\mathrm{EW}} = \sum_{j=1}^{3} i\bar{\psi}_j(x)\gamma^\mu\partial_\mu\psi_j(x) \tag{2.28}$$

is invariant under global transformations in flavour space

$$\begin{array}{l}\psi_1(x) \to \psi_1'(x) \equiv U(\alpha)_L U(\beta)_Y \Psi_1(x) \\ \psi_2(x) \to \psi_2'(x) \equiv U(\beta)_Y \Psi_2(x) \\ \psi_3(x) \to \psi_3'(x) \equiv U(\beta)_Y \Psi_3(x)\end{array} \tag{2.29}$$

$$U(\alpha)_L \equiv \exp\left(i\tfrac{\sigma_j}{2}\alpha^j\right) \qquad U(\beta)_Y \equiv \exp\left(iy_j\beta\right) \qquad (j = 1, 2, 3) \tag{2.30}$$

where $U(1)_Y$ conserves hypercharge y_j in a transformation analogous to the one in QED. α_j is an arbitrary vector in isospin space and σ_j are the Pauli matrices, the generators of the $SU(2)$ symmetry transformations,

$$\sigma^1 = \begin{bmatrix} 0 & 1 \\ 1 & 0 \end{bmatrix} \qquad \sigma^2 = \begin{bmatrix} 0 & -i \\ i & 0 \end{bmatrix} \qquad \sigma^3 = \begin{bmatrix} 1 & 0 \\ 0 & -1 \end{bmatrix} \tag{2.31}$$

The $SU(2)_L$ transformation only acts on $\psi_1(x)$, whilst the $U(1)_Y$ acts on both right-handed and left-handed particles.

The next step would be to require the Lagrangian og Eq. 2.28 to be invariant under local $SU(2)_L \otimes U(1)_Y$ transformations as well, with

$$U(\alpha(x)) = \exp\left(ig_w \tfrac{\sigma_j}{2} \alpha^j(x)\right) \qquad U(\beta(x)) = \exp\left(ig'\beta(x)\right) \tag{2.32}$$

Four gauge parameters means four different gauge bosons. The requirement of invariance under the transformations in Eq. 2.32 leads to new covariant derivatives in Eq. 2.28:

$$\begin{aligned} D_\mu \psi_1(x) &\equiv \left[\partial_\mu + ig\sigma_j \frac{W_\mu^j(x)}{2} + ig' y_1 B_\mu(x)\right] \\ D_\mu \psi_2(x) &\equiv \left[\partial_\mu + ig' y_2 B_\mu(x)\right] \\ D_\mu \psi_3(x) &\equiv \left[\partial_\mu + ig' y_3 B_\mu(x)\right] \end{aligned} \tag{2.33}$$

with three fields, $W_j(x)$, originating from the $SU(2)_L$ transformation, and the field $B(x)$ corresponding to $U(1)_Y$. This is analogous to saying that invariance under $SU(2)_L$ generates three conserved weak isospin currents

$$J_i^\alpha(x) = \tfrac{1}{2}\bar{\psi}_1(x)\gamma^\alpha \sigma_i \psi_1(x) \qquad\qquad i = 1, 2, 3 \tag{2.34}$$

and that the corresponding "charge", weak isospin, is conserved. The two currents, $J_1^\alpha(x)$ and $J_2^\alpha(x)$, can be rewritten in such a way that they represent a positively charged and a negatively charged current that connect electrically charged and neutral fields, while J_3^α couples to left-handed particles of the same type. Invariance under $U(1)_Y$ leads to a conserved electromagnetic current. These conserved currents act as sources for the gauge fields.

The Lagrangian density of electroweak interaction is given as

$$\mathcal{L}_{\text{EW}} = \sum_{j=1}^{3} \bar{\psi}_j(x)\gamma^\mu D_\mu \psi_j(x) + \mathcal{L}_{\text{kin}} \tag{2.35}$$

Here, $\mathcal{L}_{\text{kin}}$ is the properly normalised kinetic Lagrangian density necessary to have a gauge-invariant kinetic term for the gauge fields

$$\mathcal{L}_{\text{kin}} = -\frac{1}{4} B_{\mu\nu}(x) B^{\mu\nu}(x) - \frac{1}{4} W_{\mu\nu}^j(x) W_j^{\mu\nu}(x) \tag{2.36}$$

with

$$\begin{aligned} B_{\mu\nu}(x) &\equiv \partial_\mu B_\nu(x) - \partial_\nu B_\mu(x) \\ W^j_{\mu\nu}(x) &\equiv \partial_\mu W^j_\nu(x) - \partial_\nu W^j_\mu(x) - g\epsilon_{jkl} W^k_\mu(x) W^l_\nu(x) \end{aligned} \tag{2.37}$$

The two fields, $W_1(x)$ and $W_2(x)$, can be linearly combined to give rise to the two physical fields W_μ and $W^\dagger_\mu$. These are interpreted as the fields of the charged gauge bosons, $W^\pm$.

$$\begin{aligned} W_\mu(x) &= \frac{1}{\sqrt{2}} \left(W^1_\mu - i W^2_\mu \right) \\ W^\dagger_\mu(x) &= \frac{1}{\sqrt{2}} \left(W^1_\mu + i W^2_\mu \right) \end{aligned} \tag{2.38}$$

When we look at left-handed doublets of quarks, quark generation mixing leads to each doublet not being limited to one generation. A charged current interaction with one of the W bosons allows for a transition between up- and down-type quarks with a unit charge difference. The mixing between the quark generations is described by the Cabbibo-Kobayashi-Maskawa (CKM, further explained in Ref. [24, 25]).

The two neutral fields, $W_3(x)$ and $B(x)$, mix to form $A_\mu(x)$, and a second electrically neutral field, $Z_\mu(x)$

$$\begin{pmatrix} A_\mu(x) \\ Z_\mu(x) \end{pmatrix} = \begin{pmatrix} \cos(\theta_W) & \sin(\theta_W) \\ -\sin(\theta_W) & \cos(\theta_W) \end{pmatrix} \begin{pmatrix} B(x) \\ W^3_\mu(x) \end{pmatrix} \tag{2.39}$$

interpreted as the photon γ and the Z^0 boson. The size of the mixture of the singlet field $B(x)$ and $W_3(x)$ is given by the Weinberg angle θ_W. In this representation of the photon field the electroweak couplings are related to electromagnetic charge, e, by

$$g \sin\theta_W = g' \cos\theta_W = e \tag{2.40}$$

This is the unbroken electroweak theory. A problem with this model is that there are no mass terms in the Lagrangian density. Experimental results show that both $W^\pm$ and Z^0 are very massive particles. Vector bosons are introduced to the theory by breaking the $SU(2)_L \otimes U(1)_Y$ gauge symmetry. This is done using the Brout-Englert-Higgs mechanism, which will be introduced in Section 2.4.

2.4 The Brout-Englert-Higgs mechanism

The term mass is one most people know of and have a relationship to. Even though being referred to as massive probably isn't a favourite, we all are. Why

are we massive, though? What mechanism causes SM particles to acquire mass? There are many lovely explanations available, like the film from PHD Comics in Ref. [26] or the cartoon from CERN in Ref. [27]. This section will provide a short introduction to the basic idea of the Brout-Englert-Higgs mechanism that describes how the $SU(2)_L \otimes U(1)_Y$ gauge symmetry is broken by the introduction of a new field: the Higgs field.

In physics an exact symmetry has to satisfy two conditions: it must be a symmetry of the Lagrangian of the system, and it has to be the symmetry of the lowest energy state of the system. If the latter condition is not satisfied then the symmetry is hidden. The true symmetry of the system is concealed by the arbitrary selection of a particular ground state. The Brout-Englert-Higgs mechanism (BEH mechanism) of spontaneous symmetry breaking was introduced in 1964 by two independent groups; Peter Higgs; François Englert and Robert Brout [28, 29]. The mechanism was generalised from the Goldstone model[8] to be invariant under the local $U(1)$ gauge transformation in order to give mass only to W and Z bosons. The standard model also predicts that the Higgs field couples to fermions through a Yukawa interaction, giving rise to the masses of quarks and leptons. It is important to note, however, that most of the mass in composite particles (like protons, nuclei, and atoms) does not come from the BEH mechanism, but from the binding energy that holds these particles together.

In order to construct the BEH mechanism, a complex scalar field is introduced

$$\phi(x) = \frac{1}{\sqrt{2}} \left(\phi_1(x) + i\phi_2(x)\right) \tag{2.41}$$

with Lagrangian density

$$\mathcal{L}_H = \partial^\mu \phi^\dagger(x) \partial_\mu \phi(x) - V(x) \tag{2.42}$$

where V(x) is the Higgs potential

$$V(x) = -\mu^2 \left(\phi^\dagger(x)\phi(x)\right) + \lambda \left(\phi^\dagger(x)\phi(x)\right)^2 \tag{2.43}$$

μ being the Higgs mass parameter and λ the Higgs self-coupling parameter. If $\mu^2 > 0$ the potential V(x) possesses a local maximum at $\phi(x) = 0$ and a circle of absolute minima. The form of the potential is shown in Figure 2.1. It is often referred to as the Mexican hat potential because of its shape. The circle of minima dotted in the figure is at

$$\phi_0(x) = \sqrt{\frac{-\mu^2}{\lambda}} \exp\left(i\theta\right) \tag{2.44}$$

[8] Goldstone's conjecture: if there is continuous symmetry transformation under which the Lagrangian is invariant, then either the vacuum state is also invariant under the transformation, or there must exist spinless particles of zero mass [30].

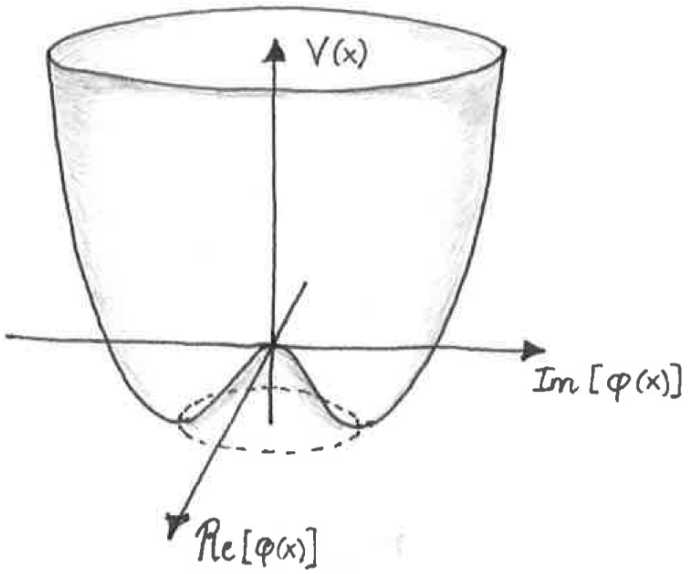

Figure 2.1: The form of the Higgs potential, showing the Mexican hat shape

where the angle θ defines a direction in the complex $\phi(x)$-plane.

Using the BEH mechanism, the fields $W^{\pm}(x)$ and $Z^0(x)$ acquire mass and the photon field $A(x)$ is recovered and remains massless. The choice of vacuum state leads to the familiar $U(1)$ after symmetry breaking, as is required, and hides the underlying $SU(2)_L \otimes U(1)_Y$. This results in a massive spin zero boson entering the theory, the Higgs boson. For a more detailed description of the BEH mechanism the reader is referred to Ref. [20].

2.5 Problems with the Standard Model

Trying to find a theory of everything, a theory that can describe any physical phenomenon, is of course the holy grail of theoretical (as well as experimental) particle physics. Experimental evidence continues to support the SM, and a big part of analysis in particle physics focuses on precision measurement of cross sections, charges and other features of the SM. Studies for the charge asymmetry measurement in top quark pair production in pp collisions at $\sqrt{8}$ TeV using the ATLAS detector at CERN, see Chapter 4, are presented in Appendix 1. These studies where conducted as part of a summer student program at CERN between

June and August 2013, under the supervision of Dr. Umberto De Sanctis and Dr. Richard Hawkings. Measurements of SM values are important tests of the SM predictions, but can also be very sensitive to new physics. The SM, as it stands today, is not complete. The model does not provide complete answers to all of our questions about matter, forces and the universe. These are just some of the main problems we are left with:

Free parameters The SM has a number of arbitrary elements, such as the weak mixing angle θ_W, the fermion masses and the mass of the Higgs boson. These have to be integrated in the theory from experimental data.

CP-violation The world as we know it can only exist because there is an abundance of matter compared to anti-matter. Charge Parity (CP)-violation, the violation of the Charge conjugation Parity symmetry, explains the matter anti-matter asymmetry to some extent, but can only account for a small fraction of it. Where the rest of this asymmetry comes from is not understood.

The generation problem The SM offers no explanation as to why there are three generations of fermions.

Gravity The theory incorporates only three out of the four fundamental forces, omitting the gravitational force.

Dark sector As explained in Chapter 1, and shown in Figure 1.2, astrophysical observations indicate the existence of a huge amount of non-luminous matter. Many experiments are conducting direct and indirect searches for dark matter, and there is no shortage of models with dark matter candidates, but none of these are included in the SM. The dark energy is a big mystery, believed to be responsible for the increasing expansion of the universe, but the SM lacks in an explanation for this as well.

The hierarchy/fine-tuning problem The combined mass measurement derived from $H \to \gamma\gamma$ and $H \to ZZ^{(*)} \to 4$ leptons in the ATLAS detector is $m_H = 125.5 \pm 0.2$ (stat) $^{+0.05}_{-0.06}$ (syst) GeV [31]. Theoretically, the bare mass of the Higgs boson is given by $m_H = 2v^2\lambda$, where v is the vacuum expectation value of the potential in Eq. 2.43 and Figure 2.1. This bare mass is subject to loop corrections from intermediate particles. For a fermion that couples with the Higgs-field with λ_f, as shown in Figure 2.2a, the correction is given by Eq. 2.45 and for a scalar particle coupling to the Higgs-field with $\lambda_{\tilde{f}}$, as shown in Figure 2.2b, it is given by Eq. 2.46 [32]

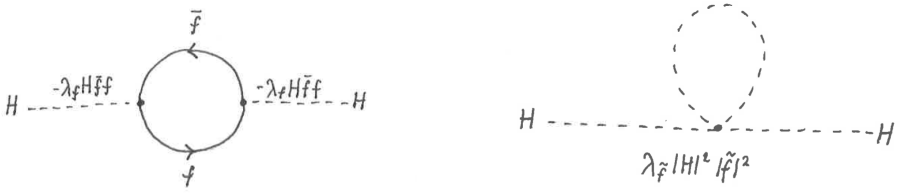

(a) Fermionic loop

(b) Scalar loop

Figure 2.2: Possible one-loop corrections to the m_H^2 parameter

$$\Delta m_H^2 = -\frac{|\lambda_f|^2}{8\pi^2}\left[\Lambda_{UV}^2 - 3m_f^2 \ln\frac{\Lambda_{UV}}{m_f} + \dots\right] \tag{2.45}$$

$$\Delta m_H^2 = \frac{\lambda_{\tilde{f}}}{16\pi^2}\left[\Lambda_{UV}^2 - 2m_{\tilde{f}}^2 \ln\frac{\Lambda_{UV}}{m_{\tilde{f}}} + \dots\right] \tag{2.46}$$

where Λ_{UV} is the ultraviolet cut-off scale, at which the mass corrections are no longer correctly described by the SM. The limit of the SM is reached at the Planck-scale[9], at the latest, where quantum effects of gravity become comparable to the electroweak forces. If Λ_{UV} is of the order of M_{Planck} the corrections to m_H are about 30 orders of magnitude larger than the measured m_H. The loop-corrections in Eq. 2.45 and Eq. 2.46 are of opposite sign, which in principle allows for cancellation between fermionic and bosonic contributions to Δm_H^2. The problem is that extreme fine-tuning of the SM particle masses is required to achieve the desired cancellations.

The Grand Unification The electromagnetic, weak and strong coupling constants of the SM appear to change with energy scale: they are running coupling constants. Extrapolated, the coupling constants almost unify at a large scale, M_{GUT}, but not quite. Beyond-SM models where the running coupling constants unify are called Grand Unification Theories (GUT). A unification of the coupling constants would reduce the number of free parameters in the SM.

[9] $M_{\text{Planck}} = 10^{19}$ GeV

Chapter 3

Supersymmetry

When particle physicists are given the chance to name something, they sometimes get carried away, just a little bit. Quarks ended up with names like charm and strange, and the acronym for weakly interacting particle is cleverly set to WIMP. Other times, if a process or theory is a special case or extension of something well known, hard to find, hard to describe, or just impressive, and creativity is low its name is prefixed "super". There are superconducting materials, there is superfluid helium, there is superallowed β decay and there is supersymmetry (SUSY).

Symmetries implement constraints on the structure of a theory. SUSY is a symmetry that relates space and time to superpartner directions of space and time. It relates spin-1/2 fermions and integer spin bosons to each other. SUSY has been a popular idea amongst theoretical physicists for a long time and for a number of reasons. It is an attractive possibility that can remedy many shortcomings of the SM.

This chapter opens with a brief introduction to SUSY. To have a hope of detecting or excluding SUSY models in ATLAS data, the theory must be realised at a mass scale in the TeV regime. Section 3.1.1 provides motivation for SUSY at this energy scale. This is followed by a short phenomenological introduction to the minimal supersymmetric extension of the standard model (MSSM). Section 3.2 takes a look into how SUSY could be broken and introduces one specific model: mSUGRA.

3.1 A brief introduction to Supersymmetry

The particles of the SM do not only follow the internal symmetries described in Chapter 2; they are also subject to external space-time symmetries for rotation, boosts and translation in four-dimensional space-time. A supersymmetric transformation will turn a fermionic state into a bosonic state and a bosonic state into

a fermionic state. The SUSY operator, Q, must be an anticommuting spinor in order to relate bosonic and fermionic states in this way.

$$Q|\text{fermion}\rangle = |\text{boson}\rangle \qquad Q|\text{boson}\rangle = |\text{fermion}\rangle \tag{3.1}$$

The Haag-Lopuszanski-Sohnius extension [33] of the Coleman-Mandula no-go [34] states "space-time and internal symmetries cannot be combined in any but a trivial way", restricting the form of SUSY. For the SM, with chiral fermions (i.e., fermions whose left- and right-handed pieces transform differently under the gauge group), this theorem implies that the generators Q and $Q^\dagger$ must satisfy an algebra of (anti-)commutation relations[1]

$$\left\{Q, Q^\dagger\right\} = P^\mu, \quad \{Q, Q\} = \left\{Q^\dagger, Q^\dagger\right\} = 0 \quad \text{and} \quad [P^\mu, Q] = \left[P^\mu, Q^\dagger\right] = 0 \tag{3.2}$$

where P^μ is the four-momentum generator of spacetime translation. As the operators Q and $Q^\dagger$ also commute with generators of the gauge transformations, particles and their superpartners have the same charge, weak isospin and colour. They also participate in the same interactions. The partners can be shown to have the same number of degrees of freedom [32], which leads to them differing only by spin.

3.1.1 Motivation for SUSY at the TeV-scale

Fine tuning of the SM was described in Section 2.5. The loop-corrections in Eq. 2.45 and Eq. 2.46 were of opposite sign, which in principle would allow for cancellation between fermionic and bosonic contributions to Δm_H^2, but fine tuning of the SM particle masses was required. This fine tuning appears unnatural, but SUSY has a solution. The MSSM predicts one supersymmetric partner to every SM particle that differs by half an integer spin. The bosonic and fermionic loop corrections cancel if there are equal numbers of bosons and fermions with identical couplings. For complete cancellation SUSY has to be an exact symmetry, which , as explained in Section 3.2, it is not. For reasonable calculationwithout too much fine tuning SUSY should then be realised at TeV scale.

TeV-scale SUSY could also provide unification of the SM gauge couplings at an energy scale $M_{GUT} \sim 10^{16}$ GeV which would limit the number of free parameters of the SM. This is illustrated in Figure 3.1, where the running coupling constants of the SM are extrapolated to high energies. The graph shows the extrapolation of the inverse of the SM coupling constants to high energies for the SM (dashed lines) and the MSSM (solid lines). For the MSSM, two scenarios are shown: one

[1] Spinor indices are suppressed for simplicity.

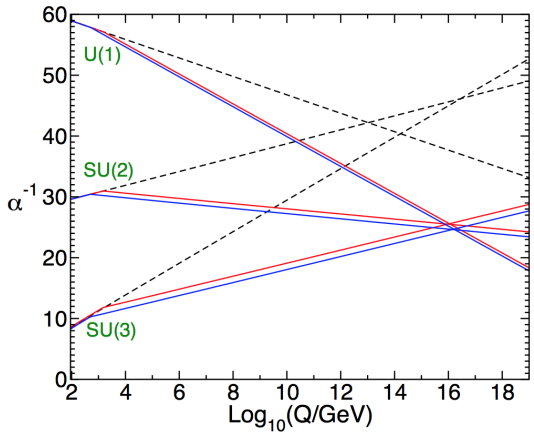

Figure 3.1: Evolution of the running coupling constants of the three gauge groups in the Standard Model (dashed lines) and the MSSM (solid lines). The solid blue lines show couplings in the MSSM with common sparticle masses of 500 GeV, the red for common sparticle masses of 1.5 TeV. The graphic is taken from Ref. [32]

with common sparticle masses of 500 GeV (blue) and one for common sparticle masses of 1.5 TeV (red). Sparticles are the supersymmetric partners of the SM particles in MSSM.

The lightest supersymmetric particle (LSP) could be a natural candidate for dark matter under certain conditions mentioned below. In order to make up for the dark matter observed in the universe today, the DM particles should be non-relativistic. This indicates that sparticles have high masses.

3.1.2 R-parity

Weak scale superpartners introduce lepton and baryon number violation that could lead to unstable protons, which would be disasterous. These particles that make up the world around us have to be stable, or very long-lived. The lower bound on the proton mean life time is $\tau > 2.1 \times 10^{29}$ years [3]. One of the reasons why SUSY is such an alluring theory is that it could provide a candidate for dark matter. This also requires a mechanism to keep the LSP stable. This is where R-parity comes in. The new quantum number is defined as

$$P_R = (-1)^{2s+3B+L}$$

where B, L and S are baryon number, lepton number and spin respectively. Standard Model particles have $P_R = +1$ whereas SUSY particles have $P_R = -1$. R-parity is, for the mSUGRA model investigated in this thesis, conserved. This means SUSY particles can only be created and destroyed in pairs, leaving the LSP stable. If the LSP is neutral under colour and electric charge as well, i.e. it does not interact through either the strong or electromagnetic forces, then it constitutes a good dark matter candidate.

3.1.3 MSSM

The minimal supersymmetric extension of the SM, MSSM, is the extension with minimal particle content. Together the SM particle and the superpartner form a supermultiplet. In the MSSM, each of the known fundamental particles is in either a chiral or gauge supermultiplet, and must have a superpartner with spin differing by 1/2 unit. Chiral multiplets are formed by the fermions of the SM and their superpartners, which have spin zero. The naming convention is to use the same name as their SM partner and adding a "s-" prefix, i.e. electron → selectron. The gauge multiplets are formed from the gauge bosons of the SM and their superpartners. These superpartners carry spin 1/2 and are named after their SM partner plus the suffix "-ino", i.e. photon → photino.

Name	Spin	P_R	Gauge Eigenstates	Mass Eigenstates
Higgs Boson	0	+1	$H_u^0\ H_d^0\ H_u^+\ H_d^-$	$h^0\ H^0\ A^0\ H^\pm$
Squarks	0	-1	$\widetilde{u}_L\ \widetilde{u}_R\ \widetilde{d}_L\ \widetilde{d}_R$	(same)
			$\widetilde{s}_L\ \widetilde{s}_R\ \widetilde{c}_L\ \widetilde{c}_R$	(same)
			$\widetilde{t}_L\ \widetilde{t}_R\ \widetilde{b}_L\ \widetilde{b}_R$	$\widetilde{t}_1\ \widetilde{t}_2\ \widetilde{b}_1\ \widetilde{b}_2$
Sleptons	0	-1	$\widetilde{e}_L\ \widetilde{e}_R\ \widetilde{\nu}_e$	(same)
			$\widetilde{\mu}_L\ \widetilde{\mu}_R\ \widetilde{\nu}_\mu$	(same)
			$\widetilde{\tau}_L\ \widetilde{\tau}_R\ \widetilde{\nu}_\tau$	$\widetilde{\tau}_1\ \widetilde{\tau}_2\ \widetilde{\nu}_\tau$
Neutralinos	1/2	-1	$\widetilde{B}^0\ \widetilde{H}^0\ \widetilde{H}_u^0\ \widetilde{H}_d^0$	$\widetilde{\chi}_1^0\ \widetilde{\chi}_2^0\ \widetilde{\chi}_3^0\ \widetilde{\chi}_4^0$
Charginos	1/2	-1	$\widetilde{W}^\pm\ \widetilde{H}_u^+\ \widetilde{H}_d^-$	$\widetilde{\chi}_1^\pm\ \widetilde{\chi}_2^\pm$
Gluinos	1/2	-1	$\widetilde{g}$	(same)
Goldstino (Gravitino)	1/2 (2/3)	-1	$\widetilde{G}$	(same)

Table 3.1: The undiscovered particles in the MSSM

It seems logical for the Higgs scalar boson to reside in a chiral supermultiplet since it has spin 0. Actually, it turns out that just one chiral supermultiplet is not enough. Only one Higgs chiral supermultiplet would lead to a gauge anomaly of the electroweak gauge symmetry making it inconsistent as a quantum theory [32]. Two Higgs supermultiplets, H_u and H_d, could be the solution. The Higgs supermultiplets are also required for all the sparticles to acquire their masses.

The fermionic superpartners of the Higgs are called higgsino following the naming convention of the gauge multiplet sparticles.

The gaugino and higgsino mass eigenstates will mix due to effects from electroweak symmetry breaking and SUSY breaking. This results in four neutral and two charged mass eigenstates, referred to as neutralinos, $\widetilde{\chi}_i^0$, and charginos, $\widetilde{\chi}_j^{\pm}$, $i = 1, 2, 3, 4$, $j = 1, 2$. The gauge eigenstates and mass eigenstates of the MSSM are listed in Table 3.1, excluding gravitinos.

3.2 Breaking SUSY

If SUSY was an exact symmetry, SUSY and SM particles would then have the same mass. Experiments would (or should) already have found the superpartners of the SM particles. Since thus far there is no evidence for selectrons or other supersymmetric particles at a similar mass as their SM partner, the assumption is that SUSY is broken. Breaking SUSY is fairly technical and this section will not go into too much detail.

Bosons and fermions of the SM do not belong to similar representations. Because of this, it is very important to establish how SUSY is broken. In either case there will be a mass scale, M_{SUSY}, associated with the SUSY breaking effects. If the energy is larger than this scale the theory is supersymmetric and if it is lower: it is back to the SM. In MSSM, SUSY is believed to be broken spontaneously in order to preserve the underlying structure of the theory. Furthermore, there are no *a priori* constraints on the form of the breaking term, apart from that it should be soft, i.e. preserving the regulating features of supersymmetry.

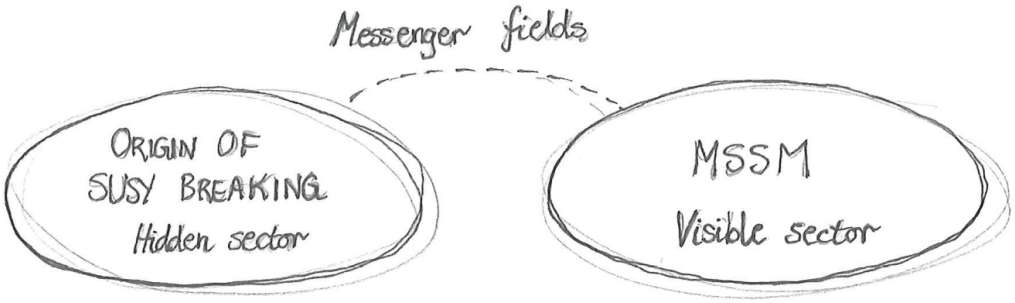

Figure 3.2: A conseptual illustration of the process of SUSY breaking in the MSSM.

The breaking is assumed to happen in a hidden sector, meaning that the fields

responsible for breaking supersymmetry are singlets under the $SU(3) \times SU(2) \times U(1)$ group of the SM, or they are very heavy and out of the scope of accelerator research. The breaking is then mediated to the visible sector by a messenger field, as illustrated in Figure3.2. Different messenger fields have been proposed such as gravity-, gauge- and anomaly mediated supersymmetry breaking. These frameworks minimise the number of additional parameters imposed by supersymmetry breaking.

3.2.1 mSUGRA

The messenger field in the Minimal Supergravity model (mSUGRA) is gravity. Gravitational interaction is the most economical mechanism for transmitting the breaking of SUSY, and mSUGRA is the simplest of models with this breaking mechanism.

The parameter space of the MSSM has 127 free parameters [21]. This number of free parameters is too high to be effectively searched. To counteract this, theories have been developed that reduce the parameter space based on certain assumptions. mSUGRA has only five free parameters, on top of the 27 free parameters in the SM, already a great "improvement" over the MSSM. To a reasonable approximation, the entire mass spectrum in mSUGRA models is determined by only five unknown parameters:

m_0 - a universal scalar mass at M_{GUT}

$m_{1/2}$ - a universal gaugino mass at M_{GUT}

A_0 - a common value for all trilinear couplings in the Lagrangian

$\tan\beta$ - the ratio between the two Higgs doublet vacuum expectation values

$\text{sign}(\mu)$ - the sign of the Higgs mass parameter μ

In mSUGRA squarks, sleptons and Higgs bosons have a common mass, m_0, whilst gauginos have a common mass $m_{1/2}$, at GUT scale. The common masses split into the separate sparticle masses at the weak scale through renormalistaion group equations (RGEs). Figure 3.3 shows the RGE evolution of scalar and gaugino masses in a typical model based on the mSUGRA boundary conditions imposed at $Q_0 = 2 \times 10^{16}$ GeV. The parameter values used for this illustration were $m_0 = 200$ GeV, $m_{1/2} = -A_0 = 600$ GeV, $\tan\beta = 10$, and sign(μ)=+. The solid lines labelled by M_1, M_2, and M_3 are running gaugino masses. The dot-dashed lines labelled H_u and H_d are the running values of the quantities $(\mu^2 + m_{H_u}^2)^{1/2}$ and $(\mu^2 + m_{H_d}^2)^{1/2}$, which appear in the Higgs potential. The other lines are the running squark and slepton masses [32].

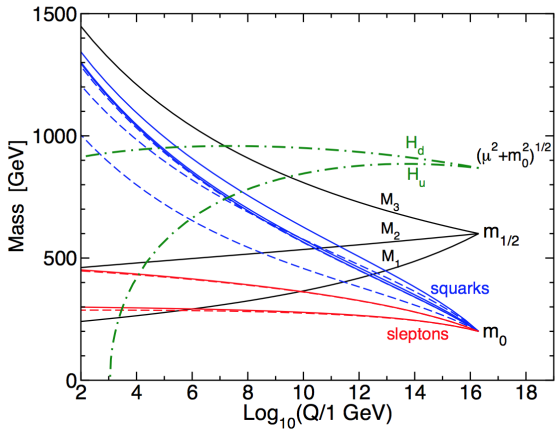

Figure 3.3: Evolution of scalar and gaugino mass parameters in the MSSM with mSUGRA boundary conditions imposed at M_{GUT}. The parameter $\mu^2 + m_0^2$ runs negative, provoking electroweak symmetry breaking. The graphic is taken from Ref. [32]

3.3 Tau leptons in SUSY

Despite lepton universality tau leptons might provide unique signatures in many SUSY models. If SUSY is, as argumented for in Section 3.1.1, realised at a relatively low energy scale, the third generation sfermions are expected to be the lightest sleptons. This is expected to cause the production rate to final states with taus to exceed the production rate into final states with electrons or muons. Naturalness arguments [35] suggest that the light third-generation sparticles should have masses of a few hundred GeV. This would protect the Higgs boson mass from quadratically divergent quantum corrections.

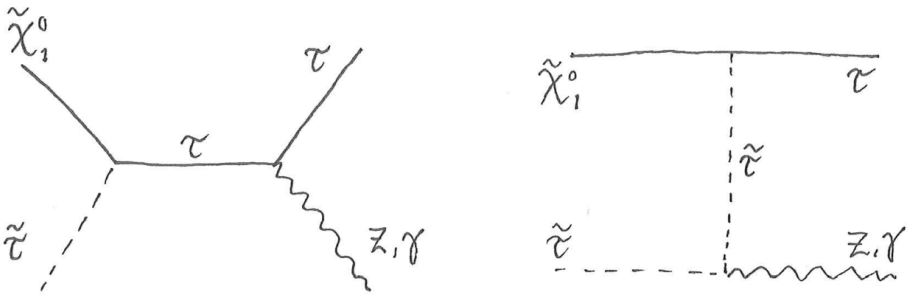

Figure 3.4: Feynman diagrams showing contributions to the oannihilation of the neutralino, $\tilde{\chi}_1^0$.

Light sleptons could also play a role in the co-annihilation of neutralinos. In certain models and certain regions of the parameter ace the difference in the mass of the tau slepton and the mass of the neutralino, here being the LSP, is small. This would allow the two particles to annihilate in the early universe. Feynman diagrams of some of the co-annihilation processes can be seen in Figure 3.4. The neutralino as a dark matter candidate has the feature that its cosmological relic density naturally falls in the range allowed by cosmology and preferred by astrophysics in some domains of the MSSM parameter space [36]. A consequence of the small difference in mass is that the experimental sensitivity is biased towards low momenta of at least one tau lepton. This means there will be fewer detectable tau candidates in the final state. If squarks and gluinos have masses within reach of the LHC, their production rates could be dominant and they could decay in cascades involving light tau sleptons, high transverse momentum jets and missing transverse momentum from the LSP [37].

Chapter 4

The experiment

Theoretical particle physicists can think up all the theories their hearts desire, but if these are not testable, no scientific hypothesis can be proposed. To probe the tiny distances scientists are faced with in particle physics, high energies are required. The heavier the particle produced, the higher the energy of the collision must be. The experimental tools available are cosmic rays, nuclear reactors, particle accelerators and various particle detectors. This chapter will present the reader with a short introduction of the particle physics laboratory CERN [1] (European Organization for Nuclear Research), followed by an overview of the particle collider LHC (Large Hadron Collider), and the particle detector ATLAS (A Toroidal LHC Apparatus).

4.1 CERN

This year, 2014, the biggest particle laboratory in the world is celebrating 60 years of existence. After the second world war, European science was no longer top of the class. Scientists such as Niels Bohr from Denmark and Pierre Auger from France imagined creating a European atomic physics laboratory that would unite European scientists, as well as allow them to share the increasing economic burden nuclear physics facilities represented. The first official proposal was put forward by French physicist Louis de Broglie in 1949, and on 29 September 1954 CERN officially came into being [38].

Initialy, CERN had 12 member states. Today CERN has 21 member states, with Romania as a candidate and Serbia as an associate member in the pre-stage to membership. Other countries have the status of observer state, non-member states with co-operation agreements or non-member states with scientific con-

[1] CERN is the acronym derived from the French name: "Conseil Européen pour la Recherche Nucléaire".

tacts, and about 10,000 visiting scientists from over 113 countries come to CERN to do research [39].

The first particle accelerator in operation at CERN was the 600 MeV synchrocyclotron (SC), built in 1957. The second particle accelerator, the Proton Synchrotron (PS), started operation in 1959. This accelerator is still part of the accelerator complex that feeds the LHC, as shown in Figure 4.1. In 1965 the first antinuclei, antideuteron, was observed simultaniously by two experiments, one using the PS at CERN [40] and the other using the Alternating Gradient Synchrotron (AGS) accelerator at the Brookhaven National Laboratory [41].

The next big achivement to take place at CERN was the world's first recording of interactions from colliding protons. This was reported by Kjell Johnsen, the leader of the Intersecting Storage Rings (ISR), on January 1971. The ISR also produced the world's first proton-antiproton collisions in 1981, paving the way for proton-antiproton collisions in the Super Proton Synchrotron (SPS). The SPS, which started up in 1976, is at the moment the last part of the accelerator complex leading up to the LHC. In a seminar at CERN in July 1973, Paul Musset of the Gargamelle collaboration presented the first direct evidence of the weak neutral current. Neutral currents are only present in unified electroweak theory, and this confirmed the existence of the Z boson before its discovery in proton-antiproton collisions in the SPS by the detector UA1 at CERN in 1983. The W boson that mediates charged current interactions was discovered in the same experiment. These were the discoveries for which Rubbia and van der Meer were rewarded the Nobel prize, only one year later. LEP measurements also led to precise predictions of the mass of the, then, undiscovered top quark and bounds on the Higgs mass.

With its 27-kilometre circumference, the Large Electron-Positron (LEP) collider was the largest electron-positron accelerator ever built, both when it had its first injection in 1989, and today, 14 years after its final shutdown. Up until 2000, LEP and its experiments provided a detailed study of the electroweak interaction based on solid experimental foundations. The number of families of light neutrinos was determined to be consistent with the Standard Model value of 3. Another important facility at CERN is the Low-Energy Antiproton Ring (LEAR), where in 1995 for the first time atoms of antihydrogen were created. In 2001, the NA48 collaboration published a paper on the discovery of direct CP violation [42].

The LHC went live in September 2008, but a faulty electrical connection led to a magnet quench and several tons of helium gas escaping. Proton beams were successfully collided in November 2009. For a more detailed description of the history and technicalities of the LHC, the reader should be referred to Section 4.2. On July 4th 2012 the two LHC mulitpurpose experiments, ATLAS and CMS (Compact Muon Solenoid), could happily announce the discovery of a Higgs like

particle to a full CERN main auditorium[2]. Peter Higgs, François Englert, Gerald Guralnik and Chris Hagen were all in the audience. In 2013, the Nobel prize in physics was awarded to Peter Higgs and François Englert "for the theoretical discovery of a mechanism that contributes to our understanding of the origin of mass of subatomic particles, and which recently was confirmed through the discovery of the predicted fundamental particle, by the ATLAS and CMS experiments at CERN's Large Hadron Collider" [43]. For more on the Higgs boson, see Section 2.4.

The last exciting result to come from CERN is the confirmation of the existence of exotic hadrons[3]. On April 9th the Large Hadron Collider beauty (LHCb) presented a Z(4430) signal with a significance of at least 13.9 σ [44].

4.2 The Large Hadron Collider

On the Swiss-French border, about 100 m under ground, subatomic particles are accelerated to near the speed of light. The LHC [45–47] is a 27 km circular accelerator, a synchrotron storage ring designed to collide protons[4] at a center-of-mass ($\sqrt{s}$) energy of 14 TeV with a luminosity of $\mathcal{L} = 10^{34}\text{fb}^{-1}$. At the time when this thesis was written, the LHC is in shut-down. The accelerator and its experiments are being upgraded to deal with the complications of moving from $\sqrt{s} = 8$ TeV to $\sqrt{s} = 14$ TeV, and to a luminosity of $\mathcal{L} = 10^{34}\text{fb}^{-1}$. But wait. Was it not written, two lines back, that the LHC was designed for the exact energy and luminosity it is now being upgrated for?

2008, on the 10th of September, the LHC started up. Protons were collected from the hydrogen source, a simple bottle of hydrogen gas. An electric field stripped the hydrogen atoms of their electrons before the protons were boosted through the accelerator complex shown in Figure 4.1, and injected into the LHC. Physicists all over the world were ready to find the Higgs, a dark matter candidate, a supersymmetric particle, or maybe just a signal that the beam got all the way around the ring. Nine days later, during powering tests of the main dipole circuit in one of the sectors of the LHC, a fault occurred in the electrical bus connection in the region between a dipole and a quadrupole, resulting in magnet quenching[5] and release of helium from the magnet into the tunnel. The LHC

[2]I was there. People slept outside the Main Auditorium to secure good seats. Talk about crazy fans! Better than any concert.

[3]Exotic hadrons are subatomic particles, made of quarks, that are not mesons or baryons, see Section 2.2

[4]The LHC also has a heavy ion program.

[5]Quenching refers to what happens when the liquid cryogens that cool the superconducting magnet coils boil off rapidly. This results in helium escaping from the cryogen bath, and the coils cease to be superconducting and become resistive.

would not start up again until Novermber 2009. The PS accelerated protons to the energy of to 1.4 GeV and the SPS to 450 GeV, before the protons were finally transferred to the two beam pipes of the LHC, each beam reaching an energy of 3.5 TeV. The 7 TeV center-of-mass energy was kept at this level until the end of 2011, when it was cranked up to 8 TeV. The accelerator comeplex in Figure 4.1 includes the Antiproton Decelerator (AD) and the Isotope mass Separator On-Line facility (ISOLDE), and fed the CERN Neutrinos to Gran Sasso[6] (CNGS) project and the Compact Linear Collider (CLIC) test area, as well as the neutron time-of-flight facility (nTOF).

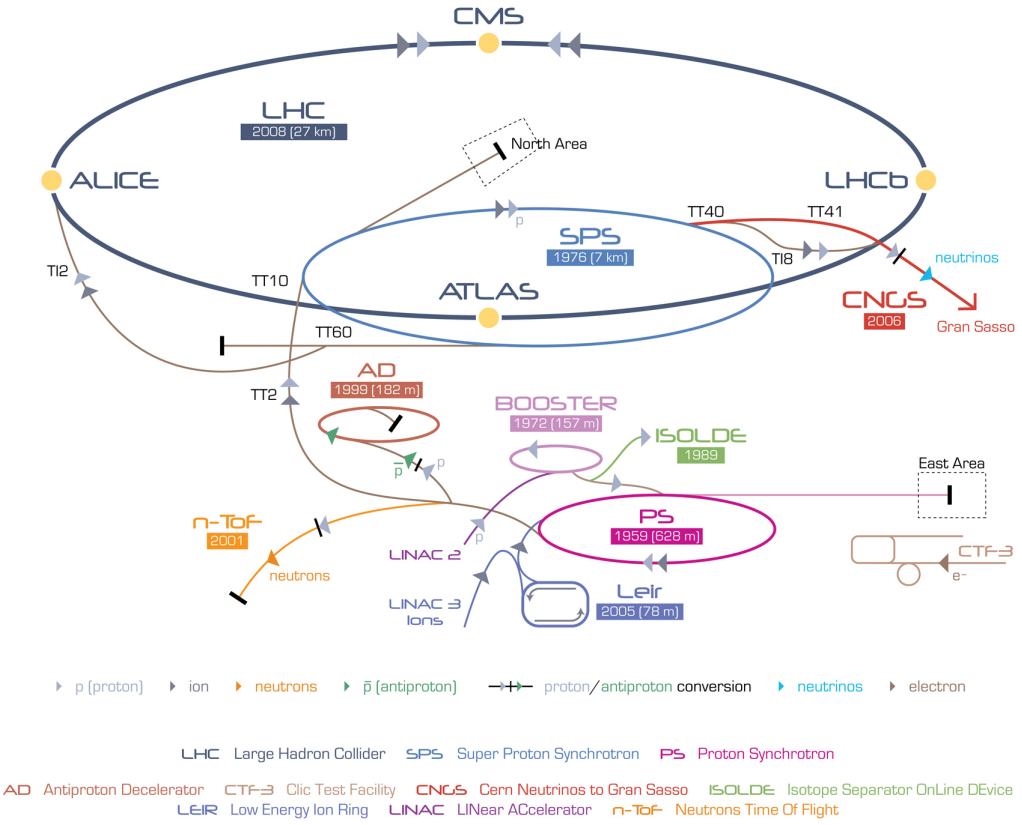

Figure 4.1: The CERN accelerator complex. The image shows the injector system for LHC, the LHC itself and the experiments connected to this accelerator complex. The image is taken from ref. [48].

Protons entering the LHC are accelerated in radiofrequency (RF) cavities. Protons with slightly different energies arriving earlier or later will be accelerated

[6]The reader may have heard of this facility when, in 2011, the OPERA collaboration released a preprint reporting faster-than-light (tachyon) neutrinos. It later turned out the results could be attributed to a faulty element of the experiment's fibre optic timing system.

or decelerated so that they stay close to the energy of the ideal particle. The LHC consists mostly of superconducting magnets. In a synchrotron, dipole magnets bend the particles around the ring, while quadrupole systems maintain the collimation of the beam. Thousands of huge, custom-built electromagnets focus particle beams and guide them around the bends. The world's largest cryogenic system cools magnets on the Large Hadron Collider (LHC) to close to absolute zero, so that the wires supplying their electricity can work in a superconducting state, without losing energy due to resistance. More than 50 types of magnets are needed to send them along complex paths without their losing speed. In this way, the particle beam is sorted into discrete packets called bunches. By design, the LHC beam would be segmented into about 2808 bunches per beam, each bunch containing approximately 1.15×10^{11} protons. The bunch spacing is, by design, 25 ns, which means bunches cross every 25 ns. For most of run 1 the bunch spacing was 50 ns, the number of protons per beam was 1.2-1.7$\times10^{11}$ and there were 1380 bunches per beam.

The proton beams can circulate for many hours inside the LHC beam pipes under normal operating conditions. The two beams are brought into collision inside four detectors – A Large Ion Collider Experiment (ALICE), ATLAS, CMS and LHCb, represented by yellow dots on the LHC in Figure 4.1. These are the main experiments at the LHC. ATLAS and CMS are general purpose experiments with similar physics programs which means they can confirm observations of the other experiment, as they did with the Higgs in 2012. LHCb and ALICE have more specific physics programs. ALICE is designed to investigate the physics of strongly interacting matter at extreme energy densities, the physics of quark-gluon plasma. ALICE can be run in proton collisions, but is outlined for the heavy ion program of the LHC. LHCb is dedicated to b-physics.

Prior to each collision point the two beams are squeezed by magnets. This results in an extreme proton density that ensures a high collision rate. This collision rate is described by the instantaneous luminosity, $\mathcal{L}$. For any given process of cross section σ, the event rate dN/dt is described by

$$\frac{d}{dt}N = \mathcal{L}\,\sigma \tag{4.1}$$

The instantaneous luminosity is the proportionality factor between the event rate and the cross section. If N_b bunches containing N_1 and N_2 particles collide with a frequency f, and $\sigma_{x,y}$ are the root mean square beam sizes at the collision point in the x- and y-direction respectively, the luminosity in the interaction region is given by [49]

$$\mathcal{L} = f\frac{N_b N_1 N_2}{\sigma_x \sigma_y} \tag{4.2}$$

Of course this is a simplified formula. There are additional complications in real

machines. Collisions are generally not head on, so the transverse beam offset and crossing angle must be taken into consideration. The two particle beams in the LHC cross at an angle in all experimental interaction points, to avoid unwanted collisions. Other factors to take into consideration are the fact that beam profiles can deviate from a Gaussian function, that beam density functions in the transverse and longitudinal planes can be correlated and that there is a non-zero dispersion at each collision point. The design luminosity of the LHC is $\mathcal{L} = 10^{34}$ cm^{-2} s^{-1}.

The integrated luminosity is a measurement of the collected data size, and it is an important value to characterise the performance of an accelerator

$$\mathcal{L}_{int} = \int_0^T f(t)dt \tag{4.3}$$

It is connected to the number of events in interest in the following way

$$\mathcal{L}_{int}\,\sigma = \text{number of events of interest} \tag{4.4}$$

This integral in Eq. 4.3 is taken over sensitive time, excluding deadtime. For collisions with $\sqrt{s} = 7$ TeV there is an integrated luminosity of about 7 fb^{-1} of proton-proton data, and for the 2012 $\sqrt{s} = 8$ TeV run there was an integrated luminosity of 23.3 fb^{-1} delivered to both ATLAS and CMS [50].

CERN's long term plan for the LHC is first of all to go to run 2, with the LHC working at the conditions they were designed for. The next step is the High Luminosity LHC (HL-LHC), an upgrade planned to be finished in 2020 for what will be run 3. With this upgrade the luminosity is to be increased by a factor of 10 beyond the design value. The CERN Courier could on 22 January 2014 report that "The HL-LHC project is currently in the design and prototyping phase and should release a Preliminary Design Report in the middle of 2014, with the Technical Design Report for construction at the end of 2015" [51].

4.3 ATLAS

ATLAS is the experimental setup within which this thesis was written. The following sections will give a short explanation of the geometry and substructures of the detector, how the particle signatures are measured and interpreted and what the plans are for upgrades at this moment in time, and in the future.

This huge general purpose detector, the largest detector at the LHC, measures 25m in height and width, and 46m in length. In Figure 4.2 two (computer generated) women and two men are placed next to the detector for comparison. After a collision large amounts of newly created particles splash out in all directions. To be capable of detecting the majority of these particles good hermeticity

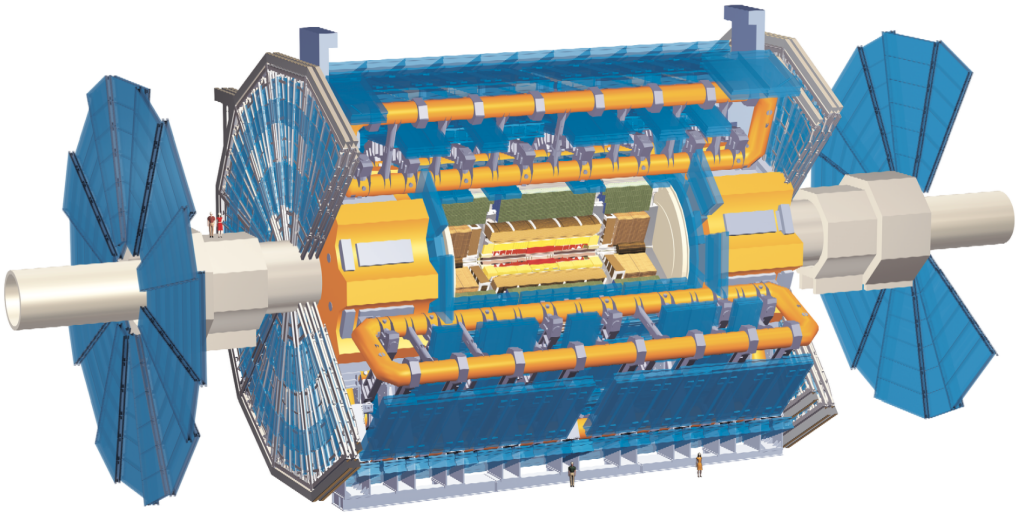

Figure 4.2: Computer generated detailed view of the ATLAS detector. The image is taken from ref. [52]

is required, the detector therefore must cover the entire solid angle surrounding the collision point. This can only be realized to a certain degree. The particle beams must enter and leave the detector somewhere, and as the idea is to have beams circulating the LHC for hours, material can not be put where the beam line is. A particle's energy should be measured, charge determined and one type discriminated against another. The layers should be arranged by transmissibility, from virtually invisible to completely opaque. When a particle stops in the detector, and the energy is measured, all other relevant information should have been retrieved in the previously transitted detector layers.

ATLAS has, as shown in Figure 4.3, a general layout where there is a barrel structure wrapped around the beam, centered at the interaction point. At both ends of the barrel, in what translates to high values of $|\eta|$ in the ATLAS coordinate system, see Section 4.3.1, detectors are also placed in the end-caps.

4.3.1 Coordinates

In the ATLAS detector the following right-handed Cartesian coordinate system is used. The z-axis is defined to be along the beam direction, and so the xy-plane

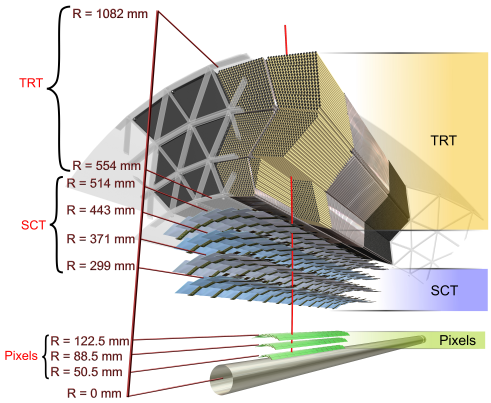

(a) ATLAS inner detector, ref. [53]

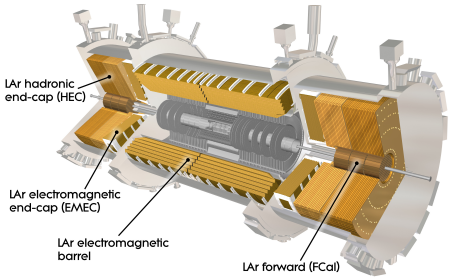

(b) Liquid Argon calorimeter, ref. [54]

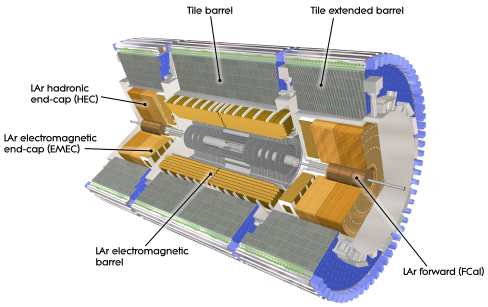

(c) Full ATLAS calorimeter, ref. [54]

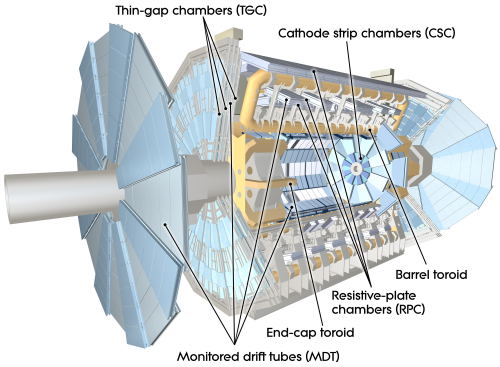

(d) Muon Spectrometer components, ref. [55]

Figure 4.3: Computer generated detail views of the ATLAS subdetectors

is perpendicular to the beam pipe. The y-axis points upwards, with respect to the plane defined by the LHC ring. The x-axis lies within this plane and is chosen to point towards the center of the accelerator ring.

The coordinate system can also be expressed in polar coordinates. r is the distance from the interaction point, θ is the polar angle measured from the beam pipe and the azimuthal angle, ϕ, is defined to increase clockwise around the z-axis.

$$x = r \sin\theta \cos\phi \qquad y = r \sin\theta \sin\phi \qquad z = r \cos\theta \tag{4.5}$$

The pseudorapidity, defined as

$$\eta = -\ln \tan \frac{\theta}{2} \tag{4.6}$$

is a spatial coordinate that is frequently used in proton-proton physics. Along the y-axis η=0, increasing in absolute value closer to the beam pipe. For a particle detector, like ATLAS, high coverage in η is desirable.

4.3.2 Inner Detector

The inner detector (ID) [56] of ATLAS comprises of three main parts: the Pixel Detector, the Semiconductor Tracker (SCT) and the Transition Radiation Tracker (TRT), as shown in Figue 4.3a. The inner detector tracks charged particles with a high efficiency over the pseudorapidity range $|\eta|<2.5$ as they move from the LHC beam-pipe to the electromagnetic (EM) calorimeter system. The inner detector is exposed to a 2 T solenoidal magnetic field[7] [57] aligned with the beam direction that deflects charged particles on circular paths. The radius of the track's curvature can be used to identify the particle's transverse momentum[8].

The Pixel Detector

The first detector a particle must traverse in ATLAS is the Pixel Detector. It is made up of three precision layers, of average radii of $\sim$ 5 cm, 9 cm and 12 cm, surrounding the beam line, and three disks at each barrel side, of radiuses between 9 cm and 15 cm. This way a charged particle will typically leave three signals [58]. The detector provides a high granularity, high precision set of measurements. All together there are 80 million silicon pixels covering an area of 1.7 m^2 in the 1456 modules in the barrel and 288 in the disks. These modules overlap on the support structure to give hermetic coverage. The most important job of the Pixel Detector is to determine the impact parameter needed to find short lived particles, like B-hadrons. The pixels are also designed to have a good resistance against radiation from the collisions, and to minimize multiple scattering [59].

The Semiconductor Tracker

The Pixel Detector is surrounded by layers of semiconductor microstrips, contributing to the measurement of momentum, impact parameter and vertex position. The SCT is constructed of 4088 silicon detector modules mounted on the barrel (four cylinders) and the end-caps (nine disks at each end of the barrel), for a total of 6.3 million silicon strips each with its own readout channel. The SCT covers $|\eta|< 2.5$, so that the particles pass through at least four layers [60].

[7] Tesla (T) is the SI unit of magnetic field strength

[8] Transverse momentum is the component of momentum perpendicular to the beamline, in the xy-plane defined in Section 4.3.1

The Transition Radiation Tracker

The outermost layer of the ID is the TRT, which operates mainly as a straw drift tube chamber. A charged particle moving through the TRT will ionize the Xenon gas inside one of the almost 300,000 straws. The electrons that are created drift towards the anode at the center of the straw, where they are read out [61]. There are 52,544 straws of 144 cm in the barrel, and 122,880 straws 37 cm in length in each end cap [62]. The straws in the barrel are arranged along the z-axis, so that they do not provide any information for η, but this information is not needed for determination of transverse momentum. The TRT has the biggest active volume of the ID components. This large spatial coverage can be afforded as it is a gaseous detector with long radiation length [63].

Central Solenoid

The ATLAS Central Solenoid (CS) is designed to produce a 2T longitudinal magnetic field at the center of the tracking volume of the ID. The magnet generates the bending power for the momentum measurement of charged particles. Since the EM calorimeter is situated outside the ID and CS, as shown in Figure 4.2, the winding must be as transparent as possible for traversing particles [64].

4.3.3 Calorimeters

Calorimeters measure the energy of particles. There are different types of calorimeters; homogenous shower counters and sampling shower detectors. Both the EM and hadronic calorimeter of ATLAS are sampling shower detectors. In these calorimeters the fluctuations of energy degradation and energy measurement are separated in alternating layers of different substances. There are layers of passive absorbers, where incoming particles interact with the material and create particle showers, and active or sensing layers, where the particles are detected as electric signals. Moving through a suitable calorimeter, a particle will decelerate, and when it eventually stops, its energy can be determined. As E_T^{miss},the energy of particles which can not be detected in a particle detector, is an important signature to many interesting physics scenarios, SUSY included, high coverage in $|\eta|$ is important for the calorimeters. The full ATLAS calorimeter is shown in Figure 4.3c.

Electromagnetic Calorimeter

The EM calorimeter in ATLAS aims to measure the energy deposition of electromagnetically interacting particles, i.e. all charged particles, as well as photons.

This sampling calorimeter uses Lead (Pb) for the passive layers, where the particle showers are created, and liquid Argon (LAr) as the active material. The liquid Argon is cooled down to a temperature of - 180°. When electromagnetically interacting particle traverse the LAr the Argon atoms are ionized. The liberated electrons drift to copper electrodes in an applied electric field, where they induce an electric signal proportional to the energy of the initial particle. The EM calorimeter has a barrel part and to end-cap parts, as shown in Figure 4.3b. Together they provide a $|\eta|< 3.2$ coverage [65]. The barrel of the LAr calorimeter is made of accordian shaped layers, subdivided into 182,468 smaller structures of fine granularity that allow for a very good spatial resolution of the substructures of an object, such as a jet [63]. This is very important for this anlysis, where discimination between hadronic jets and taus is vital, as explained in more detail in Chapter 5.

Hadronic Calorimeter

The hadronic calorimeter is dedicated to the energy measurement of hadrons. In the barrel, the hadronic calorimeter is a sampling calorimeter with passive layers of low-carbon steel and active layers of plastic scintillator tiles. This is called the Tile Calorimeter [66]. The particle showers excite the scintillating material, which re-emits the absorbed energy by luminescence.The light is collected by fibre cables and read out by photomultiplier tubes [63]. The main barrel covers $|\eta|< 1.0$, and the extended barrels on each side cover $0.8 <|\eta|< 1.7$. On each barrel end, the end-cap region is divided into a Hadronic End-cap Calorimeter (HEC) and a Forward Calorimeter (FCal). These cover different regions in pseudorapidity. The pseudorapidity range $1.5 <|\eta|< 3.2$ is covered by the hadronic LAr end-caps, shown in Figure 4.3b. In HEC the passive material is Copper. The FCal is integrated into the end-cap cryostats and covers $3.1 <|\eta|< 4.9$. It is approximately 10 interaction lengths deep, and consists of three modules in each end-cap: the first, made of copper, is optimised for electromagnetic measurements, while the other two, made of tungsten, measure predominantly the energy of hadronic interactions [67].

4.3.4 Muon Spectrometer

Due to their high mass, muons are minimal ionizing particles and penetrate the calorimeters. For this reason the Muon Spectrometer [68], shown in Figure 4.3d, is the outermost sub-system of ATLAS. It was designed and constructed to trigger and measure high momentum muons over a large pseudorapidity range that extends to 2.7. The spectrometer instrumentation is embedded in a set of superconducting air-core toroid magnets, providing an average field of 0.5 T. The

Toroid Magnet system consists of eight barrel coils, housed in separate cryostats, and two end-cap cryostats housing eight coils each. The toroidal geometry of the magnetic field allows for equal bending of the muon tracks, independent of production angle. This leads to constant momentum resolution within the η acceptance region. The open geometry of the air-toroids also minimizes the amount of material encountered by the muons, and so reduces multiple scattering and energy loss.

The barrel part of the muon spectrometer is made up of the layers of Monitored Drift Tubes (MDTs) that measure the trajectories of the muons. In the MDTs an Argon-based gas mixture is ionized along the muon's path. The liberated electrons are then collected on W-Re wires that run through each drift tube. Drift time information is used to determine the electron's starting point, and so the muon's position. Time of flight measurements are also performed by Resistive Plate Chambers (RPCs). In the end-caps tracking is done by the use of Cathode Strip Chambers (CSCs), and timing information by Thin Gap Chambers (TGCs). These are capable of coping with the higher occupancy in the forward regions [63].

4.3.5 Trigger System

A trigger is a system that very quickly decides, based on simple criteria, whether an interesting event has taken place. If so, the data-acquisition (DAQ) process is initiated. The LHC deliveres enormous amounts of data and the trigger system is designed to record events at approximately 200 Hz from the LHC's 40 MHz bunch crossing rate. When the design spacing between proton bunches is 25 ns and there are multiple collisions per crossing and the rate of "new physics" is low[9] it is not desirable to save every single event. Firstly, most of the saved events would be background events. Secondly, there is no room to store every event, which amounts to the order of 100,000 PB/year. Thirdly, reconstruction and analysis of this many events would take a very long time.

The ATLAS trigger system [69] has three levels; the first level (L1) is a hardware-based system that uses information from the calorimeter and muon sub-detectors, the second (L2) and third (Event Filter, EF) levels are software-based systems using information from all sub- detectors. Together, L2 and EF are called the High Level Trigger (HLT). Figure 4.4 shows a schematic of the ATLAS trigger system.

[9]Hopefully, otherwise particle physicists have misunderstood the SM completely.

Level 1

The first selection is made by the L1 trigger, and the trigger decision is formed by the Central Trigger Processor (CTP). The decision is based on reduced-granularity information from the calorimeter trigger towers and the dedicated triggering layers in the muon system.
The L1 trigger decision is distributed, with timing and control signals, to all ATLAS sub-detector readout systems. The CTP time-synchronizes the input from the different triggers, combine the inputs and introduces deadtime in a short time window surrounding an event accepted by L1 before it issues the final L1 decision. The deadtime is introduced because sending information to the DAQ, and too many events at once can clog the system and prevent new data from being analyzed. Detector data from events passing L1 is stored in detector specific Readout Buffers (ROBs), and one or more ROBs are grouped into Readout Systems (ROSs) which are connected to the HLT networks. In addition to making the first selections, L1 defines Regions of Interest (RoIs) within the detectors to be investigated by the HLT.

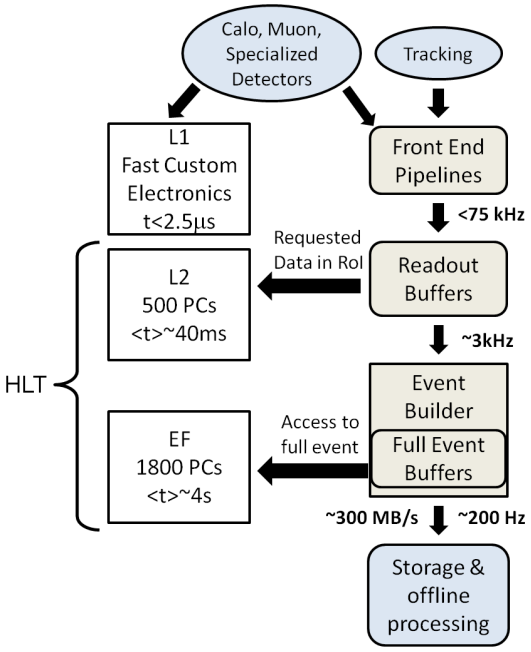

Figure 4.4: Schematic of the ATLAS Trigger System. The image is taken from ref. [69]

High Level Trigger

From L1 there is a large rate, up to 100 kHz, of events that could be interesting. These events are sent to the HLT for additional filtering. The HLT has more informational available than the L1, including inner detector hits, full information from the calorimeter and data from the precision muon detectors. The L2 selection is based on fast custom algorithms processing partial event data from the ROS corresponding to the ROIs identified by L1. The L2 triggers reduce the rate to 3 kHz, with an average processing time of 40 ms/event.

The last stage of the selection is performed by the EF. The Event Builder puts together all event fragments from the ROS from events accepted by L2.

This provides the full event information to the EF. The EF is largely based on offline algorithms and is designed to reduce the rate to ∼200 Hz, with an average processing time of 4 s/event. Data for the events that are selected by the trigger system are written into so-called inclusive data streams. These streams are based on trigger type, and there are four main physics streams; Egamma (electrons and photons), Muons, JetTauEtmiss and MinBias.

4.3.6 Physics Objects in ATLAS

The previous sections presented a short introduction to the sub-detectors of ATLAS. They are designed and ordered to maximize reconstruction efficiency. Any electrically charged particle that is created in a collision should ideally leave signals in the detector. The goal of a particle detector is not to measure electric

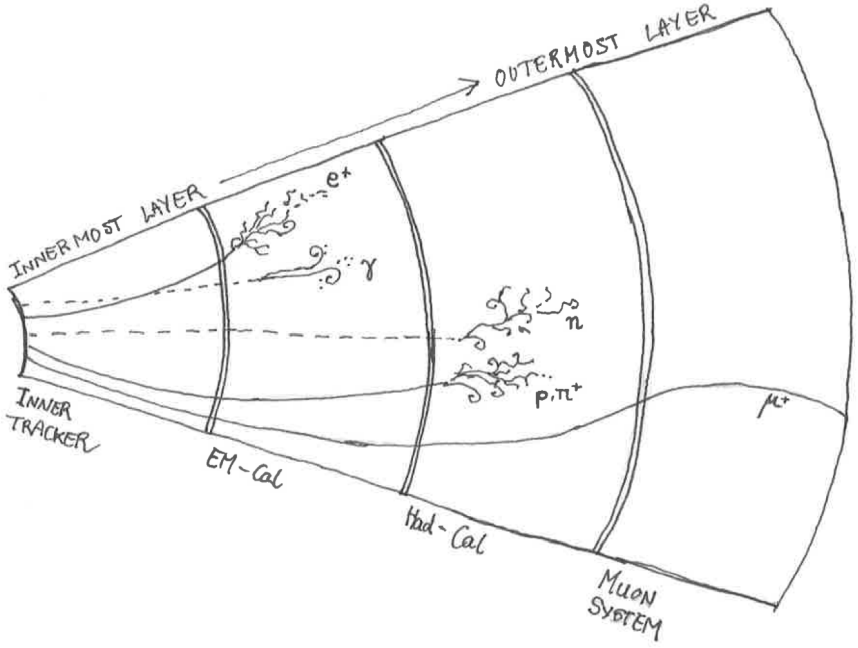

Figure 4.5: Illustration of how different particles are identified in the ATLAS detector. Only neutral and positively charged particles are shown, negatively charged particles will curve in the opposite direction in the magnetic fields.

signals and verify that something went through the machine, even though this is partly how the detector works. In order to connect the measurements to physics, the signals have to be interpreted in terms of physical objects, and the most obvious choice of interpretation is in terms of particles. In Figure 4.5 it is indicated

where in the detector various particles leave tracks, and where they deposit energy. ATLAS is designed to identify electrons, photons, muons and jets (hadrons). The following sections will give a brief overview of the reconstruction and identification of these different physics objects in the detector. Reconstruction and identification of tau leptons will be handled in detail in Section 5.1 and Section 5.2 respectively.

Electrons

An electron will leave a track in the ID and deposits its energy in the EM calorimeter. As a hadronic jet can leave similar traces, measurements in the hadronic calorimeter also have to be taken into consideration. Electrons are, in the central region where $|\eta|< 2.47$, reconstructed from their energy deposits in the EM calorimeter. Clusters of total transverse energy larger than 2.5 GeV are searched for by a sliding-window algorithm with window size 3×5 in units of 0.025×0.025 in (η, ϕ) space, further explained in Ref. [70]. These are then associated with reconstructed tracks from charged particles in the ID. Central electrons with $p_T>$ 20 GeV are chosen for the analysis following in Chapter 7.

The electron reconstuction in the forward region, $2.5<|\eta|<4.9$, relies on a topological clustering algorithm [71]. Cells with deposited energy significatly above noise level are grouped in three dimensions in an iterative procedure. In this region there are no tracking detectors, and so there is no distinction between electrons and photons, that also deposit their energy in the EM end-cap calorimeters. Here an electron candidate is reconstructed if it has a transverse energy of $E_T>$ 5 GeV and if the energy deposit in the hadronic calorimeter is small.

After the reconstruction, identification follows. The identification of electrons in ATLAS relies on cuts on different variables that provide good seperation between electrons and jets. These include the shower width in the EM calorimeter, quality of tracks reconstructed and cluster energy over track momentum (E/p). There are three selections for identified electrons; 'loose', 'medium' and 'tight', with increasing background rejection power.

Photons

The electromagentic interaction of photons with the EM calorimeter leads to photons and electrons appearing very similar in the calorimeters, and so reconstruction of photons follows in its main aspects that of electrons, and photons are reconstructed as isolated objects with most of their energy deposited in the EM calorimeter [72]. At photon energies above 1 GeV the interaction of photons with the ID is dominated by $\gamma \rightarrow e^+e^-$, electron-positron-pair production, in the presence of material. This is otherwise known as conversion [73]. The converted

photons can be identified by the presence of two tracks with opposite curvature that originate from a common vertex in the tracking volume.

Muons

In Figure 4.5 it is easy to see that the muons leave a very distinct signal in ATLAS. As mentioned in Section 4.3.4, muons are minimal ionizing particles and penetrate the calorimeters. Independent track reconstruction in the ID and muon system are combined for the identification of muons. In Ref. [74] the reconstructed muons are divided into three classes; stand-alone, combined and segment-tagged muons. A stand-alone muon has a reconstructed track only in the muon system, which is extrapolated. A combined muon is reconstructed from successfully combining a stand-alone track from the muon stystem with a track from the ID. These muon candidates constitute the sample with the highest purity. A segment-tagged muon is reconstructed from a track in the ID and is identified as a muon if the track matches a straight segmet in the muon system. For this analysis combined and segment-tagged muons are selected if $p_T > 10$ GeV and $|\eta| < 2.4$.

Jets

A jet is a colour neutral cone of hadrons that spring from a common origin, such as a hadronizing gluon or quark. The charged fragments of the jet will leave tracks in the ID, and all jets will deposit their energy in the calorimeters. In ATLAS many different algorithms can be used for jet reconstructions, as described in detail in Ref. [75], but for this thesis jets are reconstructed using the anti-k_t clustering algorithm, with a distance parameter $R \leq 0.4$ in η-ϕ space. The distance parameter is also called the radius parameter. The algorithm uses inputs from clusters of calorimeter cells above noise level. The jets are also corrected for pile-up[10] and other effects, and jets within $|\eta| < 2.8$ are required to have $p_T > 20$ GeV.

Missing Transverse Energy

Models that attempt to explain dark matter, other proposals for new physics and some interactions in SM physics[11], predict occurances of weakly interacting particles. In other words, sometimes we expect particles to escape the detector, and not because the detector is inefficient. The energy of these particles will not

[10] Every time proton bunches pass each other at a collision point in the LHC, multiple protons can interact. It is rare that more than one of these produce interesting particles, but they all produce particles. This is what is referred to as in-time pile-up. Out-of-time pile-up occurs when arge deposited in a previous collision has not yet been transported away by the front-end electronics. This could lead to the current signal stacking on top of the old one.

[11] As an example, a neutrino will move through ATLAS undetected.

be measured. This is where the power of transverse components very much reveals itself. The transverse energy, E_T, of the particles that escaped can be calculated on the assumption that initially the interacting particles have no p_T. The total E_T should therefore amount to $\sim$0. The total E_T is built up from the vectorial sum of all reconstructed objects, starting with calibrated jets, correcting with electrons, photons and muons. In this analysis τ leptons are not treated separately, but included with the jets.

4.3.7 Upgrade

The first run is over at the LHC. In this first long shut-down (LS1) the plans for detector enhancement are being carried out. As explained in Section 4.2 the main goal of LS1 is to get the LHC and its detectors working at design energies. Firstly at $\sqrt{s} = 13$ TeV, moving on to 14 TeV. There are many challenges considering both accelerator and detectors. I will only go into the main upgrades already implemented, and the ones ATLAS will undergo in the near future.

The pixel detector of ATLAS recently got a fourth innermost layer. The Insertable B-Layer (IBL was successfully inserted on 7 May 2014. The IBL is a 70 cm long cylinder of about 3 cm in radius that will provide ATLAS with about 12 million more detection channels. The IBL uses well established planar sensor technology in addition to novel 3D sensors. The cooling system for the silicon detectors is undergoing improvements, both in general and for the inclusion of the IBL. The installation of a final layer of chambers in the muon spectrometer was completed during the first three months of LS1, and a few TGCs will be exchanged. New low-voltage power supplies are being installed for the calorimeters, improvements are planned for parts of the electronic infrastructure and the L1 central trigger will be upgraded [76].

Chapter 5

The Tau Lepton

The most significant difference between the analysis optimised in Chapter 7 and the analysis searching for jets and large missing transverse energy [2] is that, in the first one, a tau lepton is required to be present. For the one tau analysis to be efficient, and for calculations of limits that can compare, or even compete, with the tau-less analysis it is key to have a good understanding of the kinematic properties of the tau and of the reconstruction and identification of this particle.

The tau lepton is the heaviest known lepton, with a mass of 1776.82 ± 0.16 MeV [3]. This high mass causes the tau lepton to be the only lepton for which decay modes involving hadrons is allowed. The most important decay modes are summarised in Table 5.1. The proper decay length of 87 μm, or $(290.6 \pm 1.0) \times 10^{-15}$ s, also leads to the tau leptons decaying before they reach the detector so that they can only be identified through reconstruction of their decay products. The tau decays can be divided in *leptonic* and *hadronic* modes. 35% of all taus decay in the leptonic mode, τ_{lep}, as shown in Table 5.1. When a tau lepton decays leptonically it decays into two neutrinos and either an electron $\tau \to e\nu_e\nu_\tau$ or a muon $\tau \to \mu\nu_\mu\nu_\tau$. These decay products cannot be distinguished from prompt electrons or muons, and are not considered for tau identification.

5.1 Reconstruction

A hadronically decaying tau lepton has a detector signature which is very similar to the signature associated with jets and other leptons. Conservation of tau number, L_τ, requires the τ to have a ν_τ amongst its decay products. The neutrinos escape detection, and so exact full reconstruction of the hadronically decaying τ_{had} is impossible. The reconstructed object is instead $\tau_{\text{had-vis}}$. The decay mode definitions are summarised in Table 5.2. To separate taus from objects with similar detector signatures it is crucial to combine information from many sub-detectors

Decay mode	Fraction (Γ_i/Γ)
$\tau \to e\nu_e\nu_\tau$	$(17.83 \pm 0.04)\,\%$
$\tau \to \mu\nu_\mu\nu_\tau$	$(17.41 \pm 0.04)\,\%$
$\tau \to h^\pm(nh^0)\nu_\tau$	$(48.11 \pm 0.12)\,\%$
$\tau \to \pi^\pm\nu_\tau$	$(10.83 \pm 0.06)\,\%$
$\tau \to \pi^\pm\pi^0\nu_\tau$	$(25.5 \pm 0.09)\,\%$
$\tau \to \pi^\pm\pi^0\pi^0\nu_\tau$	$(9.52 \pm 0.11)\,\%$
$\tau \to \pi^\pm\pi^0\pi^0\pi^0\nu_\tau$	$(1.19 \pm 0.07)\,\%$
$\tau \to h^\pm h^\pm h^\pm(nh^0)\nu_\tau$	$(15.20 \pm 0.08)\,\%$
$\tau \to \pi^\pm\pi^\pm\pi^\pm\nu_\tau$	$(9.31 \pm 0.06)\,\%$
$\tau \to \pi^\pm\pi^\pm\pi^\pm\pi^0\nu_\tau$	$(4.62 \pm 0.06)\,\%$
$\tau \to \pi^\pm\pi^\pm\pi^\pm\pi^0\pi^0\nu_\tau$	$(0.51 \pm 0.03)\,\%$
$\tau \to \pi^\pm\pi^\pm\pi^\pm\pi^0\pi^0\pi^0\nu_\tau$	$(0.21 \pm 0.04)\,\%$
$\tau \to h^\pm h^\pm h^\pm h^\pm h^\pm(h^0)\nu_\tau$	$(0.102 \pm 0.004)\,\%$
Other	$\simeq 4.3\%$

Table 5.1: The main decay modes for the τ lepton. $h^\pm$ and h^0 denote charged and neutral hadrons respectively, and $n = 0, 1, 2\ldots$ is the number of h^0. Not all possible decays are included in this table. Numbers are taken from Ref. [3].

for reconstruction of hadronically decaying taus. The reconstruction algorithm, TauRec [77], for $\tau_{\text{had-vis}}$ thus combines tracking and calorimeter information.

Variable	Explanation
τ_{lep}	Tau leptonic decay mode
τ_{had}	Tau hadronic decay mode
$\tau_{\text{had-vis}}$	Visible part of the hadronic tau decay

Table 5.2: Tau decay mode definitions.

The $\tau_{\text{had-vis}}$ reconstruction algorithm is seeded from jet-objects that are reconstructed using the anti-k_T algorithm. The jet is required to have $p_T > 10$ GeV, R = 0.4, and an η and p_T-dependent energy calibration to the hadronic tau energy scale is applied. TauRec looks for jets likely to come from tau decays, whilst trying to reject any other object of non-tau origin. Due to the hadronic jet structure, the most problematic objects that fake taus are QCD jets. They have to be efficiently suppressed due to their large abundance at the LHC. The tau reconstruction, however, provides little rejection against QCD jet background. Rejection comes from a separate identification step based on simple cuts, boosted decision trees (BDT), or projective likelihood methods. As the identification in the following analysis is based on BDT, this method is investigated in Section 5.2.

5.2 Identification

The charge of the tau decay products must add up to the charge of the decaying particle as charge is a conserved quantity. For this reason there will always be an odd number of charged particles in the decay products of a tau. A τ will in most cases leave either one or three tracks in the detector: see the branching fractions in Table 5.1, 1-prong or 3-prong τ respectively. This is a quite effective discriminant against QCD jets since these are not restricted to a certain number of charged particles. For the following analysis, tau-lepton candidates are required to be 1- or 3-prong with a charge sum of ± 1, $p_T > 20$ GeV and $|\eta| < 2.5$. Some aspects of the identification are split into 1-prong and multi-prong candidates. Taus can also be separated from other jets by their specific topology in the calorimeter and by the way energy is shared between the constituents.

5.2.1 Identification variables

Discriminating variables based on observables sensitive to the shape (transverse or longitudinal) of energy deposits from tau candidates in the calorimeter are combined with tracking information into a BDT discriminator. Some of the discriminating variables that were used for training of the BDT in this analysis, see Section 5.2.2, are listed below:

$$R_{trk} = \frac{\sum\limits_{i \in tracks}^{\Delta R_i < 0.4} p_T^i \Delta R_i}{\sum\limits_{j \in tracks}^{\Delta R_j < 0.4} E_T^j}$$

track radius is the transverse momentum weighted track width. i and j run over all tracks associated with the tau candidate within the core where ΔR $<$ 0.4, and $\Delta R = \sqrt{(\Delta\eta)^2 + (\Delta\phi)^2}$ The solid angular distance of each track is measured with respect to the tau candidate axis and p_T^i is the track transverse momentum. For candidates with one track this simplifies to the ΔR of the track to the candidate axis.

$$f_{trk} = \frac{p_T^{leadtrk.}}{p_T^{tau}}$$

The leading track momentum fraction is the ratio of the p_T of the leading core track to the total p_T of the tau candidate.

$$f_{core} = \frac{\sum\limits_{i \in cells}^{\Delta R_i < 0.1} E_T^i}{\sum\limits_{j \in cells}^{\Delta R_j < 0.4} E_T^j}$$

The core energy fraction is the ratio of E_T within $\Delta R <$ 0.1 and $\Delta R <$ 0.4 of the tau candidate. The indices i and j run over all cells associated with the tau in the respective ΔR cones.

$$R_{cal} = \frac{\sum\limits_{i \in cells}^{\Delta R_i < 0.4} E_T^i \Delta R_i}{\sum\limits_{j \in cells}^{\Delta R_j < 0.4} E_T^j}$$

The calorimeter radius is the shower width weighted by the transverse energy of each calorimeter part (Had. and EM). The indices i and j run over all cells associated with the tau in the respective ΔR cones.

$$m_{eff}^{clust.} = \sqrt{\left(\sum_i E_i\right)^2 - \left(\sum_i \overrightarrow{p}_i\right)^2}$$

The cluster mass is the invariant mass computed from the constituent clusters of the jet.

$$m_{eff}^{trk} = \sqrt{\left(\sum_i E_i\right)^2 - \left(\sum_i \overrightarrow{p}_i\right)^2}$$

The track mass is the invariant mass computed from the track system of the tau candidate. The index i runs over all tracks associated with the tau candidate.

$S_T^{flight} = \frac{L_T^{flight}}{\delta L_T^{flight}}$ **The transverse flight path significance** is the decay length significance of the secondary vertex in the transverse plane. L_T^{flight} denotes the decay length, δL_T^{flight} the corresponding estimated uncertainty.

$S_{lead.trk} = \frac{d_0}{\delta d_0}$ **The leading track impact parameter significance** of the tau candidate. d_0 is the distance of closest approach of the track to the reconstructed primary vertex in the transverse plane, and δd_0 is the corresponding estimated uncertainty.

$f_3^{lead.clust.} = \frac{\sum_{i \in clust.}^{3} E_i}{\sum_{i \in clust.}^{N} E_i}$ **The first three leading clusters energy ratio** is the ratio of energy in the three leading clusters (highest energy) divided by the energy of all N clusters associated with the tau candidate.

$\Delta R_{max} = max\{\Delta R_i^{trk}\}$ **The maximal ΔR** is the maximal solid distance of tracks in η-ϕ-space where i runs over all tracks.

Definitions and descriptions of all variables, including the ones above, can be found in Appendix A of [77].

5.2.2 BDT ID

Boosted Decision Tree, BDT [78], is a multivariate method often used in analysis in HEP. The goal is to separate signal events from background events. A MC sample is divided into two parts. The first one is the training sample used to train the decision tree. For each event there are a number of particle identification (PID) variables, some of which are described above. Initially events are ordered by value for each PID variable. For the first variable, the training sample is split in two based on the value of this variable. A splitting value that provides the best separation between one side being mostly signal and the other mostly background is chosen. This splitting process is repeated for each PID variable to find the

variable that gives the best separation. The "node" of events is separated into two "branches". For each new node this procedure is repeated until termination. This could happen when a set number of branching has occurred, or until each node is either pure signal or pure background, or else the number of events in a node is too small. The final nodes in the tree are termed its "leaves".

The second part, the test sample, is then used to test the classification and training.

The boosting of event trees starts with building one unweighted tree. Training events misclassified in the final leaf will be given an increased weight: it is boosted. The new weight follows the event into the building of a new tree. Typically, one may build 1000 or 2000 trees this way. An event is followed through each of the trees. If it lands in a signal leaf it gets a score 1 and if it lands in a background leaf the score is -1. The renormalized sum of all scores, possibly weighted, is the final score of the event. A high score means the event is signal-like whereas a low score translates to a background-like event. By choosing a particular value of the score on which to cut, one can select a desired fraction of the signal or a desired ratio of signal to background.

The BDT is trained separately for one- and multi-prong candidates. It is also trained for different pile-up conditions. The training is performed in the Tool for Multivariate Data Analysis with ROOT (TMVA) [79]. The BDT score cut is limited to three benchmarks of strictness: loose, medium and tight. These are defined by a signal efficiency for 1-prong taus of 0.65, 0.55 and 0.35 respectively. In the 1τ analysis in Ref. [1] the medium tau definition is used.

The four plots in Figure 5.1 show the jetBDT output, the output of BDT trained for jet rejection, for one of the benchmark points in the following analysis, the mSUGRA signal point with $m_0 = 600$ GeV and $m_{1/2} = 850$ GeV. Figure 5.1a and Figure 5.1b show jetBDT output for true and fake Medium taus, respectively. The cut on the BDT score seems to be $\sim$0.52. The plot for true taus has a peak around 0.75. For the plot of fake Medium taus it is harder to point out any peak, but there are less events with a score above 0.7 then there are events with a higher score. Figure 5.1c and Figure 5.1d show jetBDT output for true and fake Loose taus, respectively. Here, the cut on the BDT score is $\sim$0.50, and there is an increased number of events with lower a BDT score.

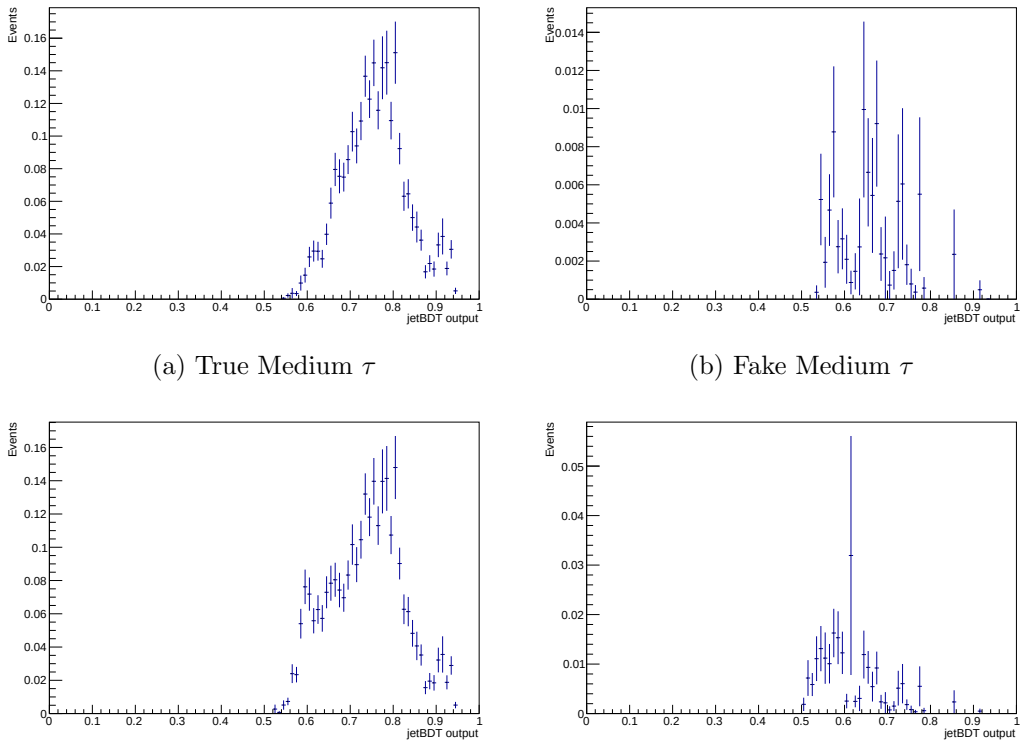

(a) True Medium τ

(b) Fake Medium τ

(c) True Loose τ

(d) Fake Loose τ

Figure 5.1: jetBDT output for mSUGRA signal point $m_0 = 600$ GeV, $m_{1/2} = 850$ GeV in the loose SR.

Chapter 6

Simulation and Analysis tools

An experimental particle physicist needs an experiment to test the scientific hypotheses proposed by their theoretical counterparts. To analyse the results from this experiment, the physicist is required to learn how to use certain tools. For analysis of data collected by the particle detector ATLAS, for which subdetectors and object reconstruction was presented in Section 4.3, Monte Carlo (MC) simulated data and a framework within which the analysis can be conducted are the most important tools. All particle physics research depends on accurate simulations of both physics events and detector response, in order to understand the complicated physics involved in hadron collisions. The analysis of real data can be compared with analysis of simulated data to gain an understanding of the physics process behind the results.

This chapter will present simulation in ATLAS, both event generation and detector simulation. The basic set-up will be described, with some examples and a brief presentation of event generation in SUSY. Two methods of detector simulation will then be introduced, along with a comparison of the two for part of the signal grid of the mSUGRA model investigated in this thesis. This is followed by a short introduction to the programming languages C++ and Python, and the framework used for the analysis presented in Chapter 7: ROOT.

6.1 Simulation

Due to the tiny cross-sections of the signatures of potential new physics, like SUSY, with respect to background processes, and the need to study systematic effects with increasing precision, a large number of events needs to be generated for MC studies. Samples of MC simulated events are used for evaluating the expected SM backgrounds and for estimating the signal efficiencies for the different SUSY models. The first step of the simulation is the generation of physics events

in proton-proton collisions. The considered physics is randomly realized according to its probability of occurrence. After the event generation, the four-momenta and quantum numbers of all generated particles are known, and their interaction with the detector can be simulated. The framework used in the ATLAS experiment to control simulation and analysis jobs is called Athena. It controls and interfaces different components in a simulation chain.

6.1.1 Event Generators

Accurate predictions, which in addition cover the full range of physics processes, is necessary. For physicists to have confidence in possible excesses, evidences and eventually discoveries, an intense process of description or prediction of data via MC is needed. Events in high-energy collisions have complex structures that are not predictable from first principles. At the most basic level a Monte Carlo event generator is a program which produces particle physics events with the same probability as they occur in nature, a virtual collider. In practice it performs a large number of, sometimes very difficult, integrals and then unweights to give the four momenta of the particles that interact with the detector (simulation). This includes the full event kinematics, the decay of all particles that are unstable on detector scale and the hadronisation of all strongly interacting particles in the conditions of overlaying proton-proton collisions [80].

The hard scattering and convolution with parton distributions form the central calculation of event generator programs. A collision between two partons, one from each proton, gives the hard process of interest. The probability of a given parton (quark or gluon) to take part in this collision is given by parton density functions (PDFs). The hard sub-process is usually a $2 \rightarrow 2$ scattering process, two partons go into the collision, two go out. The event generator must be able to compute the probability for different outgoing particles. Matrix elements for arbitrary processes are calculated and integrated over phase space. This describes the initial scattering, the process which potentially contains the new physics we are interested in. It is well known, though, that a particle collision is more complex than this. Parton shower generators simulate how the outgoing partons split into parton showers. The resulting partons hadronise and form colour singlet hadrons, and unstable particles will decay further. Initial- and finial- state radiation have to be taken into account, and the underlying structures of the event have to be generated. The partons considered to take part in the interesting hard process only take a fraction of the momentum of the protons, and so much of the energy remains in the beam remnants, which continue to travel essentially in the original directions. There is also a possibility of multiple parton interactions, both from other partons in the protons and collisions between other protons in the same bunch crossing (pile-up).

There are many different event generators, and many of them have been used to generate the MC samples used in this thesis. Some are general-purpose event generators that provide fully exclusive modelling of high-energy collision, others are more specialised.

HERWIG is a general-purpose MC event generator. The parton shower approach is used to simulate initial- and final- state QCD radiation [81].

PYTHIA is a general-purpose MC event generator that contains a library of hard processes and models for initial- and final-state parton showers, multiple parton-parton interactions, beam remnants, string fragmentation and particle decays [82].

SHERPA is a general-purpose MC event generator with special emphasis on matrix-element/parton-shower merging [83].

POWHEG is a method to generate MC events that is accurate at the next-to-leading order in QCD which can be interfaced to various different parton-shower Monte Carlo programs, including Jimmy and Pythia [84].

Jimmy is a model for multiple interaction underlying events [85].

MC@NLO calculates matrix elements up to second order. It uses HERWIG for parton showers [86].

ALPGEN is a matrix element generator for hard multiparton processes, that needs to get parton showers and fragmentations from a parton shower event generator [87].

DarkSUSY computes masses and mixings of supersymmetric particles, as well as a large variety of astrophysical signals from neutralino dark matter [88].

ISAJET was the first event generator program developed to give a realistic portrayal of SUSY scattering events [89].

6.1.2 Detector simulation

A huge fraction of dedicated computing time in experimental particle physics can be accounted to the simulation of particle interactions with the active and passive detector material and the determination of the detector response. The response of the detector is traditionally simulated as accurate as possible, by modelling any small structures which could affect traversing particles. These structures could originate from the interaction point in the centre of the detector, from subsequent reactions and decays, or from cosmic radiation. This approach is very

time-consuming and therefore not always feasible. In order to study rare processes, systematics and background effects, some analyses require a large number of collision events to be simulated.

GEANT4

The standard simulation strategy in ATLAS is based on the GEANT4 particle simulation toolkit [90] and uses a very detailed detector description. The detector geometry is constructed in GEANT4 format, and the toolkit provides detailed models for physics processes and the infrastructure for particle transportation through the geometry. The interaction of particles with the detector material releases additional particles in the calorimeter or free charge carriers in the semiconductor detectors, which are added to the simulation. Following this the particles will either deposit all their energy in the detector or escape the detector geometry. The software propagates the produced primary and secondary particles to the readouts. The induced electric signals are mimicked by the amount of simulated charge carriers, and hence the expected physical readouts from the original interaction are estimated [63]. This simulation of the detector response is called the digitisation. The hits from the tracking devices and the energy deposits in the calorimeters are converted into detector digits, corresponding to the output from the ATLAS detector. The final step in the simulation chain is the reconstruction of the original event. The reconstruction algorithms used are the ones mentioned in Section 4.3.6.

Because of the complicated detector geometry and detailed physics description used by the full Geant4 simulation, it is impossible for some physics studies to achieve the required simulated statistics without faster simulation strategies.

AtlFast-II

One of the faster simulation strategies is AtlFast-II (AFII) [91]. This uses FastCaloSim for the simulation of the calorimeter. The energy of single particle showers is deposited directly using parameterisations of their longitudinal and lateral energy profile. The reconstructed AFII output includes the energies in the calorimeter cells. Because the standard reconstruction is run, it is possible to work with a combination of events obtained from Geant4 and Atlfast-II without modifying the analysis code. This is done for some of the simulated backgrounds in the analysis in Chapter 7. The parametrisation in FastCaloSim can be tuned to data for increased accuracy.

Comparison of AFII with full Geant 4 simulation

The 1τ analysis [1] uses a combination of samples simulated with the full Geant4 simulation (fullsim) and samples simulated with the AFII fast simulation tool for $t\bar{t}$, since for Powheg there is a large extension with AFII available. The Sherpa simulations of W + jets and Z + jets also have AFII extensions, see Section 7.2.2. Taus are known to be less reliably described in AFII than in fullsim. The results of performance studies have been found to depend on the sample and the studied kinematics. For this reason an individual evaluation is required for each analysis who wishes to use AFII samples with taus. Extensive studies were done on the performance of the AFII $t\bar{t}$ sample. The studies showed that for the phase space relevant to the analysis, the performance of AFII was comparable to that of fullsim. For these background samples the uncertainties introduced by using AFII is seen to be covered by generator systematic uncertainties.

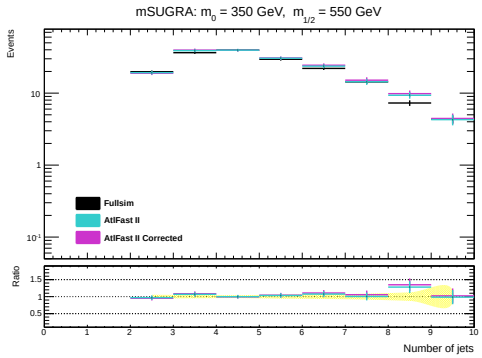

(a) $m_0 = 350$ GeV, $m_{1/2} = 550$ GeV, after plateau cuts

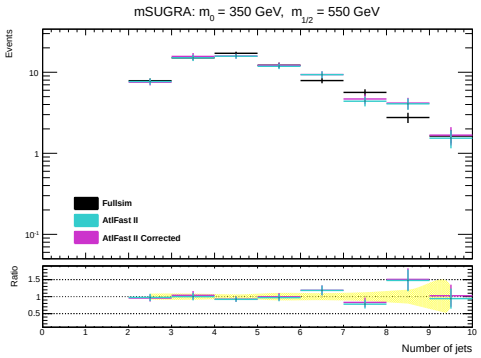

(b) $m_0 = 350$ GeV, $m_{1/2} = 550$ GeV, after anti-QCD cuts

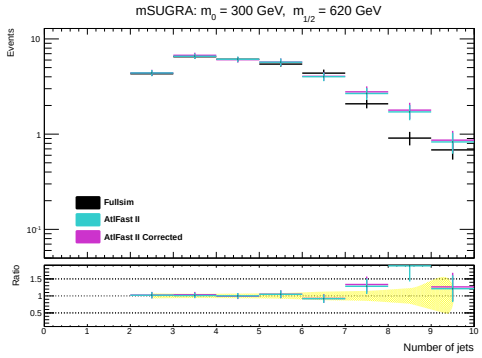

(c) $m_0 = 300$ GeV, $m_{1/2} = 620$ GeV, after plateau cuts

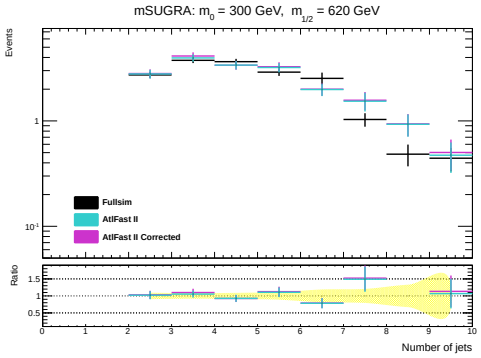

(d) $m_0 = 300$ GeV, $m_{1/2} = 620$ GeV, after anti-QCD cuts

Figure 6.1: Comparison of number of jets with full detector simulation, AtlFastII and AtlFastII with corrections

For the Powheg simulation of $t\bar{t}$, the AFII sample yields five times the statistics of the fullsim sample. The idea of being able to produce a larger grid of signal samples in a shorter amount of time is appealing. The analysis could benefit from both finer spacing between the grid points and extending the grid to larger mass values. This motivated a study of the performance of AFII fast simulation of the eight signal points in Table 6.1. The points were centrally produced in both AFII and fullsim.

m_0 [GeV]	230	250	280	300	320	320	350	350
$m_{1/2}$ [GeV]	420	460	550	620	640	660	550	680

Table 6.1: mSUGRA signal points for comparison of the performance of AFII and full detector simulation.

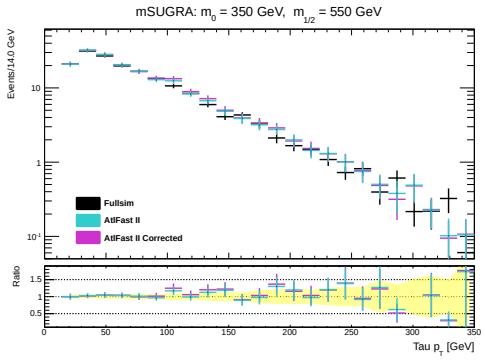

(a) $m_0 = 350$ GeV, $m_{1/2} = 550$ GeV, after plateau cuts

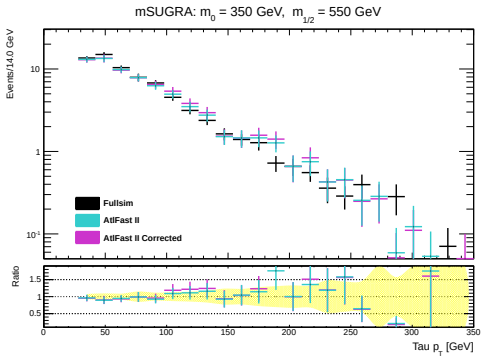

(b) $m_0 = 350$ GeV, $m_{1/2} = 550$ GeV, after anti-QCD cuts

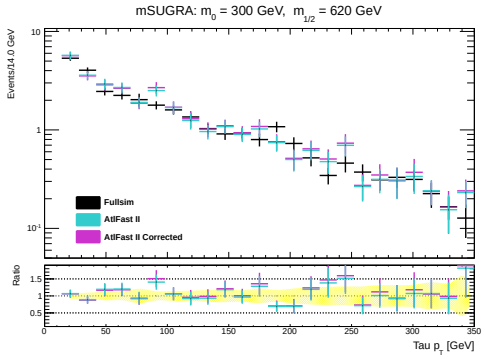

(c) $m_0 = 300$ GeV, $m_{1/2} = 620$ GeV, after plateau cuts

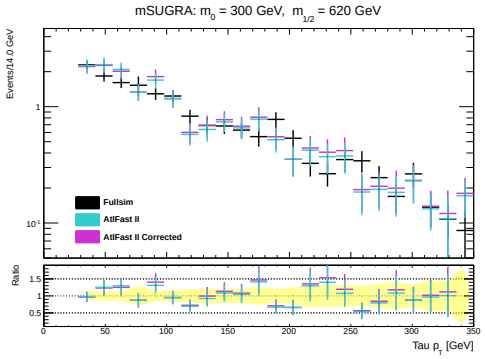

(d) $m_0 = 300$ GeV, $m_{1/2} = 620$ GeV, after anti-QCD cuts

Figure 6.2: Comparison of p_T of the first tau with full detector simulation, AtlFastII and AtlFastII with corrections

The Tau working group provides two corrections to account for mismodelling of taus in AFII. One is a correction for the efficiency in terms of a kinematic dependent scaling factor. The second correction is for a p_T mismodelling in terms of a p_T shift. Both corrections are intended to be applied at the same time. A comparison of fullsim, AFII and AFII with these two corrections applied (AFII corrected) is presented in Figure 6.1, Figure 6.2 and Figure 6.3. The figures show plots of number of jets, p_T of the first tau lepton and jetBDT output (see Section 5.2.2) respectively.

All distributions are shown for two signal points: $m_0 = 300$ GeV and $m_{1/2} = 550$ GeV, $m_0 = 350$ GeV and $m_{1/2} = 620$ GeV. The plots on the left hand side show distributions after plateau cuts, and the plots on the right hand side show distributions after the first anti-QCD cut. Further descriptions of these cuts are provided in Section 7.3.

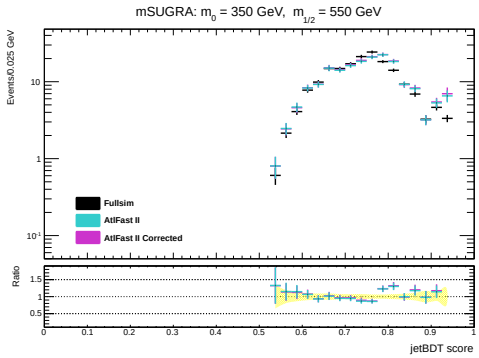

(a) $m_0 = 350$ GeV, $m_{1/2} = 550$ GeV, after plateau cuts

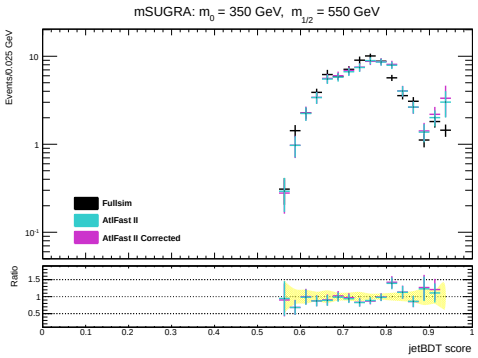

(b) $m_0 = 350$ GeV, $m_{1/2} = 550$ GeV, after anti-QCD cuts

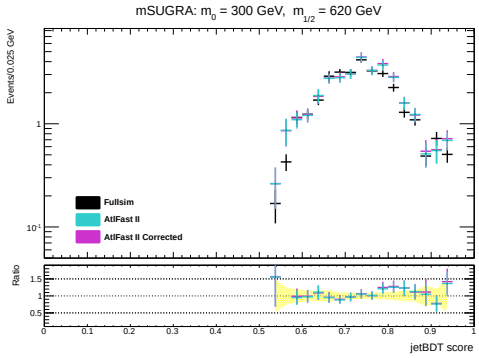

(c) $m_0 = 300$ GeV, $m_{1/2} = 620$ GeV, after plateau cuts

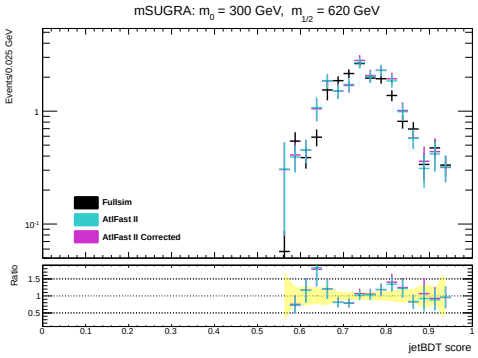

(d) $m_0 = 300$ GeV, $m_{1/2} = 620$ GeV, after anti-QCD cuts

Figure 6.3: Comparison of jetBDT with full detector simulation, AtlFastII and AtlFastII with corrections

All comparisons show good agreement between fastsim and fullsim on the level of statistical uncertainties. The corrections have no significant effect on the shape agreement. The agreement actually seems to be better between fullsim and AFII when the corrections are not applied, even though the two follow each other very closely both for the different variables, for all points and through the cutflow.

In the end, the one-tau analysis did not prioritise switching to fast simulation of the signal grid. In the future, signal grids could be made with AFII. As the next generation of analyses will work with higher energies and luminosities, and will therefore study different kinematics, new performance studies would have to be done for these in order to use AFII instead of fullsim for signal.

6.2 Analysis

Computers can help us perform useful tasks, solve high-level problems and so much more. However, computers have to be told in no uncertain terms what they are supposed to do, and their native languages are quite unlike any human language. Thus, there is a language barrier between a person who wishes a computer to do something, and the computer that typically requires instructions in its native language, machine code, to do anything. The computers rely on programs which we create, which are sets of instructions that the computer can understand and follow. A computer program is a sequence of instructions that dictates the flow of electrical impulses within a computer system. One program may allow a computer to assume the role of a financial calculator, while another transforms the machine into a worthy chess opponent. There exists a wide range of programming languages. The analysis in Chapter 7 makes use of two very different ones: C++ and Python.

6.2.1 C++

C++ is an open ISO-standardized [92] language. It is a compiled language, meaning the language is translated into the target machine's native language by a program called a compiler. This can result in fast code, even though compilation can take some time, and one has to compile every time something part of the code has been changed. C++ is a so-called strongly typed unsafe language. There are restrictions on how different types of variables can be converted to each other without any converting statements. The programmer is expected to know what he or she is doing, otherwise the code will not compile. C++ is a very flexible language that offers many paradigm choices. It offers support for procedural, generic, and object-oriented programming paradigms, among others. Procedures, or functions, contain a series of computational steps to be carried

out. Procedural programming is a list or set of instructions telling a computer what to do step by step and how to perform from the first code to a second code. Generic programming means that the programmer is not writing source code that is compiled as-is, but "templates" of source codes that the compiler in the process of compilation transforms into source codes. The C++ Standard Library includes the Standard Template Library that provides a framework of templates for common data structures and algorithms. Object oriented programming gives the ability to easily modularise the analysis code, thus making many parts of the code reusable. In addition, an object oriented approach has a number of other advantages such as data encapsulation and data protection, making the code more robust [93]. C++ was chosen as the basis of ROOT, presented in Section 6.2.3.

6.2.2 Python

Python is developed under an OSI-approved open source license, making it freely usable and distributable, even for commercial use. It is an interpreted object-oriented programming language. Data types are strongly and dynamically typed. Interpreted languages are read by a program called an interpreter and are executed by that program. While they are as portable as their interpreter and have no long compile times, interpreted languages are usually a lot slower than equivalent compiled programs. Mixing incompatible types in Python (e.g. attempting to add a string and a number) causes an exception to be raised, so errors are caught sooner. Python's automatic memory management frees the programmer from having to manually allocate and free memory in the code [94]. For this thesis Python, in combination with ROOT (see Section 6.2.3), has been used mainly for making plots. The syntax is more elegant and the fact that there is no need for compiling makes it a lot faster and more suitable for making histograms than ROOT with C++.

6.2.3 ROOT

The ROOT project [95, 96] was started by Rene Brun and Fons Rademarker in 1995. It is an object-oriented framework aimed at solving the data analysis challenges of high-energy physics. In a framework, the basic features, such as I/O and graphics, are provided. ROOT, being a HEP analysis framework, provides a large selection of HEP specific utilities such as histogram methods in an arbitrary number of dimensions, curve fitting, function evaluation and graphics classes. Working within a framework requires you to learn the framework interfaces and it can constrain you, but if you are interested in doing physics a good HEP framework can make your life a lot easier. The ROOT system provides the functionality needed to analyse large amounts of data in an efficient way. The data is defined as a set

of objects and specialised storage methods (trees with branches) are used to get direct access to the separate attributes of the selected objects, without having to touch the bulk of the data. The built-in CINT C++ interpreter allows the command language, the scripting, or macro, language and the programming language to all be C++. The interpreter allows for fast prototyping of the macros since it removes the time consuming compile/link cycle. ROOT is an open system that can be dynamically extended by linking external libraries. This makes ROOT a premier platform on which to build data acquisition, simulation and data analysis systems. The analysis in this thesis was done in ROOT with version 00-03-14 of the SUSYTools package[1], benefiting from the SusyOneTauCore package of the one-tau analysis.

PyROOT

PyROOT [97] is a Python extension model. It provides the bindings for the ROOT class library in a generic way using the CINT dictionary, and allows the user to interact with any ROOT class from the Python interpreter. There is no need to generate any Python wrapper code to include new ROOT classes. PyROOT also offers the possibility to execute and evaluate Python commands or start Python shells from the ROOT/CINT prompt.

[1]The SUSYTools package is a collection of various tools provided by combined performance groups for object reconstruction and treatment of systematic uncertainties.

Chapter 7

Reaching towards higher masses of supersymmetric particles

7.1 Introduction

In many SUSY models the tau lepton can provide an important signature. As explained in Section 3.1.1 SUSY realised at the electroweak energy scale would expect the third generation of sfermions to be the lightest sleptons. With R-parity conserved, this means the production rate into final states with taus is expected to be larger than into final states with electrons or muons. Compared to an analysis focussing on jets and missing transverse energy, E_T^{miss}, requesting a tau should provide a good measure of rejecting backgrounds, like multijet background, while keeping other kinematic cuts relaxed.

This is however not the case for the supersymmetric model minimal Super Gravity (mSUGRA), in the m_0 $m_{1/2}$ mass plane. The 1τ analysis "Search for supersymmetry in 8 TeV p–p collisions with τ-leptons, jets and missing transverse energy in the final state" [1] is less sensitive for low m_0 and high $m_{1/2}$ than the similar analysis "Search for squarks and gluinos with the ATLAS detector in final states with jets and missing transverse momentum and 20.3 fb^{-1} of $\sqrt{s} = 8$ TeV proton-proton collision data" [2]. The two analyses are looking at the same simulated mSUGRA signal samples, but the latter analysis is able to exclude a larger part of the grid, as shown in Figure 7.1.

7.1.1 Structure of the analysis

This chapter will start off with a presentation of the data and simulated MC samples used in the analysis. The first part will trace the steps of the existing 1τ analysis, which is the starting point of the following optimisation. The 1τ analysis

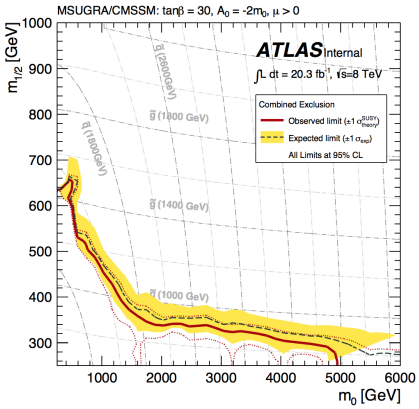

(a) τ-analysis

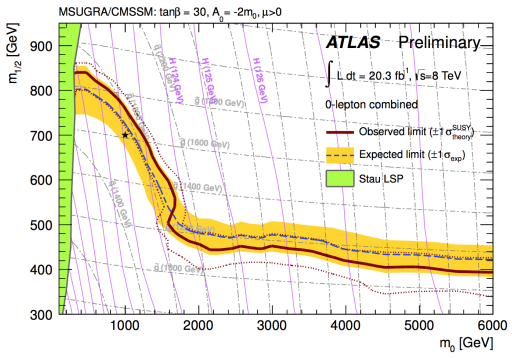

(b) jet-analysis

Figure 7.1: Exclusion limits for sSUGRA/CMSSM models with $\tan\beta = 30$, $A_0 = -2m_0$ and $\text{sign}(\mu) = +1$. The limit in Figure 7.1a is the combined limit for the 1τ, τ + e and $\tau + \mu$ channels in Ref. [1]. The limit in Figure 7.1b is obtained by using the signal region with the best expected sensitivity at each point for the analysis in Ref [2]. The dashed lines show the expected limits at 95%CL, with the yellow bands indicating the 1σ excursions due to experimental and background-theory uncertainties. Observed limits are indicated by red curves, where the solid contour represents the nominal limit, and the dotted lines are obtained by varying the signal cross section by the theoretical scale and PDF uncertainties.

presented here will be simplified version of the analysis in Ref. [1]. Section 7.3 will present the event selection. The background treatment and systematic uncertainties will be described briefly in Section 7.4 and Section 7.5 respectively. Each of these sections will include a description and justification of the relevant simplifications that have been done for the results presented. Four different strategies for optimisation will be presented and discussed in Section 7.7. The full analysis will then be run in a new signal region, proposed on the basis of the results of the optimisation. This will be presented along with new limits in the mSUGRA (m_0,$m_{1/2}$) plane in Section 7.8.

7.1.2 Important kinematic variables

Selecting on certain kinematic variables provides better separation between SUSY signal and SM background than selecting on others. The important variables for this analysis are listed here:

- E_T^{miss}, the missing transverse energy is an important variable in many SUSY

searches with a stable electrically neutral LSP.

- Number of jets, the number of reconstructed jets that above some p_T cut (here 30 GeV).

- H_T, the scalar sum of tau and jet transverse momentum:

$$H_T = p_T^{\tau} + \sum_{\text{all jets}} p_T^{\text{jets}} \tag{7.1}$$

  H_T and N_{jets} are correlated, as every jet adds its p_T to the sum.

- m_T^{τ}, the transverse mass built up by E_T^{miss} and tau p_T:

$$m_T^{\tau} = \sqrt{2 p_t^{\tau} E_T^{\text{miss}} \left(1 - \cos\left(\Delta\phi(\tau, p_T^{\text{miss}})\right)\right)} \tag{7.2}$$

  The transverse mass is a useful quantity to define for use in particle physics as it is invariant under Lorentz boost along the z-direction.

- $\Delta\phi\left(\text{jet}_{1,2}, p_T^{\text{miss}}\right)$ is the azimuthal angle between p_T^{miss} and either of the two leading jets.

- $\Delta\phi\left(\tau, p_T^{\text{miss}}\right)$ is the azimuthal angle between p_T^{miss} and the τ.

7.2 Data and Simulation Samples

7.2.1 Data Samples

The data used in this analysis are from proton-proton collisions recorded at $\sqrt{s} =$ 8 TeV between April 2012 and December 2012, corresponding to periods A-E, G-J and L [**?**]. It is the same data as used in the 1τ and jet analyses. The data is required to be part of a so-called Good Run List (GRL), which is a list of runs that fulfil criteria common to all E_T^{miss}-based SUSY analyses in ATLAS. The total integrated luminosity amounts to 20.3 $\pm$0.6 fb^{-1}, after the application of beam, detector and data-quality requirements. The data was collected from a trigger requiring a jet with high transverse momentum, p_T, and a missing transverse momentum selection on large E_T^{miss}. All events are required to pass the trigger item EF_j80_a4tchad_xe100_tclcw_veryloose [37].

7.2.2 Standard Model Background Simulated Samples

The most important background processes are vector bosons, W and Z, produced together with jets, top quark production and QCD dijets. The background MC samples used in this analysis include simulation of pile-up and are from the "MC12a" production campaign. Tables 66-79 in Ref. [1] describe all background samples used in the analysis in detail. This section provides a more general description. For generator versions and PDF sets used see Chapter 4 of Ref. [37].

W + jets and Z + jets are expected to be the dominant background processes, along with $t\bar{t}$. W and Z are simulated by the Sherpa generator. W/Z + jets events are reweighted based on the p_T of the vector boson using measured Z boson p_T distributions in the data to improve the agreement between MC and data. Various alternative W/Z + jets samples are produced by the Alpgen MC generator [87]. These are used for evaluation of generator uncertainties.

For the $t\bar{t}$ samples, the AFII fast simulation tool has been used. Studies documented in appendix D of Ref. [1] show that for the analysis optimised in this thesis the performance of the AFII $t\bar{t}$ sample is comparable to that of the full simulation. The top quark production is simulated with Powheg [84] interfaced to Pythia [82]. $t\bar{t}$ events are reweighted based on the p_T of the system to improve agreement between data and MC simulation. Alternative samples for evaluation of systematic uncertainties are generated with Alpgen in a similar setting as the one used for W/Z + jets. For the purpose of background estimation $t\bar{t}$ is treated together with single top, as their signatures are similar and difficult to separate. Single top production is simulated using MC@NLO [86] with Herwig [81] and ACER [98] with Pythia for different production channels.

$Z/\gamma*$ events with m_{ll} (the di-lepton mass) < 40 GeV are called "Drell-Yan". These are simulated with the Alpgen MC generator with fragmentation and hadronisation performed in Herwig using Jimmy [85] for underlying event simulation. The cut applied on m_{ll} ensures that these low-mass samples don't overlap with the standard Z + jets samples. This is not true for the Sherpa [83] Z + jets samples, but the contribution from these were found to be small, they have been omitted from the studies [1]. The generator used for simulating the production of diboson (WW, ZZ and WZ) samples is Sherpa. Alternative samples for systematic uncertainties are simulated by Powheg interfaced to Pythia.

The last background considered is QCD. QCD dijet events are simulated with Pythia, but the QCD background level is determined using a data-driven method in the full analysis. This makes the analysis less dependent on MC modelling of the precise cross section.

As W/Z + jets and $t\bar{t}$ are expected to be the dominant backgrounds these are the only backgrounds considered for the optimisation in Section 7.7. This choice is also motivated by the number of background events, listed in Table 7.13, for the

two 1-τ signal regions. In both signal regions diboson and multi-jet account for about 20% of the total background events. The data driven method for estimation of QCD, briefly explained in Section 7.4, is complicated and time-consuming and better left alone up until running the full analysis for the final SR, after optimisation.

Pile-up re-weighting

The MC samples include simulation of pile-up, but for the simulation to better match the data conditions a reweighting is applied. Simulated events are assigned a weight depending on the number of interactions per bunch crossing. The correction is obtained from the 00-02-11 version of the official PileupReweighting tool. Pileup conditions in data are obtained with the GRL from the ATLAS data-preparation group.

b-tag re-weighting

Top decays and direct W+jets production leave similar signatures in the detector. To separate them it is important to identify jets from b-quarks. b-quarks are only expected to appear in top events. Tagging of b-jets is mainly based on the measurement of displaced vertices from long lived hadrons that come from b decays [99]. The efficiency for identifying b-jets depends on the chosen b-tagging algorithm and is not modelled in the MC samples. An event re-weighting technique is therefore used to obtain an MC response comparable to data. Reweighting is done using version 00-03-06 of the CalibrationDataInterface [37].

7.2.3 Signal Monte Carlo Samples

Higgs-aware mSUGRA

The parameters of the mSUGRA model investigated in this thesis are chosen such that across a large area of the $(m_0, m_{1/2})$-plane the lightest Higgs boson of mSUGRA is consistent with the Higgs boson recently discovered at CERN. The parameter values chosen are:

$A_0 = -2 \cdot m_0$

$\tan\beta = 30$

$sign(\mu) = +1$

m_0 and $m_{1/2}$ are treated as grid parameters.

The large negative A_0 was chosen for maximal stop mixing that raises the

Higgs boson mass that would otherwise be too low [100].

In Figure 7.2, the black hatched area represent models with a stau LSP and not the neutralino LSP expected in final states in this analysis. The bright green region to the right of the region with stau LSP is the coannihilation region. Here, the stau is is the second lightest supersymmetric particle, something which favours stau searches. This region is covered by the Higgs-aware grid up to $m_0 = 1000$ GeV, which is the region of the grid used for optimisation in Section 7.7. A high proportion of signal events pass selection cuts in this region. This is illustrated in Figure 7.3b and Figure 7.4b showing the efficiency in each signal region of the 1τ analysis. The term efficiency will be explained in Section 7.6. The red regions in Figure 7.2 are excluded regions due to $B_s \to \mu\mu$ and b→sγ computed with DarkSUSY [88] and IsaJet [89] respectively.

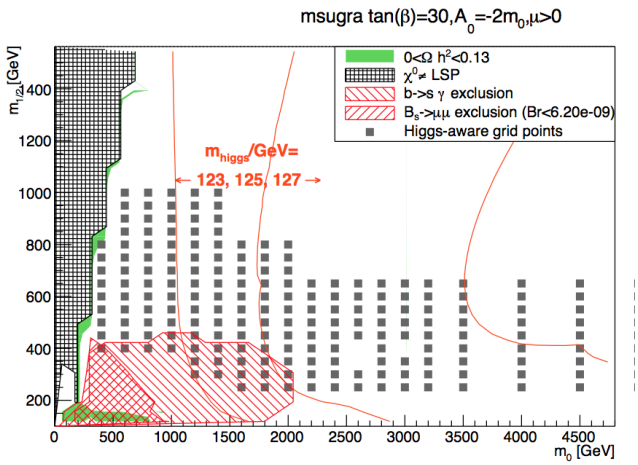

Figure 7.2: Constraints on the Higgs-aware mSUGRA signal grid. The image is taken from ref. [1]

The signal points are produced with softsusy [101] and Herwig++ [81] with a full simulation of ATLAS. The underlying event and parton densities used were UEEE3 [102] and CTEQ [103], respectively. Signal cross sections have been calculated at next-to-leading order in α with the resummation of soft-gluon emission added at next-to-leading-logarithmic accuracy (NLO + NLL) [104–106]. Nominal cross section and uncertainty are taken from an envelope of cross section predictions using different PDF sets and factorisation and renormalisation scales, as described in Ref. [107]. Produced points with m_0 smaller than 1000 GeV are listed in Table 7.1.

The signal grid is made with a spacing of 200 GeV in m_0 and 50 GeV in $m_{1/2}$, except for the eight points with m_0 below 400 GeV. In all grid plots in the following sections values for the two points with $m_0 = 320$ GeV have been averaged and filled in a common grid point. The two points are placed so close they fall into the same bin unless the binning is very fine. The values of the two points are similar for all variables, and the averaging was done to make the plots more readable. Another consequence of this is that it looks like the grid has a gap at

$m_{1/2} \approx 650$ GeV. This is due to the binning. The spacing is 50 GeV in $m_{1/2}$ for all signal points with m_0 larger than 400 GeV.

m_0 [GeV]	$m_{1/2}$ [GeV]	σ [pb]	m_0 [GeV]	$m_{1/2}$ [GeV]	σ [pb]
230	420		600	950	0.000200
250	460		600	1000	0.000110
280	550		800	400	0.167
300	620		800	450	0.0787
320	640		800	500	0.0388
320	660		800	550	0.0198
350	550		800	600	0.0103
350	680		800	650	0.00549
400	400	0.363	800	700	0.00295
400	450	0.173	800	750	0.00160
400	500	0.0843	800	800	0.000872
400	550	0.0424	800	850	0.000477
400	600	0.0217	800	900	0.000247
400	650	0.0111	800	950	0.000144
400	700	0.00595	800	1000	$7.96 \cdot 10^{-5}$
400	750	0.00310	1000	400	0.123
400	800	0.00169	1000	450	0.0561
600	400	0.244	1000	500	0.0270
600	450	0.1179	1000	550	0.0134
600	500	0.0580	1000	600	0.00693
600	550	0.0296	1000	650	0.00373
600	600	0.0153	1000	700	0.00198
600	650	0.00801	1000	750	0.00108
600	700	0.00429	1000	800	0.000594
600	750	0.00233	1000	850	0.000327
600	800	0.00126	1000	900	0.000180
600	850	0.000654	1000	950	$9.99 \cdot 10^{-5}$
600	900	0.000371	1000	1000	$5.56 \cdot 10^{-5}$

Table 7.1: List of MC samples for the SUSY signal in the mSUGRA Higgs boson-aware grid.

7.3 Event Selection

All events are required to pass preselection and cleaning. The event must have a reconstructed primary vertex, it is required to have no jets or muons that show signs of problematic reconstruction, and to have no jets that fail to satisfy quality criteria, and to have no muons that are likely to originate from cosmic muons. The interesting processes have large E_T^{miss} and so data is taken from the JetTauETmiss stream, the trigger chain EF_j80_a4tchad_xe100_tclcw_veryloose [100] is required to have fired. This saves events with $E_T^{\text{miss}} > 100$ GeV and at least one jet with $p_T > 80$ GeV. This trigger cut is only applied to data, so additional kinematic cuts are imposed to the offline reconstructed physics objects in MC data events to exclude trigger turn-on effects. These cuts, in this analysis referred to as plateau cuts, require the presence of at least two jets, the first with $p_T > 130$ GeV, the second with $p_T > 30$ GeV, and $E_T^{\text{miss}} > 150$ GeV.

In the 1τ part of the analysis in Ref. [1] two signal regions are considered, the "loose" and the "tight" signal regions (SR), described with kinematic requirements listed in Table 7.2. Events with only one hadronically decaying medium tau lepton candidate with $p_T > 30$ GeV, no additional loose tau, no muon candidates and no electron candidates are selected. A requirement on $\Delta\phi\left(\text{jet}_{1,2}, p_T^{\text{miss}}\right)$ is used to remove multi-jet events, where E_T^{miss} arises form the mismeasurement of highly energetic jets. The cut on m_T^{τ} is applied to remove W+jets events, and the requirement on H_T is applied to reduce contributions from all backgrounds.

Variable	**Loose SR**	**Tight SR**
N_{τ}^{medium}	$=1$	$=1$
N_{τ}^{loose}	$=1$	$=1$
τp_T	> 30 GeV	> 30 GeV
$\Delta\phi\left(\text{jet}_{1,2}, p_T^{\text{miss}}\right)$	> 0.4	> 0.4
$\Delta\phi\left(\tau, p_T^{\text{miss}}\right)$	> 0.2	> 0.2
m_T^{τ}	> 140 GeV	> 140 GeV
E_T^{miss}	> 200 GeV	> 300 GeV
H_T	> 800 GeV	> 1000 GeV

Table 7.2: Kinematic requirements in the "loose" and "tight" SR of the 1τ analysis in Ref. [1]. The variables listed are defined in Section 7.1.2.

7.4 Background Estimation

In this analysis the background predominantly arises from W + jets, Z + jets, top and multijet events. There are contributions from real, or true, taus as well as jets misidentified as taus, fake taus. The contributions of these types of background in the SRs are estimated from data. The two following sections will introduce the estimation techniques for electroweak (W and Z) and top background and for multijet background in the 1τ analysis. The small diboson contribution is estimated from MC simulations, whilst contributions from other backgrounds have been found negligible [37].

7.4.1 W/Z + jets and top

Electroweak and top quark backgrounds are estimated using the "matrix inversion" method. In each SR the SM background prediction from MC simulation is scaled with scale factors obtained from control regions (CRs). The CRs are chosen so that they are kinematically close to, but not overlapping, the SRs and keep signal contamination low. Each CR is designed to be enriched with a specific background, and the tau misidentification probablility should, to a good approximation, be independent from kinematic variables used to separate CRs from SRs.

As the composition of true and fake taus in the CR and SR can differ, it is necessary to compute separate scale factors for events with true and fake taus. For this reason the CRs are defined by using two variables: m_T^τ is used to separate true and fake taus, and b-tagging is used to provide a top-enriched ($t\bar{t}$ CR) and a top-depleted (W/Z CR) sample. The list of selection requirements, applied after cleaning, tau selection and light-lepton veto, are presented in Table 7.3.

The measured ratio of the data to MC event yield in each CR can then be used to compute scale factors to the correct background prediction in the SR. the vector defined by scale factors for each background ($\overrightarrow{\omega}$) is obtained by inverting the equation

$$N_{\text{data}} = A\overrightarrow{\omega} \tag{7.3}$$

where N_{data} is the observed number of events from data in each CR, after subtraction the expected number of events from other SM processes, and A is a 4×4 matrix from which the scale factors for W events with a true tau candidate, W/Z events with a fake tau candidate, and top events with either a true or a fake tau candidate are obtained. In the Z + jets events, the background is dominated by $Z \to \nu\nu$, and so the tau candidate is typically a misidentified jet. For this reason, the scale factor is obtained from the $CR_{W,\text{fake}}$. This matrix inversion method is explained in detail in Section 5 of Ref. [1].

	$N_{\text{b-jets}} = 0$	$N_{\text{b-jets}} > 0$
$m_T^\tau < 90$ GeV or $\Delta\phi\left(\tau, p_T^{\text{miss}}\right) < 1.0$ or $p_T^\tau > 55$ GeV	$\text{CR}_{\text{W,true}}$	$\text{CR}_{\text{T,true}}$
90 GeV $< m_T^\tau < 140$ GeV and $\Delta\phi\left(\tau, p_T^{\text{miss}}\right) > 1.0$ and $p_T^\tau < 55$ GeV	$\text{CR}_{\text{W,fake}}$	$\text{CR}_{\text{T,fake}}$

Table 7.3: Control regions employed for the background estimation of W, Z and top quark backgrounds in the one tau analysis. Trigger cuts and selected objects are identical to the signal region cuts in the respective channels, and a multijet rejection cut of $\Delta\phi\left(\text{jet}_{1,2}, p_T^{\text{miss}}\right) > 0.4$ is applied in all CRs.

Typical scale factors are ∼0.6 for W/Z + jets and ∼1.0 for $t\bar{t}$ with fake taus, and ∼1.0 for W + jets and ∼1.0 for $t\bar{t}$ with true taus. As these scale factors are all, apart from the fake tau W/Z + jets one, close to one the optimisation is carried out with no scale factors applied. As it is done consistently this simplification should not have a big impact in the result of the optimisation. This choice is also justified by the large statistic and systematic uncertainties on the scale factors, see Table 7.10.

7.4.2 Multijet

For the 1τ analysis, the contribution arising from multijet background processes due to fake taus is estimated from data using the so-called "ABCD" method. This method allows a data-driven estimate of a background rate in four exclusive regions, labelled A, B, C and D, defined in a two-dimensional plane specified by two uncorrelated discriminating variables, such that both of the cuts enhance the signal-to-background ratio. The variables used are E_T^{miss} and $\Delta\phi\left(\text{jet}_{1,2}, p_T^{\text{miss}}\right)$, and the CRs are defined in Table 7.4

The ABCD-method is explained in Section 5.2.3 of Ref. [1]. As mentioned in Section 7.2.2 it is complex and time-consuming, and the background contribution from multijets is smaller than the contribution from top, W + jets and Z + jets backgrounds. The Multijet background is therefore left out of the optimisation, and even the full analysis presented in Section 7.8. Instead scaled extra loose taus are used. Extra loose taus are reconstructed taus with no BDT requirement. Background events from multijet production contain both fake E_T^{miss} from

	Very loose τ	Medium τ
$\Delta\phi\left(\text{jet}_{1,2}, p_T^{\text{miss}}\right) < 0.4$		
No cut on E_T^{miss}	CR A	CR B
$\Delta\phi\left(\text{jet}_{1,2}, p_T^{\text{miss}}\right) > 0.4$		
$E_T^{\text{miss}} < 200/300$ GeV	CR C	CR D

Table 7.4: Control regions for the background estimation of multijet backgrounds in the 1τ analysis. The requirement on HT is not applied in the definition of these control regions.

instrumental effects in the jet energy measurements and fake taus. Since both effects are difficult to simulate reliably and the large cross section would require very large simulation samples, the method preferred would be the "Jet Smearing" technique [108], used in the 2τ analysis in Ref. [1].

7.5 Systematic Uncertainties

A large number of systematic uncertainties were studied as part of the 1τ analysis. The effect on the number of events in each SR was calculated. The systematic uncertainties arise predominantly from the estimation of the number of background events in the signal sample and from the generator and detector uncertainties in simulating signal efficiencies. Because of the normalization procedure in the CRs, these estimates are not affected by theoretical errors on absolute cross sections, but only by generator dependencies when extrapolating from the CRs to the SRs.

The difference in the estimated number of background events from two different generators, see Section 7.2.2, is used to define the uncertainty due to the choice of MC generator for the top, W+jets, Z+jets and diboson samples. The backgrounds have been recomputed using different generators to account for variations due to theory assumptions. For W, Sherpa is compared to Alpgen+Herwig using the susy-filtered samples to increase the available MC statistics in the studied kinematic range for the hadronic channels. For Z, Sherpa is compared to Alpgen+Pythia for the charged lepton decays of the Z and Alpgen+Herwig for the neutrino decays. Powheg $t\bar{t}$ is compared to Alpgen. For dibosonsS, herpa is compared to Powheg+Pythia8.

The experimental systematic uncertainties on the SM background estimates arise from

jet energy scale (JES) and resolution JER) : The relation between a calorime-

ter signal and the corresponding jet energy is not known precisely. The uncertainty on the jet energy scale (JES) is determined by the Jet/Etmiss performance group in MC studies. The JER is only simulated with finite precision by the Geant4 detector simulation. The agreement between the jet energy resolution in data and simulation has been studied using the spread of the p_T imbalance in dijet events and with different techniques [109].

tau energy scale (TES) : Systematic uncertainties for the tau energy scale (TES) are under study by the Tau Working Group. They have been determined in Monte Carlo truth studies varying parameters affecting the tau energy reconstruction and evaluating the influence on the scale [110].

tau identification (TauId) : In general, these uncertainties depend on the tau identification algorithm used for the τ ID, the kinematics of the τ sample, and the number of associated tracks [77].

The uncertainties from the jet and tau energy scales are the largest experimental uncertainties and are treated as uncorrelated, given that they are calibrated by different methods. The systematic uncertainty associated with the simulation of pile-up is taken into account by recomputing the event weights in all MC samples such that the resulting variation in the average interactions per bunch crossing corresponds to the observed uncertainty.

The 1τ analysis uses tau identification, reconstructed jets and missing transverse energy to define the SR, and the control regions and the extrapolation of background scale factors into the signal region also rely on these objects. To model the performance of these objects, systematic uncertainties are estimated in the following way. The relative difference between the number of expected background events obtained with the nominal MC simulation and that obtained after applying the uncertainty variations on the corresponding objects is taken to be the systematic uncertainty on the background estimate. The relative uncertainty is evaluated in a widened signal region to avoid the evaluation of systematics on that number is too strongly influenced by limited MC statistics. For the loose SR the H_T cut is lowered from 800 GeV to 600 GeV. For the tight SR the H_T cut is lowered from 1000 GeV to 800 GeV. For each background type the corresponding relative variation is then applied to the predicted number for a given SR, and the resulting absolute variations added to form a modified total background prediction. This procedure takes correlations between backgrounds into account, which arise from the scale factor corrections. An overview of all systematic and statistical uncertainties for the loose and tight SR of the 1τ analysis can be found in Table 28 and Table 29 in Ref. [1], respectively.

This calculation of systematic uncertainties is handled in the same way in the limit setting procedure, where variations of the total background prediction are

used. For the following analysis systematic uncertainties are evaluated only in the final SR in Section 7.8.

7.6 Signal Efficiencies

The efficiency, ε, of a selection is the fraction of signal events accepted by this selection. The fraction of MC generated signal events that make it through the entire cutflow to all generated signal events is however not ε. The acceptance, $A_{\text{cc}} = N_{\text{rec}}/N_{\text{true}}$, also has to be taken into consideration. N_{rec} is the number of events reconstructed in a bin, and N_{true} is the true number of events generated and possessing distinct signal characteristic, namely exactly one real tau, in a bin.

Efficiency times acceptance for the loose and tight SRs summarised in Table 7.2 are shown in Figure 7.3b and Figure 7.4b respectively, in the version of the analysis done for this thesis.

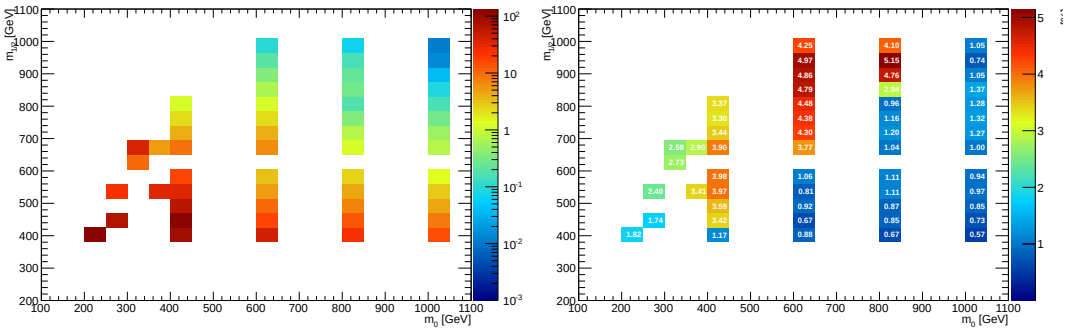

(a) Expected number of events

(b) Efficiency x Acceptance [%]

Figure 7.3: Number of events expected and Efficiency x Acceptance in the loose SR, summarised in Table 7.2.

In the loose SR $\varepsilon \times A_{\text{cc}}$ ranges from about 0.6% for low $m_{1/2}$ and m_0 up to 1000 GeV to 5% in the region with high $m_{1/2}$ and m_0 between 600 and 800 GeV. This is promising, as this thesis focusses on optimising the latter region. The uncertainties on $\varepsilon \times A_{\text{cc}}$ are not shown, but are for most signal points 1/10 - 1/5 of the value. For the points with $m_{1/2} > 950$ GeV the uncertainty is comparable to the $\varepsilon \times A_{\text{cc}}$. In addition to this, the number of events expected in the loose SR, shown in Figure 7.3a, is between 0.1 and 1 for the part of the $(m_0, m_{1/2})$ mass plane interesting to the following optimisation.

In the tight SR $\varepsilon \times A_{\text{cc}}$ ranges from about 0.4% for low $m_{1/2}$ and m_0 up to 1000 GeV to 4.5% in the region with high $m_{1/2}$ and m_0 between 600 and 800 GeV.

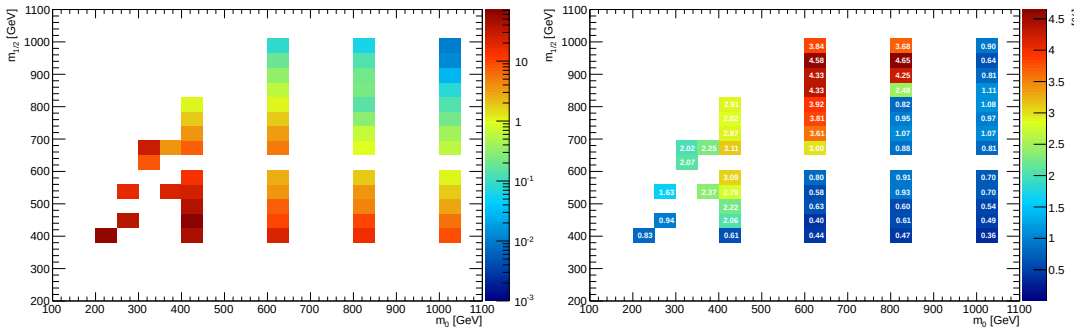

(a) Expected number of events

(b) Efficiency x Acceptance [%]

Figure 7.4: Expected number of events and Efficiency x Acceptance in the tight SR, summarised in Table 7.2.

The number of events expected in the SR, shown in Figure 7.4a, lie between 0.1 and 1, as for the loose SR.

For comparison, the corresponding plots of expected number of events and acceptance times efficiency in the existing 1τ analysis [1] are shown in Figure7.5.

The plots in Figure 7.5 show expected number of events and $\varepsilon \times A_{\text{cc}}$ for a larger part of the mSUGRA signal grid, up to $m_0 = 5500$ Gev, than Figure 7.3 and Figure 7.4. This is because the simplified analysis in this thesis is done for the region of the $(m_0, m_{1/2})$ mass plane where the produced signal samples for mSUGRA are Higgs aware, as described in Section 7.2.3. For signal points with $m_0 < 1000$ GeV both number of events expected and $\varepsilon \times A_{\text{cc}}$ agree with the corresponding numbers in Figure 7.3 and Figure 7.4.

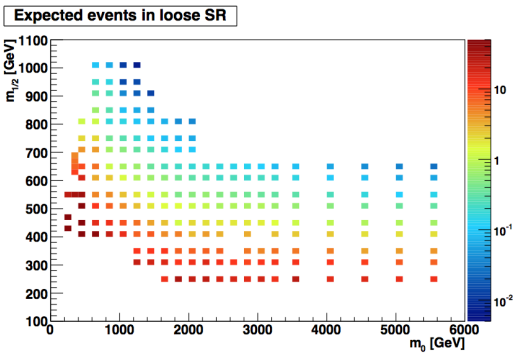

(a) Expected number of events in the loose SR

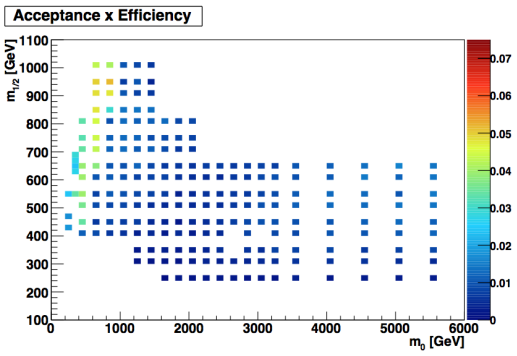

(b) Acceptance x Efficiency in the loose SR

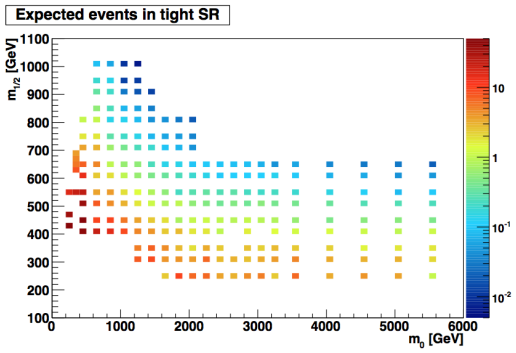

(c) Expected number of events in the tight SR

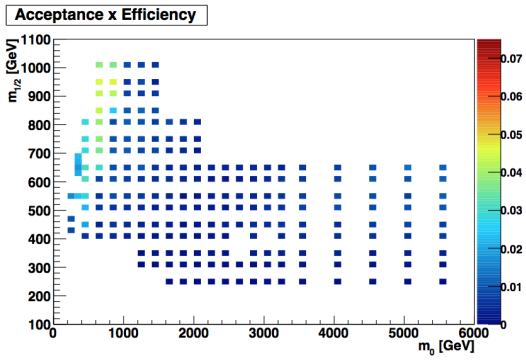

(d) Acceptance x Efficiency in the tight SR

Figure 7.5: Expected number of events and Acceptance x Efficiency for the loose SR (top half plots) and tight SR (lower half plots), summarised in Table 7.2, for the mSUGRA signal grid in the 1τ analysis. The plots are taken from Ref. **??**.

7.7 Optimisation

This section presents four strategies for optimisation of analysis in search for SUSY with 1 τ in the low m_0 ($m_0 < 1000$ GeV) high $m_{1/2}$ region of the (m_0, $m_{1/2}$) mass plane in mSUGRA. The signal samples are in this region compatible with a Higgs boson of mass $m_H = 125$ GeV. Most values will be shown in grid plots for all grid points in the interesting region. Some will be shown for a few selected signal points with m_0 between 400 and 800 GeV and $m_{1/2}$ between 800 and 1000 GeV.

Two benchmark points are chosen. One point, $m_0 = 400$ GeV and $m_{1/2} = 800$ GeV is not excluded by the 1τ analysis in Ref. [1], but is excluded by the analysis where no τ is required, in Ref. [2], as shown in Figure 7.1a and Fig-

ure 7.1b respectively. the second point, $m_0 = 600$ GeV and $m_{1/2} = 850$ GeV, is not excluded in the 1τ analysis. In the analysis that does not require a τ lepton the second benchmark point falls exactly on the 1σ uncertainty of the observed limit in Figure 7.1b.

The redone 1τ analysis in this thesis does not take multijet or diboson backgrounds into consideration until the new SR is proposed in Section 7.8. It is also possible that parts of the framework SusyOneTauCore, mentioned in Chapter **??**, has updated, and that this analysis has not been fully updated. Either way, the differences should be enough for the following optimisation conclusions to be valid in the context of improving the official analysis. In the optimisation new results are compared to the simplified version of the 1τ analysis, which is not identical to the analysis in Ref. [1], but which should still provide insight into the general direction to go with optimised cuts.

7.7.1 Asimov Significance

In this analysis the main goal is to optimise the sensitivity to unseen SUSY-processes. The statistical significance of an observed signal can be quantified by the means of a p-value. For purposes of discovering a new signal process, one defines the null hypothesis, H_0, as describing only known processes, background processes. This is tested against a different hypothesis, H_1, which includes both background and signal processes. In a counting experiment, the counted number of events n is the sum of background processes b and signal processes s. This would lead to H_0 being the scenario where $s = 0$. The p-value is the probability, under assumption of H_1, of finding data of equal or greater incompatibility with the predictions of H_1.

In particle physics one usually converts the p-value into an equivalent significance,

$$Z = \Phi^{-1}(1 - p) \tag{7.4}$$

where Φ^{-1} is the inverse of the cumulative distribution (the quantile) of the standard Gaussian. The sensitivity of an experiment can be characterised by reporting the expected (mean or median) significance that one would obtain for a variety of signal hypotheses. It has proven useful to estimate the median significance by replacing the simulated data sets by a single representative one: the "Asimov" data set. The Asimov data set is an artificial data set defined so that when one uses it to evaluate the estimators for all parameters, one obtains the true parameter values [111].

In this analysis optimisation involves maximising the Asimov discovery significance, z_A, described in Ref. [111], with the modification presented in Ref. [112]. In the case that uncertainty on the background, σ_b, is taken into account, the

expected significance will be

$$z_A = \left[2 \left((s+b) \ln \left[\frac{(s+b)(b+\sigma_b^2)}{b^2 + (s+b)\sigma_b^2} \right] - \frac{b^2}{\sigma_b^2} \ln \left[1 + \frac{\sigma_b^2 s}{b(b+\sigma_b^2)} \right] \right) \right]^{1/2} \tag{7.5}$$

z_A reduces to $s/\sqrt{b+\sigma_b^2}$ in the large statistics limit. The benchmark points in this analysis have very small cross sections. The significance is small and the z_A provides a better description of the Poisson fluctuations than $s/\sqrt{b+\sigma_b^2}$ for low event yields, and the significances in the following sections are Asimov significances computed with Eq. 7.5.

7.7.2 H_T

In the one tau analysis, after the events pass the trigger and baseline event selection, additional cuts are applied to select signal and reject as much of the background as possible. The H_T cut is the last cut to be applied. It is designed to reject primarily $Z \to \nu\nu$, dibosons, and W+jets and top where a jet is misidentified as a tau or where E_T^{miss} receives other contributions than the neutrinos from the W decay. The only difference between the loose and tight SR, summarised in Table 7.2, lies in the harder cut on H_T and E_T^{miss} in the latter.

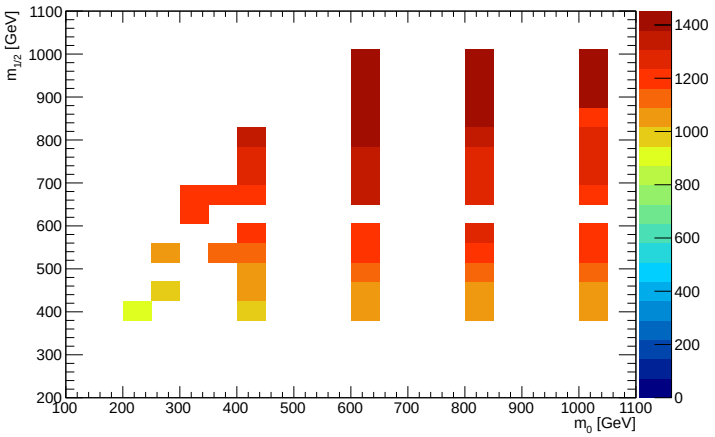

Figure 7.6: The average value of H_T in the loose SR across the mSUGRA signal grid.

The average value of H_T for the signal points in the mSUGRA signal grid, shown for the loose SR in Figure 7.6, would suggest that cutting quite high on H_T would still leave a lot of signal. The average values for signal points in the low m_0, high $m_{1/2}$ region lie between 1200 GeV and 1400 GeV, while the cuts

in the existing analysis are 800 GeV and 1000 GeV in the loose and tight SR, respectively.

In Figure 7.7a the H_T distribution for top, W + jets, Z + jets backgrounds, data and the two benchmark points for mSUGRA signal in the loose SR is presented. The distribution is here shown after the plateau cuts, explained in Section 7.3. At this early stage in the event selection the distribution falls off faster for background than for signal, for higher values of H_T. There is some disagreement between data and background MC for $H_T > 1200$ GeV. In Figure 7.7b the scaled H_T distribution is shown, also after plateau cuts. Each background (true and fake) is scaled with the appropriate scale factor, calculated for the 1τ analysis in Ref. [1]. The numbers are summarised in Table 7.10. As the scale factors are ~ 1, there is no improvement with scaling. $\omega_W^{fake} = 0.6$, and so the agreement is actually worse.

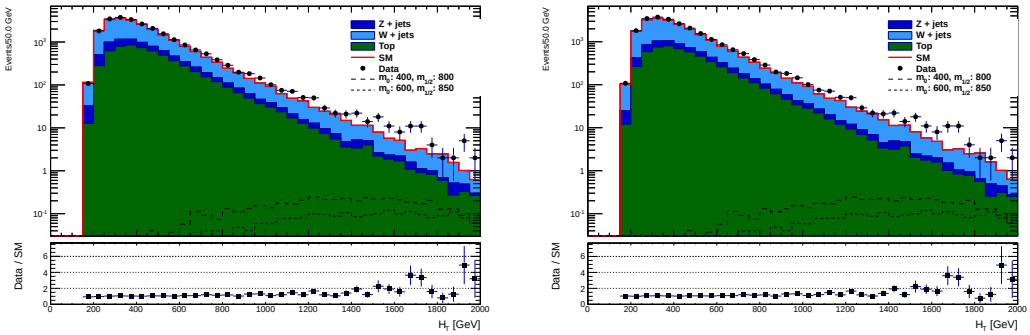

(a) Unscaled.

(b) Scaled.

Figure 7.7: The distribution of H_T in the loose SR defined in Table 7.2after plateau cuts. In the right hand plot the various background distributions have been scaled with the appropriate scale factor from Table 7.10.

$H_T = p_T^\tau + \sum_{\text{all jets}} p_T^{\text{jets}}$, and the disagreement mainly comes from p_T of the first jet, shown in Figure 7.8. As explained, the redone 1τ analysis in this thesis does not take multijet or diboson backgrounds into consideration until the new SR is proposed in Section 7.8. The missing MC background events could stem from these, or possibly a bug in the analysis code. It could also be that parts of the framework SusyOneTauCore, mentioned in Chapter **??**, was updated at some point, and this analysis was not. Either way the differences are small enough for your optimisation conclusions to be valid as well in the context of improving the official analysis.

Placing a cut on H_T based on the signal alone could prove very inefficient. The cut must reduce the background as well as keep as many signal events as

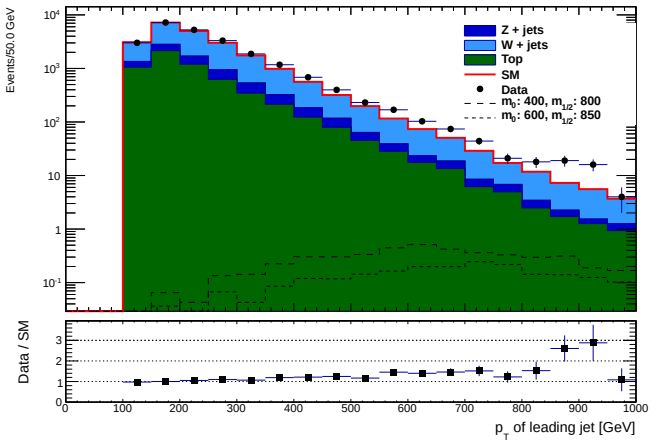

Figure 7.8: The distribution of p_T of the first jet in the loose SR defined in Table 7.2 after plateau cuts.

possible. The agreement between data and background MC is reasonable, even for the higher H_T values. Calculation of the Asimov significance as a function of H_T should provide information on where it would be best to place a cut on H_T.

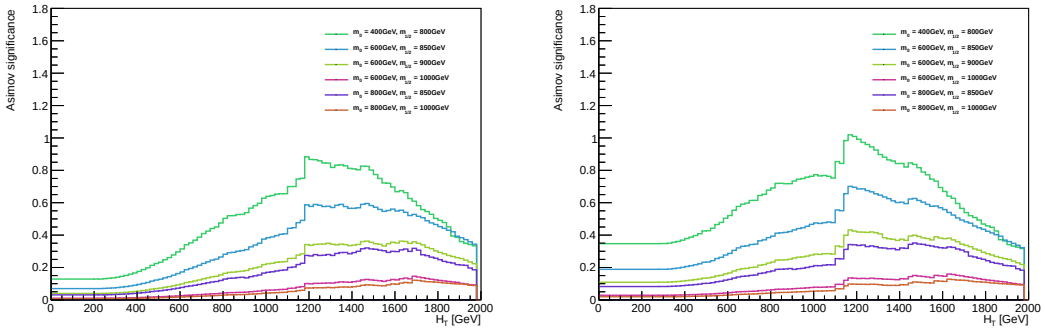

(a) Loose SR (b) Tight SR

Figure 7.9: The Asimov approximation of the signal significance as a function of H_T cut, including the background and its uncertainties, for selected mSUGRA grid points from Table 7.1. The loose and tight SRs are as defined in Table 7.2, but with H_T cut varied.

The plot in Figure 7.9 would suggest that a cut on $H_T > 1200$ GeV would be efficient, both for $E_T^{\text{miss}} > 200$ GeV and $E_T^{\text{miss}} > 300$ GeV. For the benchmark point with $m_0 = 400$ GeV and $m_{1/2} = 800$ GeV, the Asimov significance has peak

values of 0.9 and 1 for $H_T = 1200$ GeV. The second benchmark point, $m_0 = 600$ GeV and $m_{1/2} = 850$ GeV, has has peak values for the Asimov significance of 0.55 and 0.7 for $H_T = 1200$ GeV.

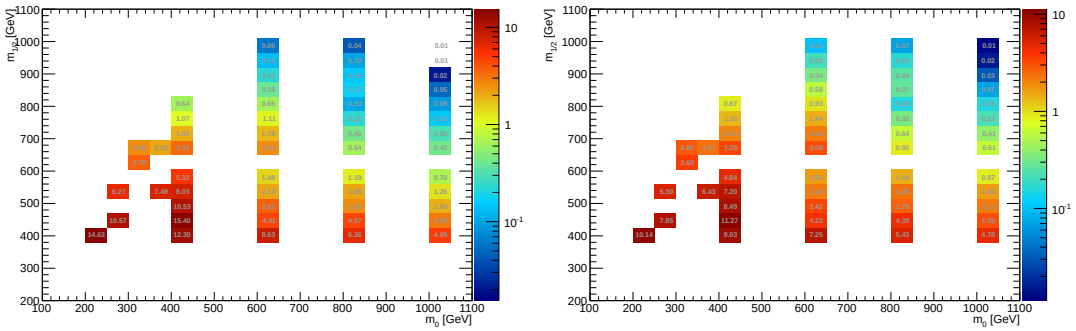

(a) $H_T > 1000$ GeV (b) $H_T > 1200$ GeV

Figure 7.10: The Asimov approximation of the signal significance as a function of H_T cut, including the background and its uncertainties, across the mSUGRA grid in the loose SR defined in Table 7.2, with higher H_T cuts.

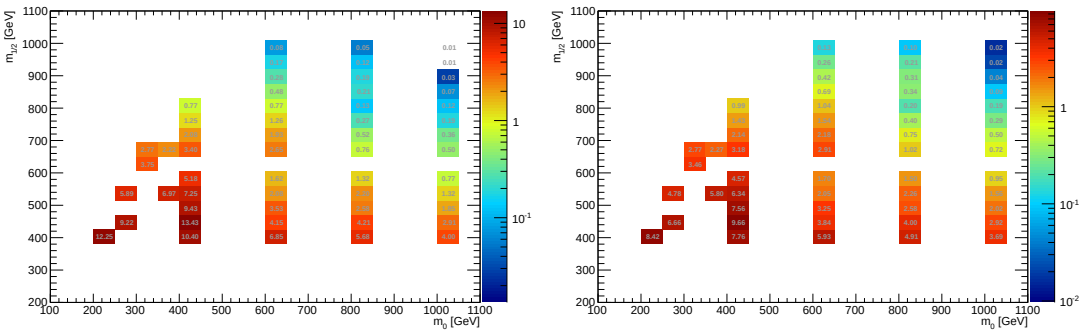

(a) $H_T > 1000$ GeV (b) $H_T > 1200$ GeV

Figure 7.11: The Asimov approximation of the signal significance as a function of H_T cut, including the background and its uncertainties, across the mSUGRA grid in the tight SR, defined in Table 7.2, with H_T cut varied.

Figure 7.10 and Figure 7.11 show Asimov significance across the grid. The plots on the left show significance for $H_T > 1000$ GeV, which is the tight cut in the 1τ analysis. The plots on the right show significance for $H_T > 1200$ GeV. Figure 7.10a shows that the values of Asimov significance in the loose SR, with $E_T^{\text{miss}} > 200$ GeV, range from 0.04 - $\sim$2 for $m_0 < 800$ GeV and $m_{1/2} > 700$

GeV with a cut on $H_T > 1000$ GeV. When the cut is increased to 1200 GeV in Figure 7.11a the values of Asimov significance increase to 0.07 - 2.16. In the tight SR with $E_T^{\text{miss}} > 300$ GeV, shown in Figure 7.11, the values increase from 0.05 - 2.08 to 0.10 - 2.18.

7.7.3 Loose τ

One of the cuts that remove the largest chunks of events, from both signal and background, is the requirement of one medium τ. Medium taus where defined in Section 5.2.2. The cutflow for the benchmark point, $m_0 = 400$ GeV and $m_{1/2} = 800$ GeV, shown in Table **??** is typical for the signal points with low m_0 and high $m_{1/2}$ in the loose SR form Table 7.2. Selecting events with > 0 taus reduces the number of events from 6.49 to 5.29. The requirement of one tau reduces the number of events by almost 50%, from 3.86 to 2.17.

Cut	**Total**	True τ	Fake τ
Cleaning	6.49	5.20	1.30
Trigger	6.49	5.20	1.30
$E_T^{miss} > 150$ GeV, > 0 tau	5.29	5.02	0.27
2 jets, jet_1 $p_T > 130$ GeV	5.11	4.84	0.26
jet_2 $p_T > 30$ GeV	5.11	4.84	0.26
Electron veto	4.48	4.26	0.22
Muon veto	3.86	3.65	0.21
Tau veto	2.17	2.09	0.09
$\Delta(\tau, E_T^{\text{miss}}) > 0.4$	1.88	1.80	0.08
$E_T^{\text{miss}} > 200$ GeV	1.84	1.76	0.08
$m_T^{\tau} > 140$ GeV	1.23	1.17	0.07
$H_T > 800$ GeV	1.16	1.10	0.06

Table 7.5: Cutflow for mSUGRA signal point $m_0 = 400$ GeV and $m_{1/2} = 800$ GeV in the loose signal region, medium τ.

The tau definition used is the medium one, explained in Section 5.2.2. A possible way of including more events with taus is by using the loose tau definition instead. Table 7.6 shows the cutflow for the same benchmark point, $m_0 = 400$ GeV and $m_{1/2} = 600$ GeV, with loose taus.

After the requirement of > 0 taus, the number of events is reduced to 6.16. Selecting events with exactly one tau still throws out a lot of events, but in the

Cut	**Total**	True τ	Fake τ
Cleaning	6.49	5.81	0.68
Trigger	6.49	5.81	0.68
$E_T^{miss} > 150$ GeV, > 0 tau	6.16	5.62	0.54
2 jets, jet_1 $p_T > 130$ GeV	5.94	5.42	0.52
jet_2 $p_T > 30$ GeV	5.94	5.42	0.52
Electron veto	5.24	4.79	0.45
Muon veto	4.49	4.11	0.38
Tau veto	2.54	2.37	0.17
$\Delta(\tau, E_T^{\text{miss}}) > 0.4$	2.20	2.04	0.16
$E_T^{\text{miss}} > 200$ GeV	2.15	1.99	0.16
$m_T^{\tau} > 140$ GeV	1.48	1.33	0.14
$H_T > 800$ GeV	1.39	1.25	0.13

Table 7.6: Cutflow for mSUGRA signal point $m_0 = 400$ GeV and $m_{1/2} = 800$ GeV in the loose signal region, loose τ

final selection choosing loose taus leaves 1.39 events, whilst choosing medium taus leaves 1.16 events. Removing tau veto was investigated in the context of previous tau papers, but no published conclusions exist. This is still something for the future.

Changing the tau definition could lead to improved Asimov significance as a function of H_T cut. Figure 7.12 shows the Asimov significance for selected signal points in the loose and tight SR. For the first benchmark point, $m_0 = 400$ GeV and $m_{1/2} = 800$ GeV, the Asimov significance has peak values of 0.85 and 1.15 for $H_T = 1200$ GeV in the loose and tight SR respectively. This is comparable to the result from Section 7.7.2, slightly worse in the loose SR, but better in the tight SR. The second benchmark point, $m_0 = 600$ GeV and $m_{1/2} = 850$ GeV, has has peak values for the Asimov significance of 0.55 and 0.75 for $H_T = 1200$ GeV. Compared to the results in Section 7.7.2, the Asimov significance for this point is the same for $H_T = 1200$ GeV in the loose SR, but with an additional peak of about the same hight at $H_T = 1700$ GeV. This behaviour can also be seen for the signal points with higher $m_{1/2}$, in Figure 7.12a. For these points it seems like cutting even higher than 1200 GeV on H_T could benefit the analysis. However, the value of Asimov significance is higher for a cut on H_T at 1200 GeV in the tight SR than for cuts at 1700 GeV in the loose SR for all points in Figure 7.12, except for the two signal points with $m_{1/2} = 1000$ GeV. These signal points are

not excluded by neither the 1τ analysis in Ref [1] nor the analysis where no tau is required in Ref. [2]. Optimisation for the points that are chosen as benchmark points is more likely to lead to sensible results.

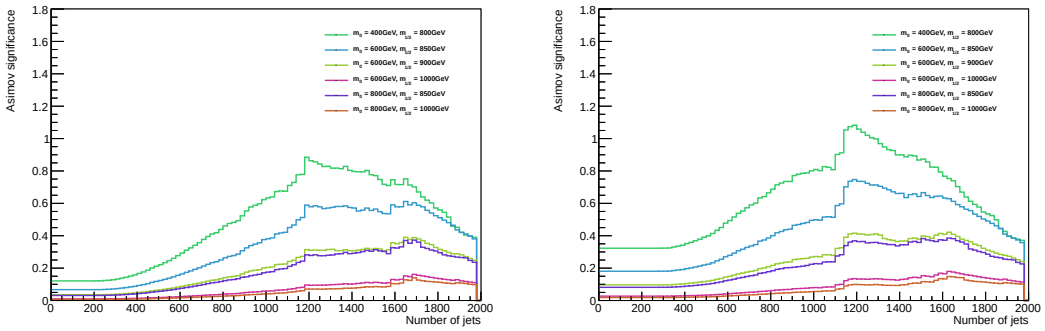

(a) Loose SR (b) Tight SR

Figure 7.12: The Asimov approximation of the signal significance as a function of H_T cut, including the background and its uncertainties, for selected mSUGRA grid points ifrom Table 7.1 selecting one loose tau.

Asimov significance across the signal grid for $H_T > 1200$ GeV with loose taus is shown in Figure 7.13. Figure 7.13a shows that the values of Asimov significance in the loose SR, with $E_T^{\text{miss}} > 200$ GeV, lie in the range 0.07 - 2.27 for $m_0 < 800$ GeV and $m_{1/2} >$. In the tight SR the values of Asimov significance increase to 0.10 - 2.43. The Asimov significance has values comparable to the values is Figure 7.10b and Figure 7.11b, where the medium tau definition is used, for the signal points with $m_{1/2} > 900$ GeV. For the signal points that are only just excluded in Figure 7.1b, but not in 7.1a, there is an improvement.

7.7.4 Tau $p_T > 20$ GeV

As mentioned in Chapter 5 the requirement for reconstruction of a tau candidate is for it to have $p_T > 20$ GeV. In the recently published version of the 1τ analysis the taus were required to have $p_T > 30$ GeV. The quick test of the effect of loosening the cut on the tau p_T from 30 GeV to 20 GeV was motivated by the fact that this cut was changed only recently. The cut on the p_T of the taus was raised compared to the search conducted on the 7 TeV data [113] in order to reduce the Z+jets contribution with low-p_T jets misidentified as tau leptons in the analysis.

Figure 7.14 shows Asimov significance as a function of H_T for loose taus with a tau p_T cut at 20 GeV in the loose (left) and tight (right) SR. The distribution

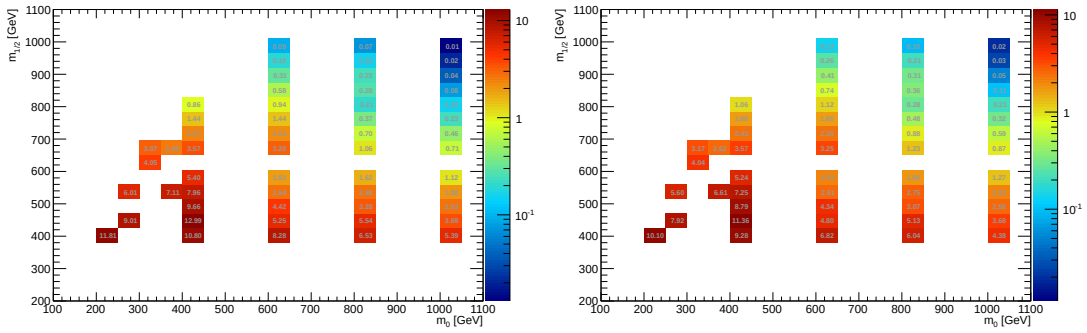

(a) Loose SR (b) Tight SR

Figure 7.13: The Asimov approximation of the signal significance for $H_T > 1200$ GeV, including the background and its uncertainties, across the mSUGRA grid. Loose taus with $p_T > 30$ GeV.

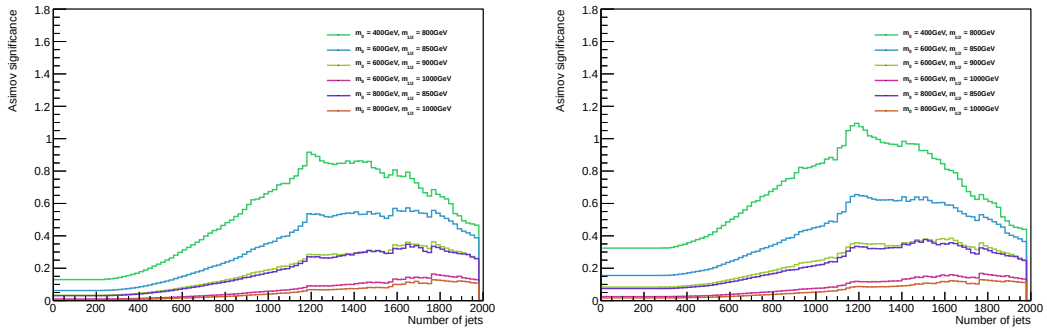

(a) Loose SR (b) Tight SR

Figure 7.14: The Asimov approximation of the signal significance as a function of H_T cut, including the background and its uncertainties, for selected mSUGRA grid points from Table 7.1. Loose taus with $p_T > 20$ GeV.

in the loose SR, in Figure 7.14a, is similar to the one in Figure 7.13a for a cut on tau p_T at 30 GeV. The values of the Asimov significance for the benchmark points in the tight SR, in Figure 7.14b do not show improvement compared to the corresponding values in Figure 7.13b for a cut on tau p_T at 30 GeV. There is a local maxima for an H_T cut at 1500 GeV, but is cannot compete with the significance of a cut at 1200 GeV.

Asimov significance across the signal grid for loose taus with $p_T > 20$ GeV in the tight SR is shown in Figure 7.15. Compared to the same plot for loose taus with $p_T > 30$ GeV in Figure 7.13b there is a slight improvement for signal points

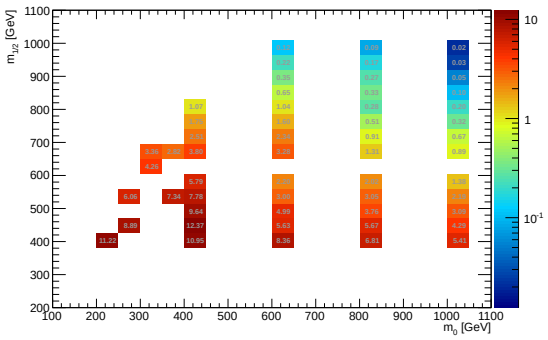

Figure 7.15: The Asimov approximation of the signal significance for $H_T > 1200$ GeV, including the background and its uncertainties, across the signal grid in the 1 tau analysis. Loose taus with $p_T > 20$ GeV in the tight SR.

with low m_0 and $m_{1/2} < 700$ GeV, but for the signal points with higher $m_{1/2}$ the value of the Asimov significance decreases.

7.7.5 Number of jets

The analysis searching for SUSY in final states with jets and missing transverse momentum [2] works with an impressive amount of signal regions. There are five inclusive analysis channels characterised by increasing jet number from two to six, labelled A to E. Each channel includes between one and three SRs. These SRs are defined as "loose", "medium" or "tight", depending on requirements on E_T^{miss}/m_{eff} and m_{eff}(inclusive) [2]. The 2τ analysis in Ref. [1] also makes use of the number of jets for optimisation. This motivates a study of the Asimov significance as a function of number of jets.

The average number of jets in the loose SR across the mSUGRA signal grid is shown in Figure 7.16. In the low m_0 and high $m_{1/2}$ region of the $(m_0, m_{1/2})$ mass plane the average number of jets is between 4.4 and 5. Figure 7.17 shows the distribution of number of jets for top, W + jets and Z + jets background, data and the two signal benchmark point, after the plateau cuts defined in Section 7.3. The number of jets falls of faster for backgrounds than for the two signal points.

The Asimov approximation of the signal significance as a function of number of jets for selected mSUGRA signal points having one loose tau with $p_T > 30$ GeV is presented for the loose (left) and tight (right) SR in Figure 7.18. In the loose SR the Asimov significance does not get higher than 0.5 for the benchmark point with $m_0 = 400$ GeV and $m_{1/2} = 800$ GeV, as shown in Figure 7.18a. This is the value of the significance for a cut on two jets, which is the cut used in the

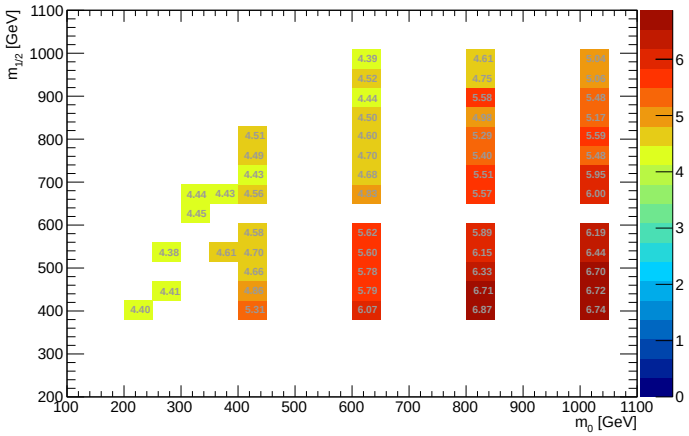

Figure 7.16: The average number of jets in the loose SR across the mSUGRA signal grid.

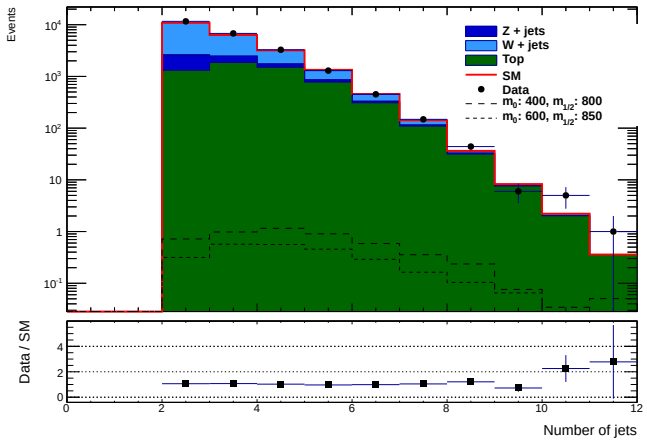

Figure 7.17: The distribution of number of jets after plateau cuts.

1τ analysis in Ref. [1]. The situation is not much better for the tight SR, shown in Figure 7.18b. In this plot the Asimov significance does not get higher than 0.8 for the same benchmark point.

The Asimov significance for a cut at 2 and 3 jets is presented in Figure 7.19a and Figure 7.19b across the signal grid for events with loose taus in the tight SR. These Asimov significance values are comparable to the values presented in Figure 7.10a and Figure 7.11a for the tight and loose SR, respectively, with $H_T >$ 1000 GeV and medium taus with $p_T > 30$ GeV.

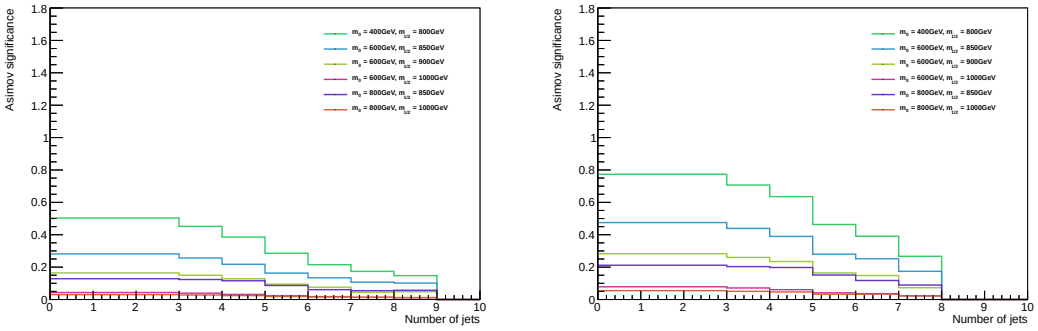

(a) Loose SR (b) Tight SR

Figure 7.18: The Asimov approximation of the signal significance as a function of number of jets, including the background and its uncertainties, for selected mSUGRA grid points from Table 7.1. These are events with one loose taus with $p_T > 30$ GeV

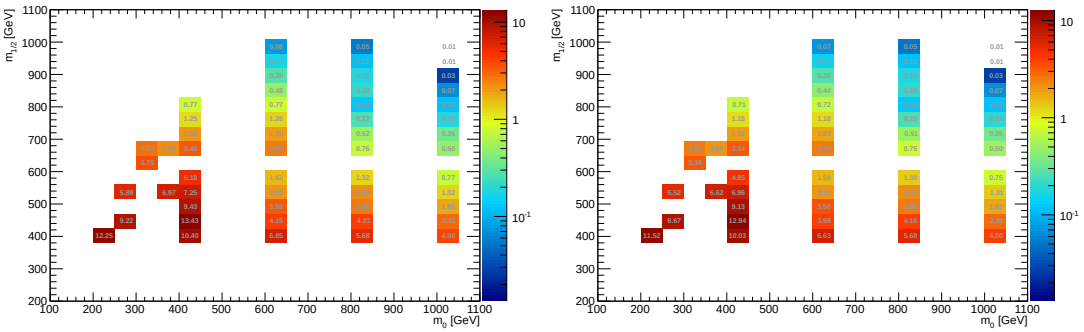

(a) Number of jets > 2 (b) Number of jets > 3

Figure 7.19: The Asimov approximation of the signal significance as a function of number of jets, including the background and its uncertainties, across the mSUGRA grid in the tight SR. These are events with one loose tau with $p_T > 30$ GeV

7.8 Setting a new limit

The optimisation in the previous sections suggests a new signal region selecting one loose tau, with a higher cut on $H_T > 1200$ GeV and the 'tight' cut on E_T^{miss}. The cut on number of jets and p_T of the tau will remain as in the existing 1τ analysis [1], as shown for the tight SR in Table 7.2. The new SR is summarised in Table 7.7.

Variable	**New SR**
N_τ^{loose}	$=1$
τp_T	> 30 GeV
$\Delta\phi\left(\text{jet}_{1,2}, p_T^{\text{miss}}\right)$	> 0.4
$\Delta\phi\left(\tau, p_T^{\text{miss}}\right)$	> 0.2
m_T^τ	> 140 GeV
E_T^{miss}	> 300 GeV
H_T	> 1200 GeV

Table 7.7: Kinematic requirements in the new SR of the 1τ analysis. The variables listed are defined in Section 7.1.2.

The full analysis has been done in this new SR. All systematic uncertainties are listed in Table 7.8. The acronyms in this table are introduced in Section 6.1 of Ref. [1]), and some are explained in Section 7.5 of this thesis. The systematic uncertainties are obtained by use of the method also briefly explained in this section. For a more detailed explanation see Chapter 6 of Ref. [1]. To avoid that measured variations on the predicted number of events in the new SR will be too strongly influenced by limited MC statistics, the relative variation are evaluated in a region where the H_T cut has been relaxed to 800 GeV (the nominal cut value is 1200 GeV) as for the tight SR in the existing 1τ analysis. The dominating systematic uncertainties are the generator uncertainties, JES, TES and ST res (which is the resolution of E_T^{miss}), as expected. The systematic uncertainties presented here are comparable to the uncertainties presented for the tight SR in the 1τ analysis in Table 29 of Ref. [1].

With the systematic uncertainties for all backgrounds at hand an attempt to estimate scale factors has been made. Following the method described briefly in Section 7.4, and in depth in Section 5.2 in Ref. [1], the scale factors listed in Table 7.10 are obtained. The uncertainties, especially the systematic uncertainty

Systematic	Total	QCD	W+jets (true)	W+jets (fake)	Top (true)	Top (fake)	Z+jets (true)	Z+jets (fake)	di-boson
JES up	-0.011	-0.203	-0.023	0.14	0.112	0.082	0.062	0.052	0.013
JES down	-0.046	-0.071	-0.067	0.052	-0.153	0.199	0.049	-0.044	-0.294
JER	-0.063	-0.1406	-0.085	0.122	-0.153	0.062	-0.103	-0.018	0.273
TES up	-0.258	-0.055	0.007	0.21	0.22	-3.471	-0.041	0.223	0
TES down	0.052	0.2638	-0.073	-0.031	-0.06	0.179	0.031	0.002	-0.294
TauId up	0.023	0.0177	0.003	-0.015	0.004	0.214	-0.001	-0.015	0.032
TauId down	-0.005	-0.0177	-0.003	0.002	-0.008	0.022	0.002	0.002	-0.032
TauElV up	0.004	-0.0041	-0.002	-0.018	-0.007	0.096	-0.002	-0.009	0.004
TauElV down	0.011	0.004	0.002	0.001	-0.001	0.111	0.002	-0.009	-0.004
ST up	0.011	-0.049	0.032	0.051	-0.051	0.215	0.034	0.04	-0.294
ST down	0.068	0.0703	0.041	0.073	-0.034	0.308	-0.032	0.089	0
ST res	0.088	-0.018	0.043	0.052	-0.09	0.957	-0.045	0.032	0
JVF up	0.031	0.001	0.041	0.068	-0.049	0.15	0.041	0.058	0
JVF down	0.034	-0.0002	0.046	0.079	-0.035	0.121	0.046	0.079	0
Pileup up	0.04	0.0304	0.1	0.086	-0.032	-0.055	0.021	0.106	-0.075
Pileup down	0.016	-0.028	-0.017	0.113	-0.023	0.073	0.057	0.081	0.066
BJet up	0.042	0	0.034	0.074	0.073	0.053	0.034	0.074	0
BJet down	0.043	0	0.036	0.065	0.031	0.153	0.036	0.065	0
CJet up	0.012	0	0.05	0.095	-0.102	-0.046	0.05	0.095	0
CJet down	0.032	0	0.038	0.08	0.002	0.048	0.038	0.08	0
B Mistag up	0.267	0	0.067	-0.346	-0.224	3.855	0.067	-0.346	0
B Mistag down	0.070	0	0.054	0.013	-0.182	0.886	0.054	0.013	0
top generator	-0.177	-0.2289	-0.005	0.003	-0.951	0.389	-0.005	0.003	0
W,Z generator	0.331	-0.107	0.248	1.489	0.517	-0.938	0	1.334	0
Method QCD	0.257	1	0	0	0	0	0	0	0
topgen stat1	0.0053	0	0	0	0.032	0	0	0	0
topgen stat2	0.037	0	0	0	0	0.391	0	0	0
W,Z gen stat1	0.081	0	0.373	0	0	0	0	0	0
W,Z gen stat2	0.054	0	0	0.668	0	0	0	0	0
W,Z gen stat3	0.026	0	0	0	0	0	1	0	0
W,Z gen stat4	0.12	0	0	0	0	0	0	0.847	0
Diboson gen	-0.003	0	-0.001	-0.008	0.004	0.008	-0.001	-0.008	-0.112
Dibos gen stat	0.007	0	0	0	0	0	0	0	0.331
Total	0.556	1.085	0.48	1.671	1.153	3.423	1.016	1.608	0.561

Table 7.8: Overview of all systematic uncertainties new signal region. The acronyms are introduced in Section 6.1 of Ref. [1]), and some are explained in Section 7.5 of this thesis. The uncertainties are presented in relative variations of the predicted number of background events. The grouping of several background types in one row for the "gen MC stat" sources is only for displaying purposes, in the analysis they are treated as uncorrelated sources.

on ω_W^{fake}, are unreasonably big. In the calculation of the systematic uncertainty on ω_W^{fake}, syst_W^{fake}, a problem occurred and the method optimised for the standard

selection did not converge. This is most likely due to low statistics for events with fake taus in the new SR. The calculation of scale factors is known to struggle with low statistics.

Scale factor	value±stat±syst
ω_W^{true}	$1.11 \pm 0.16 \pm 0.58$
ω_W^{fake}	$0.59 \pm 2.85 \pm \text{syst}_W^{fake}$
ω_{top}^{true}	$0.92 \pm 1.86 \pm 0.52$
ω_{top}^{fake}	$1.12 \pm 63.69 \pm 3.75$

Table 7.9: Scale factors for W + jets, Z + jets and top background contributions created for the analysis in this thesis. Errors are statistical (first) and systematic (second) with all experimental systematic uncertainties included. In the calculation of the systematic uncertainty on ω_W^{fake}, syst_W^{fake}, a problem occurred and the method optimised for the standard selection did not converge.

Uncertainties not considered, the scale factors in Table 7.9 are close to the scale factors estimated in the 1τ analysis. These old scale factors are presented in Table 7.10, and are used for the remainder of this analysis.

Scale factor	value±stat±syst
ω_W^{true}	$1.09 \pm 0.03 \pm 0.11$
ω_W^{fake}	$0.60 \pm 0.18 \pm 0.11$
ω_{top}^{true}	$0.93 \pm 0.05 \pm 0.10$
ω_{top}^{fake}	$0.98 \pm 0.52 \pm 0.34$

Table 7.10: Scale factors for W + jets, Z + jets and top background contributions from the 1τ analysis. Errors are statistical (first) and systematic (second) with all experimental systematic uncertainties included. Number are taken from ref. [1].

Table 7.11 shows the predicted background, corrected for the scale factors in Table 7.10 in a detailed break-down of the sources of background contribution. The QCD background events in the SR come from MC predictions, and should be replaced by the data-driven estimate from the ABCD method, described briefly in Section 7.4.2, or estimation from the "Jet smearing" technique mentioned in the same section. This would most likely increase the number of multijet events.

After cut	Top	W+jets	Z+jets	Di-boson	QCD
1 τ & no other lepton	3669±284.9	11944±353.7	1149±129	52.6±1.96	255±53.3
$\Delta\phi\left(\text{jet}_{1,2}, p_T^{\text{miss}}\right) > 0.4$	2378±211.6	6971±220.5	591±106.8	36.6±1.61	24±17.5
$E_T^{\text{miss}} > 300GeV$	110±10.5	477±15.3	40±10.1	4.26±0.518	0.14±0.08
$m_T^{\tau} > 140$GeV	16.8±6.28	28.4±5.09	26.2±7.76	1.62±0.306	0.13±0.08
$H_T > 1200$GeV	0.33±0.112	0.4±0.14	0.227±0.080	0.028±0.028	0.097±0.074

Table 7.11: Number of expected background events new SR. Uncertainties on the number of expected events are statistical.

Table 7.12 summarises the number of observed events in the new SR in data and the number of expected background events. The table also shows number of events for the two mSUGRA benchmark points: m_0 = 400 GeV / $m_{1/2}$ = 800 GeV and m_0 = 600 GeV / $m_{1/2}$ = 850 GeV.

-	1τ new SR
Multijet	$0.097 \pm 0.074 \pm 0.054$
W + jets	$0.40 \pm 0.14 \pm 0.70$
Z + jets	$0.227 \pm 0.0804 \pm 0.368$
Top	$0.33 \pm 0.12 \pm 0.71$
Diboson	$0.028 \pm 0.028 \pm 0.160$
Total background	$1.08 \pm 0.212 \pm 1.147$
Data	3
mSUGRA 400/800	1.0
mSUGRA 600/850	0.6

Table 7.12: Number of expected background events and data yield in the new SR. Uncertainties on the number of expected events are separated into statistical (first) and systematic (second) components. The SM prediction is computed taking into account correlations between the different uncertainties. Also shown are the number of expected signal events for the two benchmark point for the mSUGRA signal model studied, m_0 = 400 GeV / $m_{1/2}$ = 800 GeV and m_0 = 600 GeV / $m_{1/2}$ = 850 GeV.

The number of expected background events and data yields in the loose and tight SR of the 1τ analysis are presented in Table 7.13 for comparison. The

number of data events in the new SR is the same as for the tight SR. The hard cut on H_T reduces the number of background events in the new SR so that the number of background events is smaller than the corresponding numbers in the tight SR.

-	1τ loose	1τ tight
Multijet	$1.12 \pm 0.49^{+1.27}_{-1.12}$	$0.23 \pm 0.10 \pm 0.24$
W + jets	$3.13 \pm 0.57 \pm .58$	$0.73 \pm 0.20 \pm 0.69$
Z + jets	$1.89 \pm 0.56 \pm 1.58$	$0.42 \pm 0.15 \pm 0.14$
Top	$3.87 \pm 0.99 \pm 1.62$	$0.82 \pm 0.34 \pm 0.46$
Diboson	$0.47 \pm 0.18 \pm 0.16$	$0.16 \pm 0.10 \pm 0.09$
Total background	$10.5 \pm 1.4 \pm 2.6$	$2.4 \pm 0.4 \pm 0.8$
Data	12	3

Table 7.13: Number of expected background events and data yields in the 1τ SRs. Uncertainties on the number of expected events are separated into statistical (first) and systematic (second) components. The SM prediction is computed taking into account correlations between the different uncertainties. The numbers are taken from Table 6 in Ref. [37]

A limit at 95% confidence level (CL) on m_0 and $m_{1/2}$ for the new SR in the mSUGRA model is derived using CLs prescription [114]. The CL is an approximate confidence in the background-only hypothesis, briefly discussed in Section 7.7.1. When setting limits, the model with $s + b$ plays the role of H_0, which is tested against the background-only hypothesis, H_1, with $s = 0$. The profile likelihood ratio is used as a test statistic [115] and all systematic uncertainties on the background estimate are treated as nuisance parameters[1] Any possible signal contamination in the control regions is neglected. The limit is computed in an asymptotic approximation, explained in Ref. [115].

The expected and observed 95% CL exclusion limits on the mSUGRA model parameters in the new SR are shown in Figure 7.20. Values of $m_{1/2}$ up to 640 GeV are excluded for low m_0 and 300 GeV for high m_0 (2000 GeV $< m_0 <$ 5400 GeV). For comparison, Figure 7.21a and Figure 7.21b show the limits in the loose and tight SRs in the 1τ analysis in Ref. [1], respectively.

[1]A nuisance parameter is any parameter which is not of immediate interest but which must be accounted for in the analysis of those parameters which are of interest.

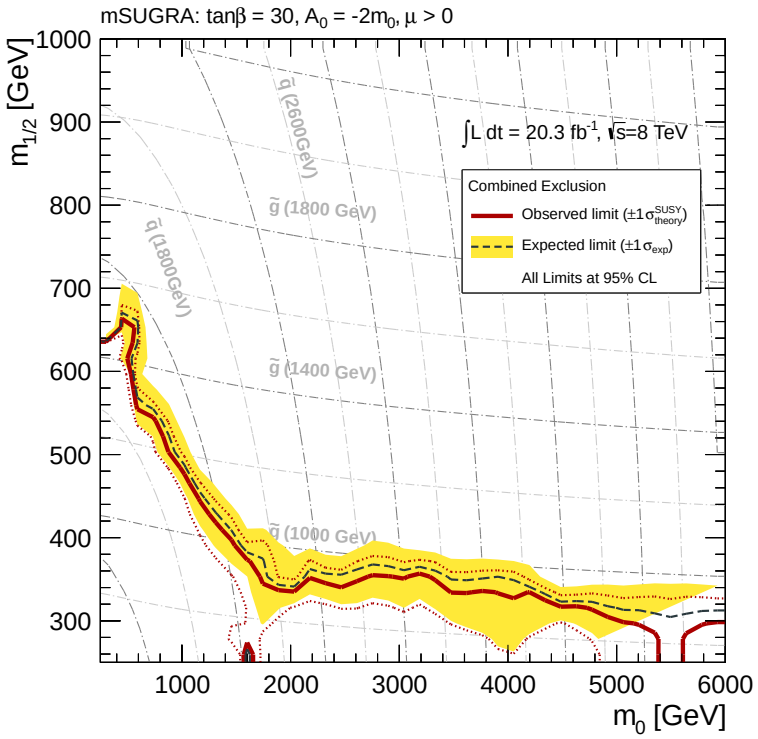

Figure 7.20: Expected and observed 95% CL exclusion limits on the mSUGRA model parameters in the new SR, summarised in Table 7.7. The dashed lines show the expected limits at 95%CL, with the yellow bands indicating the 1σ excursions due to experimental and background-theory uncertainties. Observed limits are indicated by red curves, where the solid contour represents the nominal limit, and dotted lines represent uncertainties.

The new limit in Figure 7.20excludes a region of the $(m_0, m_{1/2})$ mass plane comparable to the tight SR exclusion in Figure 7.21b for low m_0. It compares to the combined limit for the 1τ, τ + e and $\tau + \mu$ channels in Ref. [1], shown in the introduction of this chapter in Figure 7.1a.

One surprising feature of the new exclusion limit is that the exclusion for high m_0 and low $m_{1/2}$ is better than the combined result for the 1τ, τ + e and $\tau + \mu$. The optimisation presented in this thesis has been focussed on improving sensitivity in the low m_0 and high $m_{1/2}$ region, and up until the point where the full analysis was run on all mSUGRA signal points in Table 7.1 there was no way of knowing what was happening for high m_0. The new limit is still, however, far away from the limit in Figure7.1b, for the jet analysis in Ref. [2].

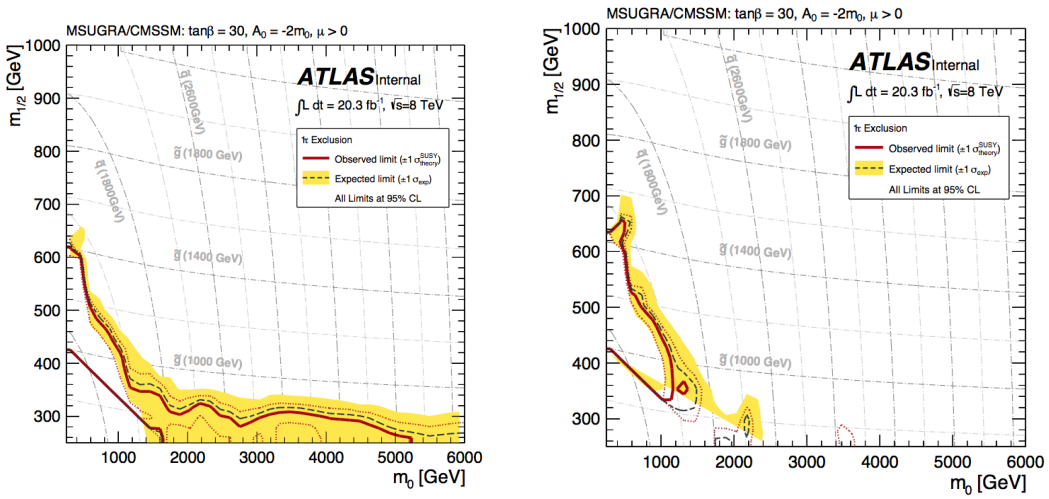

(a) Loose SR

(b) Tight SR

Figure 7.21: Expected and observed limits for the mSUGRA grid in both signal regions; loose (left) and tight (right) in in the 1τchannel. The signal regions are summarised in defined in Table 7.2. Images are taken from Ref. [1].

Chapter 8

Summary and conclusions

The main topic of this thesis as been the optimisation of the search for supersymmetric particles in $\sqrt{s} = 8$ TeV proton-proton collsisions in final events with one τ lepton, jets and missing transverse energy in the low m_0 and high $m_{1/2}$ region of the $(m_0, m_{1/2})$ mass plane.

The first part of the thesis provided a short introduction to the theorietical framework on which this work is built: the SM and SUSY. Chapter 2 presented the theoretical foundation of the SM, and mentioned both the successes and problems of the theory. The concept of SUSY and its solutions to some of the unsolved problems of the SM were described in Chapter 3.

The next part of the thesis describes the experimental set-up and tools necessary to perform the analysis. The real data investigated in this thesis was taken by the ATLAS detector between April and December 2012, as part of run 1 of the LHC. The LHC is now in shut-down, with preparations being made for run2. The ATLAS experiment and its subdetectors were presented in Chapter 4, and the reconstruction of physics objects in the detector was explained. As the final state of interest in this study contains a tau lepton, the reconstruction and identification of taus in ATLAS was presented, more exstensively than reconstruction and identification of the other physics objects, in Chapter 5. The optimisation presented in this thesis is performed on MC simulated data. Chapter 6 gives an introduction to MC event generators and detector simulation tools. This chapter also presents a comparison of AFII with full Geant 4 simulation for eight points in the mSUGRA signal grid. All comparisons show good agreement between fastsim and fullsim on the level of statistical uncertainties. Two correcions recommended by the Tau working group were shown to have no significant effect on the shape agreemen, and to even worsen the agreement between the samples with fast and full simulation slightly. The full mSUGRA signal grid was not reproduced with AFII detector simulation, but hte result of this study is promising for signal grid production for run 2. Further studies would be required for the new center of

mass energy, luminosity and collider and detector upgrade.

Chapter 7 presented the optimisation of an analysis searching for SUSY in events with one tau lepton. Four strategies aiming to increase the Asimov significance were presented in a simplified version of the analysis in Ref. [1]. The Asimov significance was plotted as a function of H_T in order to investigate whether a new cut on this kinematic variable could improve sensitivity in the low m_0 and high $m_{1/2}$ region of the $(m_0, m_{1/2})$ mass plane. The tau definition was changed from medium to loose, and the Asimov significance was again plotted as a function of H_T. The cut on the p_T of the tau was lowered from 30 GeV to 20 GeV, and Asimov significance was plotted as a function of H_T. The higher limits in the $(m_0, m_{1/2})$ mass plane from the analysis with no tau requirement in Ref. [2] compared to the analysis requiring one tau in Ref. [1] inspired a closer look into the former analysis' signal region definitions. The analysis operates with five inclusive analysis channels characterised by increasing jet number from two to six. This motivated a study of the Asimov significance as a function of number of jets.

On the basis of the optimisation, a new signal region was constructed. Selecting events with $H_T > 1200$ GeV, $E_T^{\text{miss}} > 300$ GeV and using the loose tau definition is seen to have a small increasing effect on the Asimov significance. The full analysis is then run within the new signal region. There is very limited statistics in the signal region after the high cut on H_T, and so scale factors for background estimation were taken from Ref. [1]. The expected and observed 95% CL exclusion limits on the mSUGRA model parameters in the new signal region were calculated, seeFigure 7.20. Values of $m_{1/2}$ up to 640 GeV are excluded for low m_0 and 300 GeV for high m_0 (2000 GeV $< m_0 <$ 5400 GeV). The new limit excludes a region of the $(m_0, m_{1/2})$ mass plane comparable to the tight SR exclusion for the 1τ analysis, shown in Figure 7.21b, for low m_0. There is no improvement. The limit also compares to the combined limit for the 1τ, τ + e and $\tau + \mu$ channels in Ref. [1], shown in Figure 7.1a.

Improvements to studies for optimisation in the future would include removing the tau veto. A more detailed look into the tau ID requirements could also be investigated. Optimising for all SM backgrounds should also be considered. Run 2 of the LHC will give a quantum leap in luminosity and collision energy. This means there will be more pile-up, but it also means we have the possibility to reach even higher masses. The new run conditions will require new optimisation for all SUSY (and other) searches. Maybe 2015 is the year we find a supersymmetric particle?

Bibliography

[1] The ATLAS Collaboration. "Search for supersymmetry in 8 tev p–p collisions with τ-leptons, jets and missing transverse energy in the final state". *ATL-COM-PHYS-2013-1086*, 2013.

[2] The ATLAS Collaboration. "Search for squarks and gluinos with the ATLAS detector in final states with jets and missing transverse momentum and 20.3 fb^{-1} of $\sqrt{s} = 8$ tev proton-proton collisions data: supporting documentation". *ATLAS-CONF-2013-047*, 2013.

[3] J. Beringer et al. (Particle Data Group). Phys. Rev. D**86** (2012) 01000. `pdg.lbl.gov`.

[4] Hinshaw et al. Nine-year wilkinson microwave anisotropy probe (wmap) observations: cosmological parameter results. *The Astrophysical Journal Supplement Series*, 208(2):19, 2013.

[5] P.A.R. et al Ade. Planck 2013 results. xvi. cosmological parameters. *arXiv preprint arXiv:1303.5076*, 2013.

[6] Harvard CMB Group. "BICEP2". `http://www.cfa.harvard.edu/CMB/bicep2/`, March 2014.

[7] BICEP2 collaboration. "BICEP2 i: Detection of B-mode polarization at Degree Angular Scales". *arXiv:1403.3985 [astro-ph.CO]*, 2014.

[8] Joseph John Thomson. Xl. cathode rays. *The London, Edinburgh, and Dublin Philosophical Magazine and Journal of Science*, 44(269):293–316, 1897.

[9] Ernest Rutherford. Lxxix. the scattering of α and β particles by matter and the structure of the atom. *The London, Edinburgh, and Dublin Philosophical Magazine and Journal of Science*, 21(125):669–688, 1911.

[10] James Chadwick. The existence of a neutron. *Proceedings of the Royal Society of London. Series A*, 136(830):692–708, 1932.

[11] Max Planck. The theory of heat radiation. *Entropie*, 144(190):164, 1900.

[12] Albert Einstein. On a heuristic point of view about the creation and conversion of light. *Annalen der Physik*, 17:132–148, 1905.

[13] Arthur H Compton. Xcv. absorption measurements of the change of wavelength accompanying the scattering of x-rays. *The London, Edinburgh, and Dublin Philosophical Magazine and Journal of Science*, 46(275):897–911, 1923.

[14] Louis De Broglie. *Recherches sur la théorie des quanta*. PhD thesis, Migration-université en cours d'affectation, 1924.

[15] Claus Jönsson. Elektroneninterferenzen an mehreren künstlich hergestellten feinspalten. *Zeitschrift für Physik*, 161(4):454–474, 1961.

[16] F. Reines et al C.L. Cowan, Jr. Detection of the free neutrino: a confirmation. *Science*, 24(3212):103–104, 1956.

[17] Paul AM Dirac. The quantum theory of the electron. *Proceedings of the Royal Society of London. Series A, Containing Papers of a Mathematical and Physical Character*, pages 610–624, 1928.

[18] Carl D Anderson. The positive electron. *Physical Review*, 43(6):491, 1933.

[19] E. Noether. Invariante variationsprobleme. *Nachrichten von der Gesellschaft der Wissenschaften zu Göttingen, Mathematisch-Physikalische Klasse*, 1918:235–257, 1918.

[20] F. Mandl and G. Shaw. *"Quantum Field theory"*. Wiley, second edition, 2011.

[21] H. Baer and X. Tata. *"Weak Scale Supersymmetry, From Superfields to Scattering Events"*. Cambridge University Press, 2006.

[22] D. Griffiths. *"Introduction to Elementary Particles"*. WILEY-VCH Verlag GmbH & Co. KGaA, Weinheim, second, revised edition, 2011.

[23] A. Pitch. The standard model of electroweak interactions. *arXiv preprint arXiv:1201.0537*, 2012.

[24] Makoto Kobayashi and Toshihide Maskawa. Cp-violation in the renormalizable theory of weak interaction. *Progress of Theoretical Physics*, 49(2):652–657, 1973.

[25] Nicola Cabibbo. Unitary symmetry and leptonic decays. *Phys. Rev. Letters*, 10, 1963.

[26] PHD Comics. the higgs boson explained. `http://www.phdcomics.com/comics/archive.php?comicid=1489`, June 2014.

[27] `http://www.exploratorium.edu/origins/cern/ideas/cartoon.html`, June 2014.

[28] Peter W. Higgs. Broken symmetries and the masses of gauge bosons. *Phys. Rev. Lett.*, 13:508–509, Oct 1964.

[29] F. Englert and R. Brout. Broken symmetry and the mass of gauge vector mesons. *Phys. Rev. Lett.*, 13:321–323, Aug 1964.

[30] J. Goldstone. Field theories with "superconductor" solutions. *Il Nuovo Cimento*, 19(1):154–164, 1961.

[31] Combined measurements of the mass and signal strength of the Higgs-like boson with the ATLAS detector using up to 25 fb^{-1} of proton-proton collision data. Technical Report ATLAS-CONF-2013-014, CERN, Geneva, Mar 2013.

[32] Stephen P. Martin. "A Supersymmetry Primer". *arXiv:hep-ph/9709356*, 2011.

[33] Rudolf Haag, Jan T. Łopuszański, and Martin Sohnius. All possible generators of supersymmetries of the s-matrix. *Nuclear Physics B*, 88(2):257 – 274, 1975.

[34] Sidney Coleman and Jeffrey Mandula. All possible symmetries of the s matrix. *Phys. Rev.*, 159:1251–1256, Jul 1967.

[35] B. de Carlos and J.A. Casas. One loop analysis of the electroweak breaking in supersymmetric models and the fine tuning problem. *Phys.Lett.*, B309:320–328, 1993.

[36] John R. Ellis, Toby Falk, Keith A. Olive, and Mark Srednicki. Calculations of neutralino-stau coannihilation channels and the cosmologically relevant region of MSSM parameter space. *Astropart.Phys.*, 13:181–213, 2000.

[37] ATLAS Collaboration. Search for supersymmetry in events with large missing transverse momentum, jets, and at least one tau lepton in 20 fb^{-1} of

sqrt(s)=8 TeV proton-proton collision data with the ATLAS detector: Paper draft to prepare and follow up with the official circulations of SUSY-2013-10 in ATLAS. Technical Report ATL-COM-PHYS-2014-402, CERN, Geneva, Apr 2014.

[38] "About CERN". `http://home.web.cern.ch/about`, April 2014.

[39] "Member States". `http://home.web.cern.ch/about/member-states`, April 2014.

[40] T. Massam et al. "Experimental observation of antideuteron production". *Il Nuovo Cimento A*, 63:10–14, September 1965.

[41] D. E. Dorfan et al. "Observation of Antideuterons". *Phys.Rev.Lett.*, 14:1003–1006, June 1965.

[42] L. Iconomidou-Fayard. "Results on Cp Violation from the NA48 Experiment at CERN". *International Journal of Modern Physics A*, pages 1–14, 2002.

[43] The nobel prize in physics 2013. `http://www.nobelprize.org/nobel_prizes/physics/laureates/2013/`, May 2014.

[44] Roel Aaij, B Adeva, M Adinolfi, and Affolderothers. Observation of the resonant character of the $Z(4430)^-$ state. *arXiv preprint arXiv:1404.1903*, 2014.

[45] Oliver Sim Brüning, Paul Collier, P Lebrun, Stephen Myers, Ranko Ostojic, John Poole, and Paul Proudlock. LHC Design Report, Vol. 1. Technical report, CERN, 2004.

[46] Oliver Sim Brüning, Paul Collier, P Lebrun, Stephen Myers, Ranko Ostojic, John Poole, and Paul Proudlock. LHC Design Report, Vol. 2. Technical report, CERN, 2004.

[47] V Mertens, Karlheinz Schindl, Paul Collier, Michael Benedikt, and John Poole. LHC design report, Vol. 3. Technical report, CERN, 2004.

[48] "CERN's Accelerator Complex". `https://espace.cern.ch/liu-project/LIU_images/Forms/DispForm.aspx?ID=11`, April 2014.

[49] E. M. Henley and A. García. *"Subatomic Physics"*. World Scientific Publishing Co. Pte. Ltd., third edition, 2007.

[50] Daniel Teyssier on behalf of the ATLAS and CMS collaborations. "LHC results and prospects: Beyond Standard Model". *arxiv:1404.7311v1*, 2014.

[51] Lucio Rossi and Agnes Szeberenyi. HiLumi LHC design study moves towards HL-LHC. Jan 2014.

[52] "Atlas Gold display". `http://www.atlas.ch/photos/full-detector-cgi.html`, May 2014.

[53] "Inner Detector 3D". `http://www.atlas.ch/photos/inner-detector-combined.html`, May 2014.

[54] "Calorimeters". `http://www.atlas.ch/photos/calorimeters.html`, May 2014.

[55] "Combined Muon System". `http://www.atlas.ch/photos/muons-combined.html`, May 2014.

[56] *ATLAS inner detector: Technical Design Report, 1.* Technical Design Report ATLAS. CERN, Geneva, 1997.

[57] *ATLAS central solenoid: Technical Design Report.* Technical Design Report ATLAS. CERN, Geneva, 1997. Electronic version not available.

[58] *ATLAS inner detector: Technical Design Report, 2.* Technical Design Report ATLAS. CERN, Geneva, 1997.

[59] Norbert Wermes and G Hallewel. *ATLAS pixel detector: Technical Design Report.* Technical Design Report ATLAS. CERN, Geneva, 1998.

[60] P Dervan and Taka Kondo. Performance and operation experience of the atlas semiconductor tracker. Technical report, ATL-COM-INDET-2013-044, 2013.

[61] J Adelman. Performance of the atlas transition radiation tracker. *Nuclear Instruments and Methods in Physics Research Section A: Accelerators, Spectrometers, Detectors and Associated Equipment*, 706:33–38, 2013.

[62] E. Abat et al. The atlas transition radiation tracker (trt) proportional drift tube: design and performance. *Journal of Instrumentation*, 3(02):P02013, 2008.

[63] T. Nattermann. *"Search for Supersymmetry with Tau Leptons, Muons, Missing Transverse Momentum and Jets with the ATLAS Experiment at the Large Hadron Collider"*. PhD thesis, Rheinischen Friedrich-Wilhelms-Universitat Bonn, 2013.

[64] Akira Yamamoto, Y Makida, R Ruber, Y Doi, T Haruyama, F Haug, H Ten Kate, M Kawai, T Kondo, Y Kondo, et al. The atlas central solenoid. *Nuclear Instruments and Methods in Physics Research Section A: Accelerators, Spectrometers, Detectors and Associated Equipment*, 584(1):53–74, 2008.

[65] ATLAS Collaboration. *ATLAS liquid-argon calorimeter: Technical Design Report*. Technical Design Report ATLAS. CERN, Geneva, 1996.

[66] ATLAS Collaboration. *ATLAS tile calorimeter: Technical Design Report*. Technical Design Report ATLAS. CERN, Geneva, 1996.

[67] Georges Aad, E Abat, J Abdallah, AA Abdelalim, A Abdesselam, O Abdinov, BA Abi, M Abolins, H Abramowicz, E Acerbi, et al. The atlas experiment at the cern large hadron collider. *Journal of Instrumentation*, 3(08):S08003, 2008.

[68] Giora Mikenberg. The atlas muon spectrometer. *Modern Physics Letters A*, 25(09):649–667, 2010.

[69] Georges Aad et al. Performance of the ATLAS Trigger System in 2010. *Eur.Phys.J.*, C72:1849, 2012.

[70] ATLAS Collaboration. Electron reconstruction and identification efficiency measurements with the ATLAS detector using the 2011 LHC proton–proton collision data. *submitted to Eur. Phys. J.*, 2014.

[71] W Lampl, S Laplace, D Lelas, P Loch, H Ma, S Menke, S Rajagopalan, D Rousseau, S Snyder, and G Unal. Calorimeter Clustering Algorithms: Description and Performance. Technical Report ATL-LARG-PUB-2008-002. ATL-COM-LARG-2008-003, CERN, Geneva, Apr 2008.

[72] ATLAS Collaboration. Measurements of the photon identification efficiency with the ATLAS detector using 4.9 fb-1 of pp collision data collected in 2011. Technical Report ATLAS-CONF-2012-123, CERN, Geneva, Aug 2012.

[73] ATLAS Collaboration. Expected photon performance in the ATLAS experiment. Technical Report ATL-PHYS-PUB-2011-007, CERN, Geneva, Apr 2011.

[74] ATLAS Collaboration. Muon reconstruction efficiency and momentum resolution of the ATLAS experiment in proton-proton collisions at $\sqrt{s} = 7\,\text{TeV}$ in 2010. *submitted to Eur. Phys. J.*, 2014.

[75] L. Asquith et. al. Performance of Jet Algorithms in the ATLAS Detector. Technical Report ATL-PHYS-INT-2010-129, CERN, Geneva, Dec 2010.

[76] Letter of Intent for the Phase-I Upgrade of the ATLAS Experiment. Technical Report CERN-LHCC-2011-012. LHCC-I-020, CERN, Geneva, Nov 2011.

[77] The ATLAS Collaboration. "Identification of Hadronic Decays of Tau Leptons in 2012 Data with the ATLAS Detector". *ATLAS-CONF-2013-064*, 2013.

[78] B. P. Roe et al. "Boosted decision trees, an alternative to artificial neural networks". *arXiv: physics/0408124*, 2004.

[79] Tmva. `http://tmva.sourceforge.net`, June 2014.

[80] T. Sjöstrand. "Monte Carlo Generators". *arXiv:hep-ph/0611247v1*, 2006.

[81] "Herwig++ Physics and Manual". *arXiv:0803.0883v3*, 2008.

[82] S. Mrenna T. Sjöstrand and P. Skands. "A Brief Introduction to PYTHIA 8.1". *arXiv:0710.3820v1*, 2007.

[83] Sherpa. `https://sherpa.hepforge.org/trac/wiki`, May 2014.

[84] The powheg box. `http://powhegbox.mib.infn.it`, May 2014.

[85] Bryan Webber. Monte carlo methods in particle physics. `http://www.hep.phy.cam.ac.uk/theory/webber/MunichPDF/MClecture4.pdf`, June 2014.

[86] The mc@nlo package. `http://www.hep.phy.cam.ac.uk/theory/webber/MCatNLO/`, May 2014.

[87] Michelangelo L. Mangano, Mauro Moretti, Fulvio Piccinini, Roberto Pittau, and Antonio D. Polosa. ALPGEN, a generator for hard multiparton processes in hadronic collisions. *JHEP*, 0307:001, 2003.

[88] P. Gondolo, J. Edsjo, P. Ullio, L. Bergstrom, Mia Schelke, et al. DarkSUSY: Computing supersymmetric dark matter properties numerically. *JCAP*, 0407:008, 2004.

[89] Isajet 7.83. `http://www.nhn.ou.edu/~isajet/`, May 2014.

[90] S et. al. Agostinelli. GEANT4: A Simulation toolkit. *Nucl. Instrum. Methods Phys. Res., A*, 506(CERN-IT-2002-003. SLAC-PUB-9350. 3):250–303. 86 p, Jul 2002.

[91] W Lukas. Fast Simulation for ATLAS: Atlfast-II and ISF. Technical Report ATL-SOFT-PROC-2012-065, CERN, Geneva, Jun 2012.

[92] Jtc1/sc22/wg21 - the c++ standards committee. `http://www.open-std.org/jtc1/sc22/wg21/`, May 2014.

[93] A brief description - c++ information. `http://www.cplusplus.com/info/description/`, May 2014.

[94] Python. `https://www.python.org`, May 2014.

[95] et. al. Rene Brun, Fons Rademakers. Root user's guide. `http://root.cern.ch/root/html534/guides/users-guide/ROOTUsersGuideA4.pdf`, 2014.

[96] Root. `http://root.cern.ch/`, May 2014.

[97] Wim Lavrijsen Pere Mato. Pyroot. `http://root.cern.ch/drupal/content/pyroot`, May 2014.

[98] Borut Paul Kersevan and Elzbieta Richter-Was. The Monte Carlo event generator AcerMC versions 2.0 to 3.8 with interfaces to PYTHIA 6.4, HERWIG 6.5 and ARIADNE 4.1. *Comput.Phys.Commun.*, 184:919–985, 2013.

[99] The ATLAS Collaboration. A framework for vertex reconstruction in the atlas experiment at lhc. *Journal of Physics: Conference Series*, 219(3):032019, 2010.

[100] T. Sjursen. *"Search for Supersymmetry with Tau Leptons in Data from the ATLAS Experiment at the LHC"*. PhD thesis, The University of Bergen, 2014.

[101] B.C. Allanach. SOFTSUSY: a program for calculating supersymmetric spectra. *Comput.Phys.Commun.*, 143:305–331, 2002.

[102] Pavel M. Nadolsky, Hung-Liang Lai, Qing-Hong Cao, Joey Huston, Jon Pumplin, et al. Implications of CTEQ global analysis for collider observables. *Phys.Rev.*, D78:013004, 2008.

[103] A.D. Martin, W.J. Stirling, R.S. Thorne, and G. Watt. Parton distributions for the LHC. *Eur.Phys.J.*, C63:189–285, 2009.

[104] W. Beenakker, R. Hopker, M. Spira, and P.M. Zerwas. Squark and gluino production at hadron colliders. *Nucl.Phys.*, B492:51–103, 1997.

[105] A. Kulesza and L. Motyka. Threshold resummation for squark-antisquark and gluino-pair production at the LHC. *Phys.Rev.Lett.*, 102:111802, 2009.

[106] Wim Beenakker, Silja Brensing, Michael Kramer, Anna Kulesza, Eric Laenen, et al. Soft-gluon resummation for squark and gluino hadroproduction. *JHEP*, 0912:041, 2009.

[107] Michael Kramer, Anna Kulesza, Robin van der Leeuw, Michelangelo Mangano, Sanjay Padhi, et al. Supersymmetry production cross sections in pp collisions at $\sqrt{s} = 7$ TeV. 2012.

[108] Georges Aad et al. Search for squarks and gluinos with the ATLAS detector in final states with jets and missing transverse momentum using 4.7 fb^{-1} of $\sqrt{s} = 7$ TeV proton-proton collision data. *Phys.Rev.*, D87:012008, 2013.

[109] ATLAS Collaboration. Jet energy measurement and its systematic uncertainty in proton–proton collisions at $\sqrt{s} = 7$ TeV with the ATLAS detector. 2014.

[110] ATLAS Collaboration. Determination of the tau energy scale and the associated systematic uncertainty in proton-proton collisions at $\sqrt{s} = 8$ TeV with the ATLAS detector at the LHC in 2012. (ATLAS-CONF-2013-044), Apr 2013.

[111] Glen Cowan, Kyle Cranmer, Eilam Gross, and Ofer Vitells. Asymptotic formulae for likelihood-based tests of new physics. *The European Physical Journal C*, 71(2):1–19, 2011.

[112] Glen Cowan. Expected discovery significance for counting experiment with background uncertainty. `http://www.pp.rhul.ac.uk/~cowan/atlas/cowan_statforum_8may12.pdf`, 2012.

[113] Georges Aad et al. Search for Supersymmetry in Events with Large Missing Transverse Momentum, Jets, and at Least One Tau Lepton in 7 TeV Proton-Proton Collision Data with the ATLAS Detector. *Eur.Phys.J.*, C72:2215, 2012.

[114] A. L. Read. Presentation of search results: the cl_s technique. *J. Phys. G: Nucl. Part. Phys. 28 2693*, 2002.

[115] Glen Cowan, Kyle Cranmer, Eilam Gross, and Ofer Vitells. Asymptotic formulae for likelihood-based tests of new physics. *The European Physical Journal C*, 71(2), 2011.

Appendices

Appendix A

Summer Student Report, CERN 2013

Summer student project 13363

Studies for the charge asymmetry measurement in top quark pair production in pp collisions at $\sqrt{s} = 8$ TeV using the ATLAS detector

Author:
Agnethe Seim Olsen

Supervisors:
Dr. Umberto De Sanctis
Dr. Richard Hawkings

1 Introduction

The charge asymmetry A_C, predicted by QCD at NLO in the top-antitop quarks pair production, is an important test of the SM predictions at high energies, but is also very sensitive to New Physics. The asymmetry could be altered by the presence of new particles coupling to top quarks, whose effects cannot be seen in the $t\bar{t}$ invariant mass spectrum [1]. At the LHC, top quark pairs are produced mainly through gluon-gluon fusion. About 20% of the events are produced from $q\overline{q}$ hard collisions, while the fraction coming from qg partonic processes is almost negligible. The effect is present only in asymmetric initial states, like $q\overline{q}$ and qg [2]. Quarks are more boosted than antiquarks, due to the different mean momenta carried by valence quarks and sea antiquarks [1]. Hence the variable $\Delta \mid y \mid = \mid y_t \mid - \mid y_{\bar{t}} \mid$, that is the difference between the absolute values of the rapidity of the top and the antitop, is used to define A_C:

$$A_c = \frac{N(\Delta \mid y \mid > 0) - N(\Delta \mid y \mid < 0)}{N(\Delta \mid y \mid > 0) + N(\Delta \mid y \mid < 0)} \tag{1}$$

obtained by counting the number of events where $\Delta \mid y \mid$ is positive or negative [4].

The top quark mainly decays to a W boson and a b-quark, and W+jets is

the largest background in the semileptonic top decay channel.
This report presents a measurement of the top-antitop production A_C, in the semileptonic channel, using data corresponding to an integrated luminosity of 14.3 fb^{-1} of pp collisions at $\sqrt{s}$=8 TeV collected by the ATLAS detector at the LHC.
An estimation of W+jets scale factors (SF) using "data-driven" methods is presented together with a study on the scale factors' dependence on different kinematic variables.

2 Object definition and event selection

The $t\bar{t}$ final state in the lepton + jets channel is characterised by an isolated lepton (electron or muon) with relatively high p_T, missing transverse momentum (E_T^{miss}) arising from the neutrino from the leptonic W decay, two b-quark jets and two light quark jets from the hadronic W decay.
The appropriate single-electron or single-muon trigger is required to have fired, EF_e24vhi_medium1 or EF_e60_medium1 for the electron and EF_mu24i_tight or EF_mu36_tight for the muon [2]. The events are also required to contain exactly one, isolated, reconstructed lepton .
To reject multijet background, E_T^{miss} >20 GeV and $E_T^{miss} + M_T^W$ >60 GeV requirements are applied.
The event is required to have at least four jets, with $\mid \eta \mid$ <2.5 and p_T>25 GeV. These are reconstructed with the $anti-k_t$ jet algorithm with a distance parameter R=0.4. In the signal region at least one b-tagged jet is required using the MV1-tagger (at 70% efficiency). For more details, see Ref. [1].

3 Background determination

The number of background events coming from single top production, Z + jets and diboson events are evaluated using Monte Carlo (MC) simulation normalised to the relevant NNLO cross sections for single top and Z + jets events and NLO for diboson events [1].

The method used for evaluating the QCD background with fake leptons in both the electron and muon channels is the so-called 'Matrix Method' [3]. For W + jets, since both the normalisation and the heavy flavour (HF) composition are not accurately known in MC, a data driven approach is used. The normalisation and flavor scale factors are determined simultaneously. The total W+jets scale factors for each flavour component are the product of the W+jets nomralisation and the flavour specific scale factors [3].

3.1 W + jets normalisation

At the LHC, there is an overall charge asymmetry in the production of W-bosons. Due to the relative differences in the quark and anti-quark parton distribution functions more W^+ than W^- are produced. Theoretically the ratio of cross-sections

$$r_{MC} = \frac{\sigma(pp \to W^+)}{\sigma(pp \to W^-)} \tag{2}$$

is better understood than the prediction of the total W cross-sections. This asymmetry is exploited to measure the total W + jets background from data. To a good approximation, processes other than W + jets give equal numbers of positively and negatively charged leptons, except for single top, dibosons and Z + jets production[1]. The normalisation of the W+jets background (before the b-tagging requirement is applied) in the signal region ($\geq$ 4 jets) is extracted from the following formula:

$$N_{W^+} + N_{W^-} = (\frac{r_{MC}+1}{r_{MC}-1})(D^+ - D^-) \tag{3}$$

where $D^{+/-}$ is the number of events with positive/ negative lepton in the final state when asymmetric bacgrounds have been subtracted and r_{MC} is evaluated applying signal region kinematic cut to the W+jets MC simulated samples. Since the charge asymmetry depends on the W+jets flavour composition, a data driven procedure is used to estimate the HF fraction [3].

The fraction of W+jets events with at least one b-tag (tagged sample) is estimated in each jet bin (n) using

$$W^n_{\geq 1tag} = W^n_{pretag} * f^{2j}_{tag} * f^{2\to n}_{tag} \tag{4}$$

where W^n_{pretag} is the W + jets normalisation estimated from the charge asymmetry method in the n-th bin, f^{2j}_{tag} is the tagging fraction (the ratio of the tagged and the untagged sample) measured from data in the 2jet exclusive bin (where the W background is dominant), after the subraction of the other asymmetric backgrounds listed above, and $f^{2\to n}_{tag}$ is measured from MC as the ratio between the tagging fractions in the 2-jet exclusive bin and each n jet bin [3].

3.2 W + heavy flavour rescaling

The flavour composition of the W + jets sample can be tuned by applying the scale factors K_{bb}, K_{cc}, K_c and K_{light}, calculated for each flavour (xx) in each jet bin i as the ratio of the flavour fractions F_{bb}, F_{cc}, F_c, F_{light} determined from MC and from a data driven method

$$K_{xx,i} = \frac{F^{data}_{xx,i}}{F^{MC}_{xx,i}} \tag{5}$$

In data, the number of W+jets, N^W, is obtained after subtraction of non-W and QCD contributions: $N^W = N_{data} - N_{QCD} - N_{MC}$.
For each jet bin i the relation between the tagged and pretagged number of events is

$$N^{W,tag}_i = N^{W,pretag}_i * (F_{bb,i}P_{bb,i} + F_{cc,i}P_{cc,i} + F_{c,i}P_{c,i} + F_{light,i}P_{light,i}) \tag{6}$$

where P_{xx},i is the b-tagging probability for each flavour type taken from MC. We let $F_{cc} = K_{cctobb} * F_{bb}$, where K_{cctobb} is taken from MC, to simplify the method, and obtain a single SF for the bb and cc components as these are similar processes [3].

Using the equation above and the fact that for each jet bin the flavour fractions add up to unity, the data is split into sub-samples of negatively and positively charged leptons and the W+jets enriched region is considered to determine $F_{xx,2}$ [3]. The number of W+jets in the pretag 2-jet exclusive bin ($N_2^{W,pretag^{\pm}}$) is already normalised to data using the A_C method. The fractions $F_{xx,2}$ are determined by requiring that the tagged number of events ($N_2^{W,tag^{\pm}}$) in MC equal that in data separately for the two subsamples of leptons. Using the fractions the normalisation is re-determined and the procedure iterated [3].

4 Reconstruction of the $t\bar{t}$ final state

The full $t\bar{t}$ system is reconstructed for measurement of the A_C. A kinematic fit is used to determine the likelihood for candidate events to be $t\bar{t}$ events as well as to compute the four-vectors of the top and antitop quark to compute $\Delta \mid y \mid$ [2].
The likelihood is maximised with respect to the energies of the partons, the energy of the charged lepton, and the components of the neutrino three-momentum. The combination of jets and partons that give the highest likelihood value is selected. Finally, the top quark (or anti-quark) is identified by looking at the lepton charge in the event [1].

5 Results

5.1 W + jets Scale Factor estimates

In a first study, the normalisation SF and HF SF for the W+jets background were estimated in different jet bins; 2 jet exclusive, 3 jet exclusive, 3 jet inclusive, 4 jet exclusive, 4 jet inclusive and 5 jet inclusive, using the data driven method described in section 3.1-3.2. The estimated scale factors with statistical uncertainties are summarised in Table 1, for the electron channel, and Table 2, for the muon channel.
Figure 1 shows the M_T^W distribution in the 2 jets bin, for the tagged selec-

tion, before and after the rescaling using the SF in Table 1 and Table 22.

Electron Channel	SF	$K_{bb}(K_{cc})$	K_c	K_{light}
2jet exclusive	0.83±0.01	1.31±0.10	1.01±0.04	0.96±0.01
3jet exclusive	0.74±0.01	1.28±0.10	0.99±0.04	0.94±0.01
3jet inclusive	0.74±0.01	1.28±0.10	0.98±0.04	0.93±0.01
4jet exclusive	0.79±0.01	1.26± 0.10	0.97±0.04	0.92±0.01
4jet inclusive	0.76±0.01	1.26±0.10	0.97±0.04	0.92±0.01
5jet inclusive	0.68±0.01	1.25±0.10	0.96±0.04	0.91±0.01

Table 1: Nomralisation scale factor (SF) and heavy flavour scale factors (K_{ii}) with statistical uncertainties for different jet bins, in the electron channel

Muon Channel	SF	$K_{bb}(K_{cc})$	K_c	K_{light}
2jet exclusive	0.82±0.01	1.58±0.09	0.74±0.04	0.98±0.01
3jet exclusive	0.76±0.01	1.54±0.08	0.72±0.04	0.95±0.01
3jet inclusive	0.75±0.01	1.53±0.08	0.71±0.04	0.95±0.01
4jet exclusive	0.75±0.01	1.50±0.08	0.70±0.04	0.93±0.01
4jet inclusive	0.72±0.01	1.49±0.08	0.70±0.04	0.95±0.01
5jet inclusive	0.65±0.01	1.47±0.08	0.69±0.04	0.91±0.01

Table 2: Nomralisation scale factor (SF) and heavy flavour scale factors (K_{ii}) with statistical uncertainties for different jet bins, in the muon channel

5.2 W + jets Scale Factor dependence on kinematic variables

As a second study the SF dependence on different kinematic variables was evaluated.

The first part of this study is on the W+jets SF dependence on jet and lepton p_T and lepton η. After the recalculation of the various SF for cuts on lepton and jet p_T between 25 and 45 GeV, and $\mid \eta \mid$ between 0 and 2.5, the plots for the electron channel and muon channel were compared.

The second part of this study was on how the W+jets SFs depend on E_T^{miss} and M_T^W. The cuts on E_T^{miss} and M_T^W were determined from plotting the two variables against each other, attempting to reduce the QCD contribution. The SFs for different cuts on E_T^{miss} and m_T in the 4 jet inclusive bin were recalculated, keeping the cut on one variable fixed and varying the

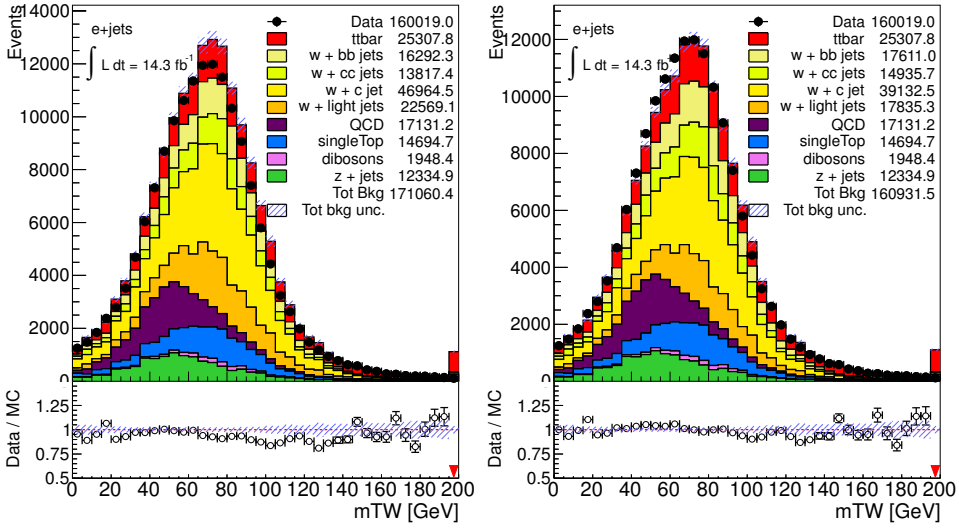

(a) Unscaled (b) Scaled

Figure 1: The M_T^W distribution in the 2jet exclusive bin, for the tagged slection, in the electron channel. The number of events for each distribution is presented in the legend. The unscaled distribution is shown on the left plot, the scaled on the right.

other. The E_T^{miss} cut was between 20 and 40 GeV, while the cut on M_T^W between 40 to 60 GeV, in steps of 5 GeV. Figure 2 shows the normalisation, K_{bb} and K_c SF for the electron and muon channels as a function of M_T^W cuts, for a fixed cut of E_T^{miss}>20 GeV and for the tagged selection.

5.3 Measurement of the $t\bar{t}$ A_C

The numbers presented here are the measurement of the charge asymmetry A_c before unfolding. These values are determined at the reconstruction level and cannot be compared with the theoretical prediction. The measured inclusive reconstructed charge asymmetry is $A_c = 0.007 \pm 0.002$. This is for the electron and munon channels combined.

The charge asymmetry with statistical uncertainties for differential measurements, as a function of $m_{T,t\bar{t}}$, $p_{T,t\bar{t}}$ and $\mid y_{t\bar{t}} \mid$ are shown in Table 3, Table 4 and Table 5, respectively. Table 3 also presents the A_c measure-

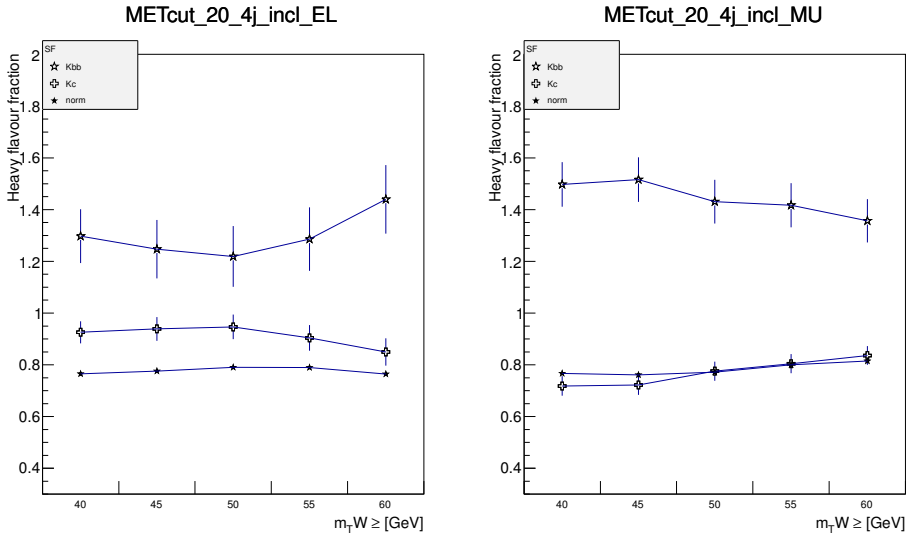

(a) Electron channel (b) Muon channel

Figure 2: The dependence of the normalisation, and the HF SF K_{bb} and Kc, on cuts on M_T^W in the 4jet inclusive bin. The left plot is for the electron channel, the right plot for the muon channel. The cut on E_T^{miss} is 20 GeV.

ment as a function of $m_{T,t\bar{t}}$, with the requirement on the z component of the $t\bar{t}$ system velocity $\beta_{z,t\bar{t}}$ >0.6. For SM predictions, see Ref. [2] and [5]. The statistical uncertainties listed in the tables are calculated with the following formula

$$\sigma_{A_c} = \sqrt{\frac{(1 - {A_c}^2)}{N_{tot}}} \tag{7}$$

where A_c is the measured charge asymmetry and N_{tot} is the total number of events (in a given bin for differential measurements).

	$m_{t\bar{t}}$ [GeV]				
A_c	0-420	420-500	500-600	600-720	720-∞
Before unf.	-0.003 ± 0.006	-0.002 ± 0.009	0.011 ± 0.008	-0.024± 0.010	0.021±0.012
w/$\beta_{z,t\bar{t}}$ >0.6	-0.010 ± 0.014	-0.045 ± 0.023	0.001 ± 0.023	-0.040 ± 0.026	0.080 ± 0.040

Table 3: Measured inclusive charge asymmetry values and statistical uncertainties for the electron and muon channels combined before unfolding as a function of the $t\bar{t}$ invariant mass . The measured asymmetries with the requirement on the z component $t\bar{t}$-system velocity $\beta_{z,t\bar{t}}$ >0.6 are also shown.

	$p_{T,t\bar{t}}$ [GeV]		
A_c	0-25	25-60	60-∞
Before unfolding	0.001 ± 0.010	-0.013 ± 0.007	0.008 ± 0.005

Table 4: Measured inclusive charge asymmetry values and statistical uncertainties for the electron and muon channels combined before unfolding as a function of the $t\bar{t}$-system $p_{T,t\bar{t}}$.

	$\mid y_{T,t\bar{t}} \mid$		
A_c	0-0.3	0.3-0.7	0.7-∞
Before unfolding	0.001 ± 0.010	-0.013 ± 0.007	0.008 ± 0.005

Table 5: Measured inclusive charge asymmetry values and statistical uncertainties for the electron and muon channels combined before unfolding as a function of the $t\bar{t}$-system $\mid y_{T,t\bar{t}} \mid$.

6 Conclusions

From the first study on the W+jets scale factor estimates it seems as if the scale factors improve the agreement between data and MC in almost all jet bins. The study revealed that MC overshoots data systematically in $t\bar{t}$ signal region. Some mismodeling in the E_T^{miss} distribution in the signal region is seen.

From the study on how the SF depend on cuts on lepton and jet p_T and lepton η, it appears that the SF are quite dependent on jet p_T, especially in the electron channel, in the 4 jet exclusive, 4 jet inclusive and 5 jet inclusive bins. They appear less dependent on lepton p_T and η. Analyses with different p_T threshold for these objects should compute SF for their

selection and not use those from the standard selection.
K_{bb} and K_c with standard E_T^{miss} and M_T^W cuts are different when we compare the electron and muon channel. The only real difference in the computation comes from QCD. When the cut on M_T^W is hardened, this reduces the QCD contribution, and SF are more similar between the two channels. There is a similar, but less pronounced effect when the E_T^{miss} cut is hardened.
Finally the top quark charge asymmetry has been measured inclusively and differentially. The results cannot be compared directly with the SM predictions in Ref. [5] because an unfolding procedure is needed to determine A_C at partonic level.

References

[1] ATLAS Collaboration, Measurement of the charge asymmetry in top quark pair production in pp collisions at $\sqrt{s} = 7$ TeV using the ATLAS detector, Eur. Phys. J. C (2012) 72:2039.

[2] ATLAS Collaboration, Measurement of the top quark pair production charge asymmetry in proton-proton collisions at $\sqrt{s} = 7$ TeV using the ATLAS detector, ATLAS-CONF-2013-078.

[3] Object selection and calibration, background estimations and MC samples for the Autumn 2012 Top Quark analyses with 2011 data, ATL-COM-PHYS-2012-1197, https://cds.cern.ch/record/1472525.

[4] U. De Sanctis, Measurements of the top quark charge asymmetry at the LHC, ATL-PHYS-PROC-2012-263.

[5] W. Bernreuther and Z.-G. Si, Top quark and leptonic charge asymmetries for the Tevatron and LHC, Phys. Rev. D86 (2012) 034026.

List of Abbreviations and Acronymes

τ_{had}	hadronic τ decay
τ_{lep}	leptonic τ decay
AD	Antiproton Decelerator
AFII	AtlFast-II
ALICE	A Large Ion Collider Experiment
ATLAS	A Toroidal LHC Apparatus
BDT	Boosted Decision Tree
BEH mechanism	The Brout-Englert-Higgs mechanism
BICEP2	the Background Imaging of Cosmic Extragalactic Polarization experiment 2
CERN	European Organization for Nuclear research
CKM matrix	The Cabbibo-Kobayashi-Maskawa matrix
CL	Confidence Limit
CLIC	Compact Linear Collider
CMB	The Cosmic Microwave Background
CMS	The Compact Muon Solenoid
CNGS	CERN Neutrinos to Grand Sasso
CP	Charge Parity

CR	Control Region
CS	Central Solenoid
CSC	Cathode Strip Chamber
CTP	Central Trigger Processor
DAQ	Data Acquisition
EF	Event Filter
EM	ElectroMagnetic
FCal	Forward calorimeter
Fullsim	Full Geant4 Simulation
GRL	Good Run List
GUT	Grand Unification theory
HEC	Hadronic End-cap Calorimeter
HEP	High Energy Physics
HL-LHC	High Luminosity LHC
IBL	Insertable B-Layer
ID	Inner Detector
ISOLDE	The Isotope mass Separator On-Line facility
ISR	Intersecting Storage Rings
JER	Jet Energy Resolution
JES	Jet Energy Scale
L1	Level 1 (trigger)
LAr	Liquid Argon
LEAR	Low Energy Antiproton Ring
LHC	Large Hadron Collider

LHCb	The Large Hadron Collider beauty
LS1	Long Shutdown 1
LSP	The Lightest Supersymmetric Particle
MC	Monte Carlo
MDT	Monitored Drift Tubes
MSSM	The Minimal Supersymmetric extension of the Standard Model
mSUGRA	The minimal SUperGRAvity model
nTOF	neutron Time-Of-Flight
PDF	Parton Density Function
PS	The Proton Synchrotron
QCD	Quantum Chromo Dynamics
QED	Quantum Electro Dynamics
RGE	Renormalisation Group Equation
ROB	Readout Buffer
RoI	Region of Interest
ROS	Readout System
RPC	Resistive Plate Chamber
SC	Synchrocyclotron
SCT	The SemiConductor Tracker
SLAC	Stanford Linear Accelerator Center
SM	The Standard Model
SPS	The Super proton Synchrotron
SR	Signal region
SUSY	Supersymmetry

T	tesla
TES	Tau Energy Scale
TGC	Thin gap chamber
TMVA	Tool for Multivariate Analysis
TRT	The Transition Radiation Tracker
WIMP	Weakly Interacting Massive Particle